

**FABRICATION, CHARACTERIZATION AND ANALYSIS
OF CARBON NANOTUBE BASED
NANOELECTROMECHANICAL SYSTEM**

WU WEN ZHUO

(B.S., University of Science and Technology of China (USTC))

**A THESIS SUBMITTED FOR
THE DEGREE OF
MASTER OF ENGINEERING**

**DEPARTMENT OF ELECTRICAL AND COMPUTER
ENGINEERING**

NATIONAL UNIVERSITY OF SINGAPORE

2007

ACKNOWLEDGEMENTS

Neither these past two years in Singapore, nor me, nor this thesis would be the same without the help and company of many people.

First, my advisors, Dr. Wong Wai Kin and Dr. Moorthi Palaniapan, whose intuitive insights always turned out to be correct, despite my endless efforts to contradict. Dr. Wong and Dr. Moorthi have imparted lots of knowledge and experience in the project-related area and their understanding and encouragement during my hard times are truly appreciated.

Among many others, I have enjoyed your company in a social setting just as much as your scientific input in the lab. Thank you for teaching me, listening to me, and letting me argue with you. I couldn't ask for better guidance. I was also very fortunate to get help from a lot of people on this project. Special thanks to Mrs. CM Ho, Ms. Anna Li, Mr. Koo Chee Keong, Mr. Mans and other staff from the Centre for Integrated Circuit Failure Analysis and Reliability (CICFAR) for kindly providing support and assistance during this project. I would like to mention my appreciation to the graduate students from CICFAR, Dmitry, Szu Huat, Heng Wah, Jaslyn, Luo Tao, Alfred, Chow Khim, Kin Mum and others for the wonderful company and friendship they have provided. Special thanks to Sing Yang, Wang Lei and Shen Chen for the invaluable discussions and suggestions on various topics. I would also like to thank Jin Quan for the memorable debate, communication and the delicious green tea. Many thanks to the

research fellow from CFCFAR, Dr. Hao Yufeng, and the alumni of CFCFAR, Soon Huat and Kuan Song for the precious discussions on research and various other aspects.

I am appreciative of the constant encouragement and company from all my good friends, especially, Zhang Hong, Zhao Xiaochun, Zheng Yi, Fu Jia, Hou Shengwei and Wu Xue. Thanks for being such good friends and being there for me, when I need it. Thanks to those who I have left out unintentionally but have helped in any way or contributed to my work.

Finally and most importantly, I want to thank my family for always quietly watching out for me, patiently loving me, and sparing advice, when I need it most. I would like to especially thank my Mom, for the care and the love that she has given unconditionally throughout the candidature with her persistence and aspiration. I wouldn't be who I am if it wasn't for you.

TABLE OF CONTENTS

ACKNOWLEDGEMENTS	I
TABLE OF CONTENTS	III
LIST OF FIGURES	VII
LIST OF TABLES	XI
SUMMARY	XII
CHAPTER 1 INTRODUCTION	1
1.1 BACKGROUND	1
1.2 MOTIVATION OF THE PROJECT	2
1.3 PROJECT OBJECTIVES	3
1.4 THESIS OUTLINE	4
CHAPTER 2 LITERATURE REVIEW	6
2.1 INTRODUCTION	6
2.2 MICRO- AND NANOELECTROMECHANICAL SYSTEMS	7
2.3 CARBON NANOTUBES (CNTs)	9
2.3.1 CARBON NANOTUBE STRUCTURE	9
2.3.2 SYNTHESIS	13
2.3.2.1 ARC DISCHARGE	13

2.3.2.2 LASER ABLATION	15
2.3.2.3 CHEMICAL VAPOR DEPOSITION	16
2.3.2.4 HIGH PRESSURE CARBON MONO-OXIDE PROCESS	17
2.3.3 ELECTRICAL PROPERTIES OF CARBON NANOTUBES	17
2.3.4 MECHANICAL PROPERTIES OF CARBON NANOTUBES	20
2.3.5 PREVIOUS WORK ON CNT RESONATORS	22
2.4 ELECTRON MICROSCOPY	23
2.4.1 SCANNING ELECTRON MICROSCOPE	23
2.4.2 TRANSMISSION ELECTRON MICROSCOPE	25
CHAPTER 3 CATALYTIC GROWTH OF CARBON NANOTUBES	28
3.1 OBJECTIVE AND PURPOSE	28
3.2 CHEMICAL VAPOR DEPOSITION	28
3.2.1 GROWTH MECHANISM	30
3.3 METHODOLOGY	31
3.4 EXPERIMENTAL SETUP	33
3.5 CVD GROWTH OF CNTs	37
3.6 MORPHOLOGY	40
3.6.1 CVD PROCESS WITHOUT CATALYST	40
3.6.2 INFLUENCE OF DIFFERENT KINDS OF CATALYSTS	43
3.6.3 CATALYST CONCENTRATION	46
3.6.4 GROWTH DURATION	48
3.6.5 GROWTH TEMPERATURE	51

3.7 PECVD GROWTH OF CNTs	53
3.8 SUMMARY	56
CHAPTER 4 FABRICATION, DETECTION AND CHARACTERIZATION OF	
CARBON NANOTUBE RESONATOR	
4.1 INTRODUCTION	59
4.2 EXPERIMENTAL SETUP AND DEVICE FABRICATION	60
4.2.1 MAKING CONTACTS AND PULLING OUT THE CNT	61
4.2.1.1 CURRENT WELDING	64
4.2.1.2 EBID OF CARBONACEOUS SUBSTANCE	65
4.2.1.3 USE OF VAN DER WAALS FORCE	69
4.2.1.4 USE OF ELECTRIC ATTRACTIVE FORCE	70
4.3 ACTUATION AND DETECTION	72
4.3.1 ACTUATION SETUP	72
4.3.2 DETECTION SETUP	73
4.4 EXPERIMENTAL RESULTS OF CNT RESONATOR SYSTEM	74
4.4.1 OBSERVATION AND CHARACTERIZATION OF OSCILLATION IN SEM	74
4.4.1.1 FORWARD PROCESS AND RESONANCE PEAKS OBSERVED	74
4.4.1.2 BACKWARD PROCESS AND SUB-RESONANCE PEAKS OBSERVED	80
4.4.1.3 INTEGRATED MAPPING OF ELECTRICALLY INDUCED MECHANICAL RESONANCE	86
4.4.1.4 EFFECT OF DC BIAS ON OSCILLATION	87
4.4.2 OBSERVATION AND CHARACTERIZATION OF SAMPLES IN TEM	89

4.4.2.1 PREPARATION PROCEDURES	90
4.4.2.2 RESULTS IN TEM	91
4.5 SUMMARY	93
CHAPTER 5 ANALYSIS OF CARBON NANOTUBE RESONATOR PERFORMANCE	94
5.1 INTRODUCTION	94
5.2 MODEL FOR ACTUATION AND THEORETICAL VALUES OF OUTPUT SIGNAL	95
5.3 CHARACTERIZING RESONANCE OF THE CNT RESONATOR	103
5.4 ULTRA-SENSITIVE MASS SENSOR	117
5.5 SUMMARY	129
CHAPTER 6 CONCLUSIONS AND RECOMMENDATIONS	131
6.1 CONCLUSIONS	131
6.2 RECOMMENDATIONS FOR FUTURE WORK	132
BIBLIOGRAPHY	135

LIST OF FIGURES

Fig 2. 1 Examples of NEMS	8
Fig 2. 2 Structure of CNTs [19].	11
Fig 2. 3 Illustration of pentagon-heptagon defect [28] and the formation of a spiral CNT [29].	12
Fig 2. 4 Schematic of an arc discharge apparatus for synthesizing CNTs [29].	14
Fig 2. 5 Schematic of a laser ablation apparatus for synthesizing CNTs [30].	16
Fig 2. 6 Electronic structure of CNTs [19].	19
Fig 2. 7 Measuring mechanical properties of CNTs [47], [52].	21
Fig 2. 8 Electron path and schematics of SEM and TEM [56].	26
Fig 3. 1 Growth models for catalytic CVD growth of CNTs.	31
Fig 3. 2 Process flow for catalytic CVD growth of CNTs using tungsten wire as substrate	33
Fig 3. 3 Equipment setup for tungsten wire etching	35
Fig 3. 4 Morphology of etched tungsten tips.	35
Fig 3. 5 Tapered tungsten tip mounted on silicon wafer for CVD process.	36
Fig 3. 6 Schematic diagrams of CVD chamber used in the experiments.	39
Fig 3. 7 Philips XL30 FEG scanning electron microscope.	40
Fig 3. 8 Tungsten wire without catalyst after CVD process	41
Fig 3. 9 Growth yields on catalyst-coated patterns and the sterile glades	42

Fig 3. 10 Effect of different catalysts on the CNT growth *	45
Fig 3. 11 Effect of concentration on CNT growth	47
Fig 3. 12 Effect of duration time on CNT growth	49
Fig 3. 13 Coil shape CNTs observed in experiments	50
Fig 3. 14 Effect of temperature on CNT growth	52
Fig 3. 15 Microscope images of PECVD-grown CNTs	54
Fig 3. 16 TEM micrograph of commercial arc-discharge grown CNTs	55
Fig 4. 1 Two types of configurations for single CNT resonator	60
Fig 4. 2 Nanomanipulators mounted onto the SEM	61
Fig 4. 3 Contacting between tungsten tip and CNT and pulling-out of CNT	62
Fig 4. 4 EBID of carbonaceous substance to improve the contact between the CNTs and tungsten tips	66
Fig 4. 5 Doubly-clamped CNT resonator implemented via EBID method	68
Fig 4. 6 Pulling out CNT via Van der Waals force	69
Fig 4. 7 Use of electric attractive force for pulling out CNT	71
Fig 4. 8 Experimental setup for harmonic actuation of electrically induced mechanical resonance in an individual MWNT resonator	73
Fig 4. 9 Schematic of the experimental setup for oscillating nanotubes	73
Fig 4. 10 Eight selected frequencies out of the acquired data points along the forward process, which starts from (a) to (h), exhibit the first order resonance of this CNT system	77

Fig 4. 11 The amplitude-frequency curve of the CNT resonator acquired according to the data points along the forward process. 79

Fig 4. 12 Augmentation of diameter at some sites along the nanotube. 80

Fig 4. 13 The amplitude of oscillation-dc bias curve obtained for $f=109.202\text{ KHz}$, with dc bias from 5 V to 9.5 V. 81

Fig 4. 14 Comparison between the resonance amplitudes for $f=109.606\text{ KHz}$ in forward process and $f=108.680\text{ KHz}$ in backward process.. 82

Fig 4. 15 Amplitude-frequency curves observed for forward and backward processes. 83

Fig 4. 16 Integrated mapping of electrically induced mechanical resonance.. 86

Fig 4. 17 Effect of dc bias on oscillation of CNT system. 89

Fig 4. 18 TEM images of catalytic CVD grown MWNTs..... 92

Fig 5. 1 Schematic of experimental setup and equivalent circuit for actuation of CNT motion..... 96

Fig 5. 2 Schematic of mathematical model for calculation of potential electrically output signal..... 98

Fig 5. 3 Calculated capacitance between tips of CNT and counter electrode and output signal..... 102

Fig 5. 4 TEM and SEM images indicating the structural parameters for CNT resonator. 105

Fig 5. 5 Structures of CVD grown CNT and commercial arc-discharge CNT..... 108

Fig 5. 6 Mapping of electrically induced mechanical resonance of CNT resonator..... 114

Fig 5. 7 Added carbonaceous substances caused by EBID during electron scanning,
indicated as the black bulky part along the CNT..... 116

Fig 5. 8 $\Delta m-t$ curve reveals a linear relationship between the added mass referred to the
first resonance peak and time, the time corresponding to each peak is recorded in
the experiment. 127

Fig 5. 9 Effective mass of CNT system versus time..... 128

LIST OF TABLES

Table 3. 1 Parameters for growth without catalyst	41
Table 3. 2 Parameters of PECVD process demonstrating effects of catalyst	42
Table 4. 1 Growth parameters of MWNT for CNT-cantilever	91
Table 5. 1 Parameters characterizing resonance of CNT system.....	115
Table 5. 2 Added mass and mass sensitivity for peak 1, 2, 3 and 4.....	119
Table 5. 3 Added mass and mass sensitivity of CNT resonator considering loaded mass and variational spring constant	123
Table 5. 4 Loaded mass and mass sensitivity of CNT resonator considering loaded mass and variational spring constant	125
Table 5. 5 Revised loaded mass and mass sensitivity of CNT resonator using pristine CNT mass.	129

SUMMARY

The merit of micromechanical resonators is that miniaturization of the dimensions enhances the sensitivity of these sensors. However, the emerging demands on sensors for gas, virus, and biomolecule detection, for example, require much higher sensitivity of ultrasmall particles. Due to the limitations in fabrication and other practical issues, current microelectromechanical transducers based on conventional materials have nearly reached their sensitivity limits.

Since the discovery in 1991, the extraordinary mechanical and electrical properties have made carbon nanotubes (CNTs) ideal components of nanodevices for the purpose of emerging ultrasensitive applications. Synthesis of catalytic CVD grown multiwalled carbon nanotubes (MWNTs) and fabrication of CNT sensors are described first in this thesis. The feasibility and capability of using catalytic CVD grown MWNTs as ultrasensitive mass sensor which exhibit attogram mass sensitivity are investigated and evaluated. This attogram-sensing capability enables CNT resonator's potentially versatile utilization in various emerging fields and CNT resonator the promising candidate for novel sensing applications to meet the ever-increasingly high-performance requirement.

CHAPTER 1 INTRODUCTION

1.1 Background

Nanoelectromechanical systems (NEMS), the counterpart of microelectromechanical systems (MEMS) at nanoscale, are nano-to-micrometer scale mechanical resonators coupled to electronic devices of similar dimensions [1] , [2] , [3] , which show great potential for promising novel applications and for deepening our understanding of how classical dynamics arises by approximation to quantum dynamics. Sensors, which are making significant impact in everyday life with applications ranging from biomedical to automotive industry, are devices that detect or measure physical and chemical quantities such as temperature, pressure, force, and particles mass. The main requirements of a good sensor are high sensitivity, fast response, and high reliability. This has led to intensive research activities across the world in developing new sensing materials and technologies to meet the ever-increasing demands on ultrasensitive, fast and reliable sensing.

With the advent of nanotechnology, research is underway to create miniaturized sensors which can lead to reduced weight, lower power consumption, and lower cost. The discovery of carbon nanotubes (CNTs) has generated keen interest among researchers to develop CNTs based sensors for many applications. The application of CNTs in next-generation of sensors has the potential of revolutionizing the sensor industry due to their inherently superior properties such as small size, high strength, excellent thermal and electrical conductivity, and large specific surface area [4] , [5] .

CNTs are hexagonal networks of carbon atoms of approximately several nanometers in diameter and one to tens of microns in length, which can essentially be thought of as a layer of graphene rolled-up into a cylinder [5] . Depending on the arrangement of their graphene cylinders, there are two types of nanotubes: single walled nanotubes (SWNTs) and multiwalled nanotubes (MWNTs). SWNTs have only one single layer of graphene cylinders; while MWNTs possess many layers.

With the high frequencies and small inertial masses of the nanomechanical resonators based on CNTs, together with the ultrasensitive mechanical displacement detection capabilities of the coupled electronic devices, CNTs based NEMS show great promise for metrology and various sensing applications.

1.2 Motivation of the Project

The emerging demands on miniaturized, fast and ultrasensitive sensors for gas, virus, and charge detection, for example, require much higher mass sensitivity of ultrasmall particles and have made current microelectromechanical transducers based on conventional materials nearly reach their sensitivity limits due to the limitations in fabrication and other practical issues. CNTs have shown the potential as the most viable candidate to produce NEMS devices of nanometer scale. In order to understand the properties of CNTs and hence the CNTs based systems better, it is ideal to study the CNTs and the progression of properties of CNTs synthesized under various conditions. The conventional top-down approach is not suitable for investigating CNTs based systems due to their ultrasmall sizes and the limitations in fabrication process.

Therefore it is natural to study and investigate synthesis and characterization of CNTs and CNTs based NEMS through the bottom-up approach. Moreover there is also a need to explore the methods in which the inspection and characterization tools available can be utilized for these nano-dimensioned devices and structures like CNTs.

1.3 Project Objectives

This project is aimed to investigate the capability and feasibility of using catalytic CVD grown MWNTs as ultrasensitive mass sensor which exhibit attogram mass sensitivity.

Basically, this project consists of the following three major parts:

- **Synthesis and catalytic CVD growth of MWNTs**

CNTs are synthesized through catalytic CVD process. The catalytic growth in combination with the CVD is the simplest way to generate a relatively large amount of CNTs. Through the plasma enhanced CVD (PECVD) method, well-aligned and ordered CNT structures have also been synthesized in a controlled process on patterned planar surfaces. Growing CNT directly on tungsten wire substrate gives rise to satisfactory electrical contact, which facilitates the subsequent electrical characterization work. Various growth parameters influencing the quality and morphology of the CNTs grown are also investigated to determine the optimal synthesis conditions.

- **Fabrication, actuation and detection of CNT resonator**

Due to the extremely small sizes, it is difficult to realize a CNT based resonator with conventional fabrication, actuation and detection methods. SEM and TEM enable the capability in electrical actuation and *in situ* harmonic detection of electrically induced mechanical resonance of single MWNT cantilever. Due to the incapacity in detecting and investigating the ultralow level output signals electrically, *in situ* investigation of performance of cantilevered CNT resonator prototype under DC and AC bias in SEM needs to be conducted.

- **Characterization of CNT resonator**

The capability and feasibility of using catalytic CVD grown MWNTs as ultrasensitive mass sensor which exhibit attogram mass sensitivity are investigated and evaluated by characterizing the CNT resonator. This attogram-sensing capability enables CNT resonator's potentially versatile utilizations in various emerging fields such as biomolecule, virus and gas detection.

1.4 Thesis outline

This thesis consists of six chapters. Following this introduction chapter is a literature survey which provides a basic introduction to NEMS, CNTs' properties and synthesis methods of CNTs. Previous work done on CNTs resonators and the basics of

characterization facilities used are also addressed and discussed at the end of this chapter. Chapter 3 investigates the catalytic CVD growth process for synthesizing MWNTs. Growth parameters influencing synthesis results of the CNTs are investigated and the optimal synthesis condition is determined in this chapter. Chapter 4 describes the fabrication of CNTs based resonators in both cantilever and doubly-clamped configurations and the method for electrical actuation and *in situ* harmonic detection of electrically induced mechanical resonance of single MWNT cantilever. Details of the experimental setup, techniques for device fabrication, actuation and detection, and the experimental results for characterizing the CNT resonator system are also investigated in this chapter. In chapter 5, a quantitative model for describing the specific actuation method and theoretical output signal of the CNT resonator motion is presented first. Important parameters which describe and characterize CNT resonator are calculated using the hollow tube model and compared with both the theoretically values predicted and experimental results reported. The capability and feasibility of CNT resonator acting as ultra-sensitive mass sensor is examined and discussed in details afterwards. Chapter 6 concludes this thesis and provides some recommendations for future work.

CHAPTER 2 LITERATURE REVIEW

2.1 Introduction

Microelectromechanical devices have been the cynosure of extensive research for a number of years and have generated much excitement as their potential utilizations in various applications have been increasing. An electromechanical device is basically a mechanical structural element, such as a beam or a cantilever, which is controlled via a microelectronic circuit. Technologies of microelectromechanical systems (MEMS) are currently used to make such diverse systems as electric current regulators [6] , microscale mirrors arrays [7] , RF electronic devices, accelerometers in automobile crash airbags systems, and various ultrasensitive sensors.

Nanoelectromechanical system (NEMS) is the natural successor to and shrunken counterpart of MEMS as the size of the devices is scaled down to the nanometer domain. NEMS also holds promise for lots of scientific and technological applications. Particularly, NEMS has been proposed for use in ultrasensitive mass detection [3] , RF signal processing [8] , and as a model system for exploring quantum phenomena and applications in macroscopic systems [9] . To improve sensitivity for these applications requires decreasing the size, or, more importantly, decreasing the active mass of the system, thus increasing the resonant frequency, and decreasing the line-width of the resonance to achieve high quality factors. One promising candidate, perhaps the ultimate, material for these applications is carbon nanotube (CNT). CNT is the stiffest

material known, has low density and ultrahigh aspect ratio, and could be defect-free. Properties of CNTs will be discussed later.

In this chapter a basic introduction to MEMS and NEMS will be presented first. A brief introduction to CNTs' structure, synthesis methods, and their electrical and mechanical properties will be discussed afterwards. Previous work done on CNTs resonators will also be addressed. The basics of characterization facilities used, specifically SEM and TEM, are discussed at the end of this chapter.

2.2 Micro- and nanoelectromechanical systems

A typical electromechanical device can be described as a system where electrically controlled signals provide mechanical stimuli to a resonator, whose mechanical motion, typically the displacement of the element, is then transduced back into electrical signals. Additional control electrical signals can be applied to change the two main characteristics of the resonator: its resonant frequency $\omega_0/2\pi$ and quality factor Q . There are various types of geometries that are used in NEMS. Figure 2.1 shows some of the representatives. In general, flexural and torsional vibrations are the two types of mechanical motions that are mostly used. An example of a flexural resonator is a doubly clamped beam or a cantilever, and an example of a torsional oscillator is a paddle. Only flexural resonators, particularly the cantilever geometries, are considered in this thesis.

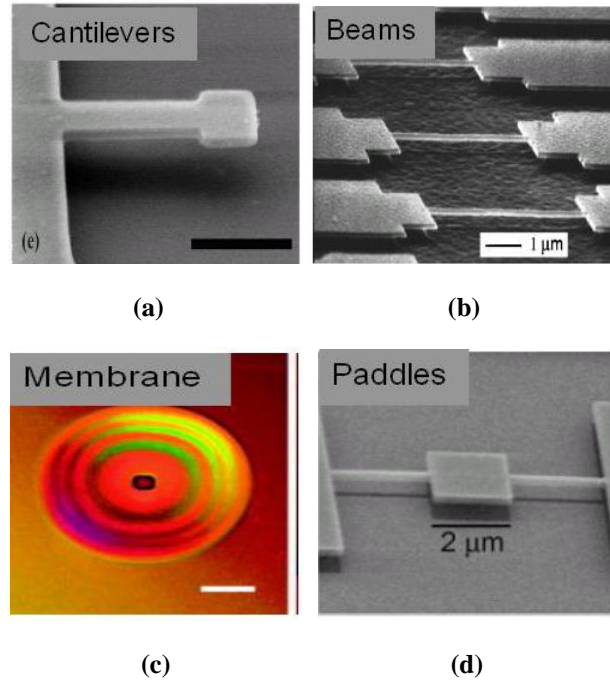


Fig 2. 1 Examples of NEMS. (a), (b), (c) Examples of NEMS devices utilizing flexural vibration. (a) Singly clamped cantilever [10] . (b) Doubly clamped resonators [11] . (c) Suspended membrane [12] . (d) NEMS utilizing torsional vibration, a paddle [13] .

Experimentally, NEMS can operate at frequencies in the range of gigahertz. Due to the small sizes, actuating and detecting the motion of the vibrating element at such high resonant frequencies becomes a challenge. Typical NEMS operates with Q in the range of 10^3 - 10^5 . These values are much higher than those typically available with conventional electronic oscillators, but still inferior to MEMS counterparts. Ultrahigh quality factors are desirable as the minimum operating power of the device is decreased; hence its sensitivity to external driving and the selectivity in the spectral domain are resultantly increased. Such qualities make NEMS useful for a variety of different applications such as digital signal processing [14] , mass detection [15] , and force sensing [16] .

The most common and conventional top-down approach to microfabrication involves lithographic patterning techniques using short-wavelength optical sources. However, below a certain size, entirely different production techniques must be employed, on one hand due to preeminent surface effects which are difficult to control, and the other because the physics of the phenomena is susceptible to change at nanoscale which already lies in the quantum realm. To meet the increasingly stringent performance requirement, novel materials possessing distinct properties have been investigated in elementary research to study their feasibility as alternatives of conventional materials and candidates for new applications. Due to their remarkable electrical, mechanical, and electro-mechanical properties, CNTs have been a subject of intensive research since their discovery in 1991 [17] .

2.3 Carbon nanotubes (CNTs)

2.3.1 Carbon nanotube structure

CNTs are thin, hollow cylinders of covalently bonded carbon atoms. They fall into two different categories: single-walled carbon nanotubes (SWNTs) and multiwalled carbon nanotubes (MWNTs), which consist of concentric SWNTs stacked together. SWNTs are typically 1-2 *nm* in diameter and several μm in length, but SWNTs up to *mm* long have been grown and reported [18] . MWNTs typically have diameters in the range of 5-50 *nm* and are typically several tens of μm in length.

The carbon atoms in the walls of a “perfect” nanotube are arranged in a honeycomb lattice just as in a single sheet of graphene. In fact, a CNT can be thought of as a single

rolled graphene sheet (See Fig 2.2a). The properties of a CNT then are derived from the properties of graphene. Depending on the “rolling” angle with respect to the lattice, the relative arrangements of the atoms in the walls of the CNT with respect to the axis are different. The angle between the orientation of the lattice and the nanotube’s axis is known as the “chiral angle” of the CNT. Fig 2.2b, c and d show examples of CNTs with different chiralities.

Several types of defects can influence the structure and binding in a CNT. These defects include substitutional impurities, adsorption of molecules, pentagon-heptagon defects and carbonization.

Substitutional impurities are atoms other than carbon incorporated at lattice sites in the CNT, which are typically boron or nitrogen atoms [20] . The presence of substitutional atoms will change the unit cell of the CNT and thereby the binding and electrical properties.

Adsorption of molecules to the surface of the CNT will change the unit cell and thereby the electrical properties of this CNT. Particularly the adsorption of NO_2 and NH_3 molecules has been studied intensely [21] [22] [23] [24] [25] .

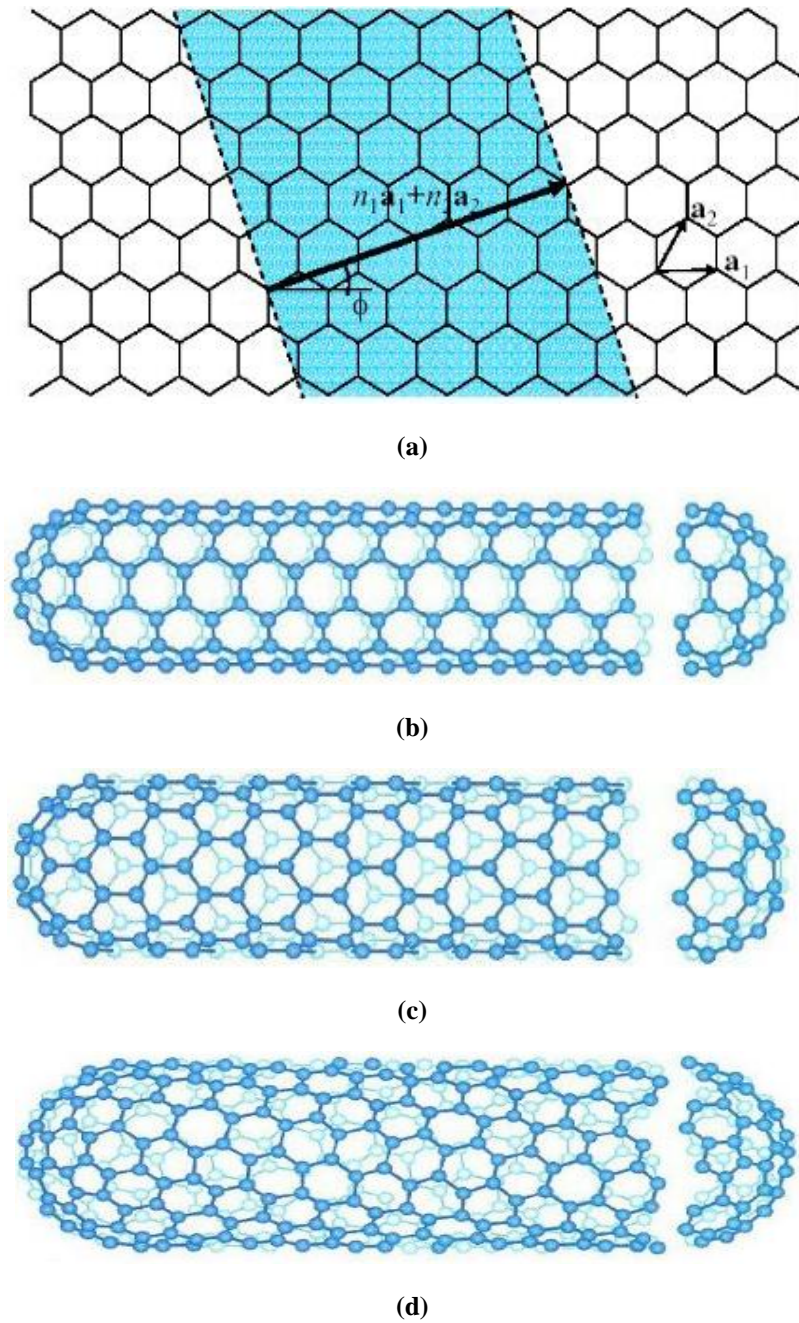


Fig 2. 2 Structure of CNTs [19] . (a) A CNT is formed by wrapping a graphene sheet. The shaded area shows the part of the sheet to be rolled and the black arrow identifies the direction of wrapping. The angle between the direction of wrapping and the lattice is called the “chiral” angle. (b) An “armchair” CNT ($\Phi=30^\circ$). (c) A “zigzag” CNT ($\Phi=0^\circ$). (d) A “chiral” CNT (Φ is arbitrary). Φ is the chiral angle.

Pentagon-heptagon defects are structural defects where a pentagonal ring of carbon is situated adjacent to a heptagonal ring. This will cause the CNT to bend towards the heptagon as shown in Fig 2.3 [26] . With an even distribution of these defects the CNT will possibly form a coil, which has been observed in the experiments (seen in Chapter 3). Meanwhile the pentagon-heptagon defect causes change in chirality.

Carbonization means that the carbon atoms are not arranged in any kind of lattice or in other words, in the amorphous form. The amount of carbonization presenting in a CNT depends on the specific method of growth.

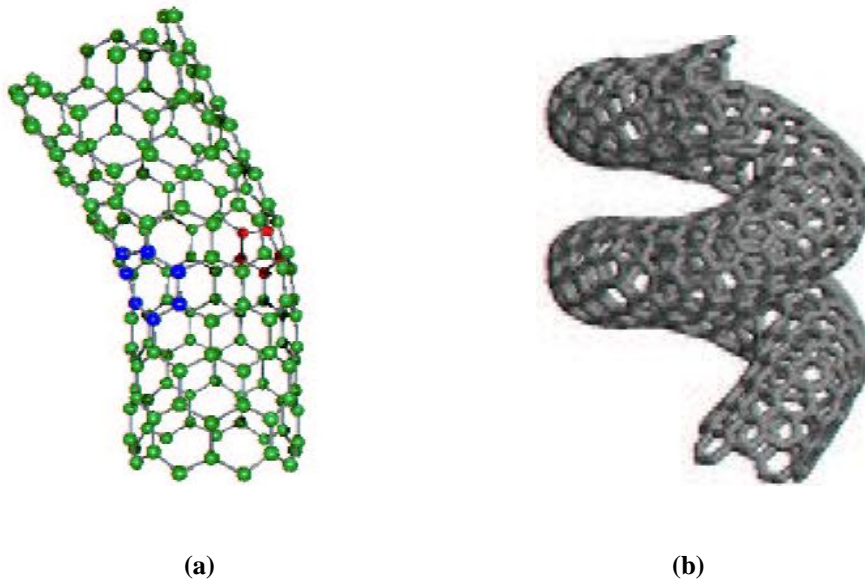


Fig 2. 3 Illustration of pentagon-heptagon defect [28] and the formation of a spiral CNT [29] . (a) Illustration of pentagon-heptagon defect [28] . Red pentagon represents the pentagon defect while blue heptagon is the heptagon defect. (b) The formation of a spiral if these defects are spread throughout the CNT [29] .

2.3.2 Synthesis

Since the discovery of CNTs in soot from arc discharge [17] , several methods of synthesizing CNTs have been realized. Four of these approaches will be described in this section: arc discharge, laser ablation, chemical vapor deposition, and HiPco. The last method has been investigated intensively in the past few years, and the results indicate that the HiPco process might be the future large scale synthesis method of CNTs.

2.3.2.1 Arc discharge

Arc discharge provides a simple method for vaporizing carbon into plasma, which leads to the formation of high quality CNTs.

An illustration of a typical carbon arc discharge apparatus is shown in Fig 2.4. The anode and cathode are both carbon rods of 5-20 *mm* in diameter, and the position of anode can be adjusted so that the optimum distance between the anode and cathode can be maintained continuously as the end of the anode is evaporated off during CNT growth. The dc voltage across the anode and cathode is around 20-25 *V* with a current in the range of 50-120 *A*. During operation helium flows through the chamber with a flow rate of 5-15 *ml/s* and pressure in the chamber is typically in the order of 500 *torr* [20] .

CNTs are produced in bundles in the inner region of the cathode, where the temperature is highest. The bundles are aligned in the direction of the current. The yield of CNTs

and exactly what kind of CNTs produced are very much dependent on the growth conditions, even though the spread in diameter is usually narrow. The maximum yield obtained is around 20% of the evaporated graphite and this is only in the center of the cathode [20] . Also by using different catalyst in the graphite rods it is possible to induce the formation of SWNTs, MWNTs, ropes of SWNTs, or bundles of SWNTs. Other carbon particles are also deposited on the walls of the chamber and around the CNTs.

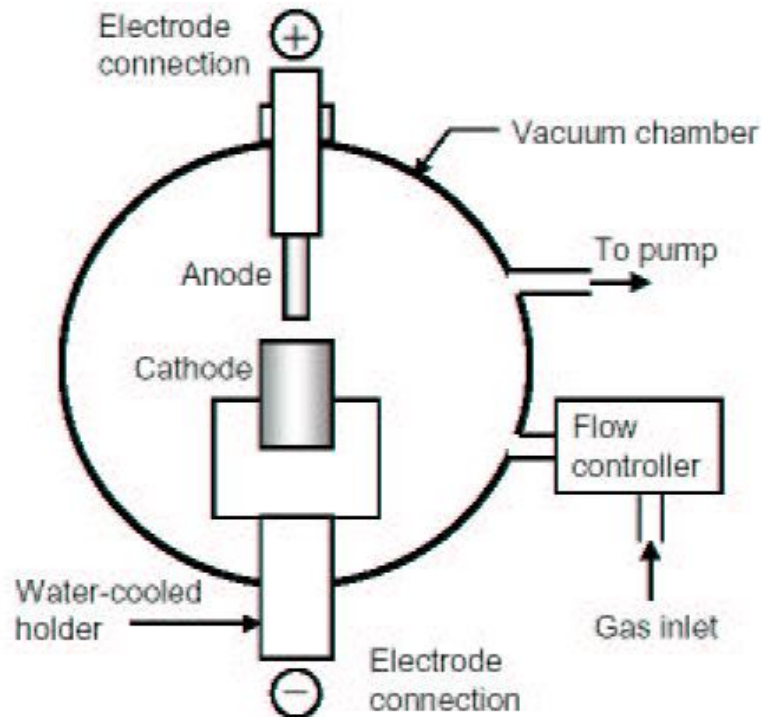


Fig 2. 4 Schematic of an arc discharge apparatus for synthesizing CNTs [29] . The anode and cathode, both made primarily of carbon, are positioned at optimal distance while a high current is passed from the anode to the cathode making an arc discharge. During this arc discharge carbon plasma is formed, and CNTs are deposited on the cathode.

The arc discharge method is a simple and economic way of synthesizing nearly defect-free CNTs. One of the drawbacks of this method compared to other methods, however, is the poor control of the deposition area. There is no way to produce the CNTs at a desired position in a device using arc discharge. Furthermore the formed CNTs will be mixed with several other carbon particles and the need for purification is apparent.

2.3.2.2 Laser ablation

A very efficient way of synthesizing ropes of SWNT is using a powerful laser to evaporate a graphite sample. The principle and apparatus of production is shown in Fig 2.5. The graphite (mixed with a small amount of transition metals) target is placed in a furnace, and hit by a laser beam. Opposite the laser is a water-cooled copper collector just outside the furnace. A steady flow of argon from the laser to the copper collector makes the vaporized carbon flow from the target to the collector, where it will deposit and form ropes of SWNTs [20] . The ropes of SWNT produced will typically have diameters in the range from 10-20 *nm* and length up to 100 μ *m*. Individual SWNT has diameter in the range from 1-3 *nm*. The distribution of diameters is usually very narrow and the diameter depends on the transition metals mixed in the graphite target as well as temperature and other experimental parameters.

The laser ablation method is probably the best way of making defect free SWNT. The disadvantage of this method is, as in the case of the arc discharge method, the poor control of deposition area, making the method useless in a device fabrication process. Furthermore the method is rather costly because of the high powered lasers engaged.

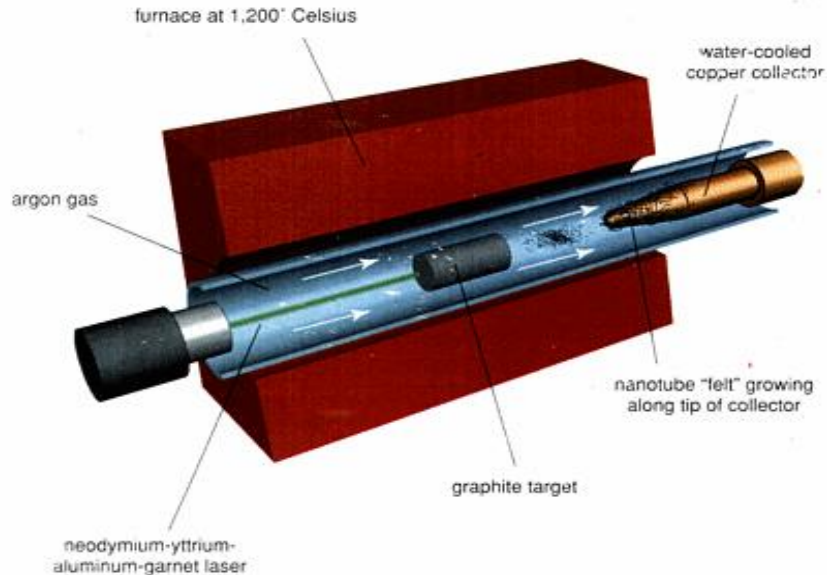


Fig 2. 5 Schematic of a laser ablation apparatus for synthesizing CNTs [30] . In this case an Nd YAG laser hits the graphite target heated to 1200°C and carbon is evaporated. The steady flow of argon sweeps the carbon to the water cooled copper collector, where the carbon deposits forming ropes of SWNT.

2.3.2.3 Chemical Vapor Deposition

Chemical vapor deposition (CVD) method of producing CNTs incorporates the disassociation of carbon-containing molecules and the utilization of catalyst particles, mainly the transition metals. In the chemical vapor deposition process (CVD), chemical reactions take place which transform gaseous molecules, called precursor, into a solid material on the surface of the substrate. CVD has been a very versatile process used in the production of coatings, powders, fibers and monolithic parts. With CVD, it is possible to produce almost any metallic or non-metallic element, including carbon and silicon, as well as compounds such as carbides, borides, nitrides, oxides and many

others. The catalytic chemical vapor deposition of carbon nanotubes is adopted in this project and related details will be discussed in Chapter 3.

2.3.2.4 High pressure carbon mono-oxide process

The High Pressure Carbon mono-Oxide (HiPco) process is based on the same principles as CVD process. In HiPco the carbon atoms come from carbon monoxide gas, which is continuously pumped into a high-pressure (30-50 *atm*) reaction chamber working at a temperature of 900-1100°C, where it is mixed with industrial gas containing the necessary catalysts to sustain the chemical reactions which create CNTs.

The temperature and pressure conditions required in HiPco process are common in industrial plants, and HiPco is both a less expensive and faster method of producing SWNT than the other methods. Research of the parameters involved in HiPco process [31] at Rice University has optimized the process making it possible to produce 250g of SWNT in less than a week. Nevertheless there is still no way of controlling the area of deposition, despite the large yield and fast production rate of HiPco process.

2.3.3 Electrical properties of carbon nanotubes

Carbon nanotubes inherit their remarkable electrical properties from the unique electronic band structure of graphene (Fig 2.6a). Depending on its chirality, nanotube can be either metallic, semiconducting [32], or semiconducting with a small band gap [33]

The cylindrical structure of a CNT imposes periodic boundary conditions on the electron wave function around the nanotube's circumference, and transport in SWNT occurs only along the axis of the tube, making a CNT a 1D conductor. The conductance G of a 1D channel is given by the Landauer-Buttiker model [34]

$$G = \left(\frac{e^2}{h} \right) \sum_i T_i \quad (2.1)$$

where T_i denotes the transmission probability through the i -th channel, and e^2/h is the conductance quantum. In nanotubes there are four degenerate 1D channels: two due to spin degeneracy, and two due to the degeneracy arising from clockwise/counterclockwise “handedness” of the electron wave function, which is shown in Fig 2.6d. Therefore, the theoretical low-bias conductance of a CNT with perfect transmission is

$$G = 4 \left(\frac{e^2}{h} \right) \quad (2.2)$$

Conductances approaching the value in Equation (2.2) have been measured experimentally in high quality metallic tubes with lengths of 200 nm [35] , [36] and in semiconducting tubes at “on” state [37] , [38] . These are essentially ballistic nanotubes. For longer tubes, the main origin of resistivity at low biases is believed to be due to scattering by acoustic phonons [39] with experimentally measured mean free paths at room temperature of around 1 μm .

Semiconducting CNTs have a band gap $E_g = 0.7 eV / D$, where D is the CNT diameter in the unit of nm [40] , which separates the valence and conduction bands. Small-band semiconducting tubes have gaps on the order $\leq 100 meV$ that originate from

perturbations such as twist, curvature, or local strain in an otherwise metallic tube [41] , [42] .

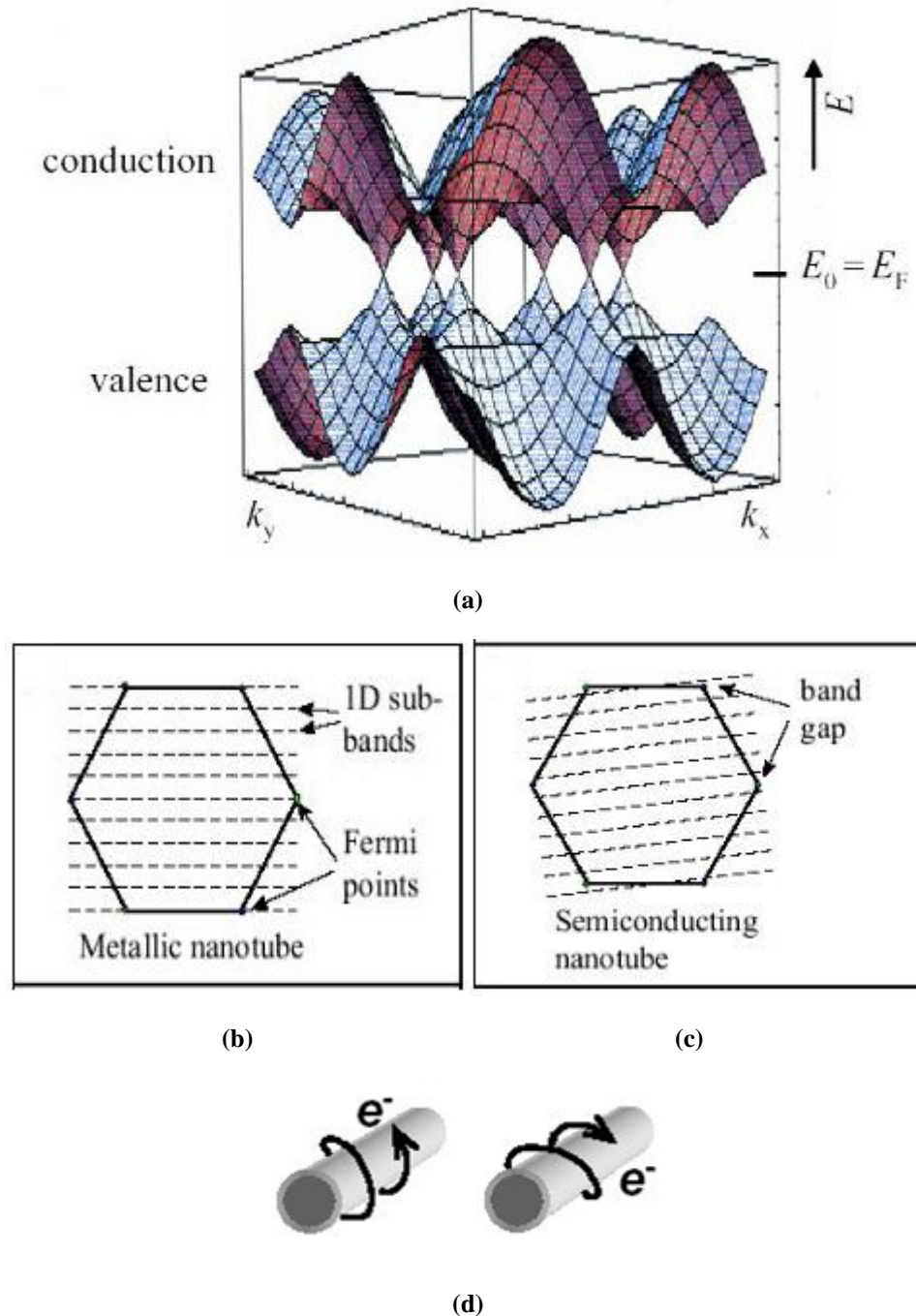


Fig 2. 6 Electronic structure of CNTs [19] . (a) Band structure of graphene. (b), (c) Imposing the boundary conditions of the band structure leads to allowed states on the equidistant lines in k -space. For a metallic CNT (b) the lines cross the points of zero bandgap (the Fermi points). For a semiconducting CNT (c) the lines miss the Fermi points. (d) 4-fold degeneracy of a CNT: two states due to spin and two states due to the “handedness” of the wave function.

2.3.4 Mechanical properties of carbon nanotubes

CNTs owe their mechanical properties to the strength of the sp^2 hybridized C-C bond. The two most important parameters characterizing the mechanical properties of a material are the elastic modulus E

$$\sigma = \varepsilon E \quad (2.3)$$

that describes the slope of the stress σ vs. strain ε curve, and the tensile strength σ_s , which describes the maximum stress the material can endure. If further stress is applied the material either fractures or undergoes irreversible plastic deformation.

Theoretical calculations for the elastic modulus and the tensile strength of a CNT predicted values ranging from $0.5TPa$ to $5TPa$ for the elastic modulus [43] , [44] , [45] and $10GPa$ to $40GPa$ for the tensile strength [46] .

Experimentally, neither parameter is easy to measure due to the small size of CNTs. Two techniques, however, have been proved useful in measuring these properties: Atomic Force Microscopy (AFM) and Electron Microscopy. Early work concentrated mostly on the properties of MWNT and CNT bundles [47] in which Transmission Electron Microscopy (TEM) was used to image thermal vibrations of MWNTs at high temperature and then extracted the elastic modulus, ranging from 0.4 to $4.15TPa$, by fitting the shape of the resonance as shown in Fig 2.7a. This work was later continued

by several other groups using TEM with MWNTs [48] , with reported values around $1.4TPa$. Electrically excited CNT vibrations have also been used to measure elastic modulus [49] , [50] with extracted elastic modulus values of approximately $1TPa$.

Wong *et al* [51] used an AFM cantilever to bend singly clamped MWNTs and directly measure their elasticity and strength. They found values of elastic modulus of around $1.3TPa$. Minot *et al* [52] have used similar methods to study the elastic properties of doubly clamped ropes of SWNT and individual doubly clamped SWNTs (see Fig 2.7b).

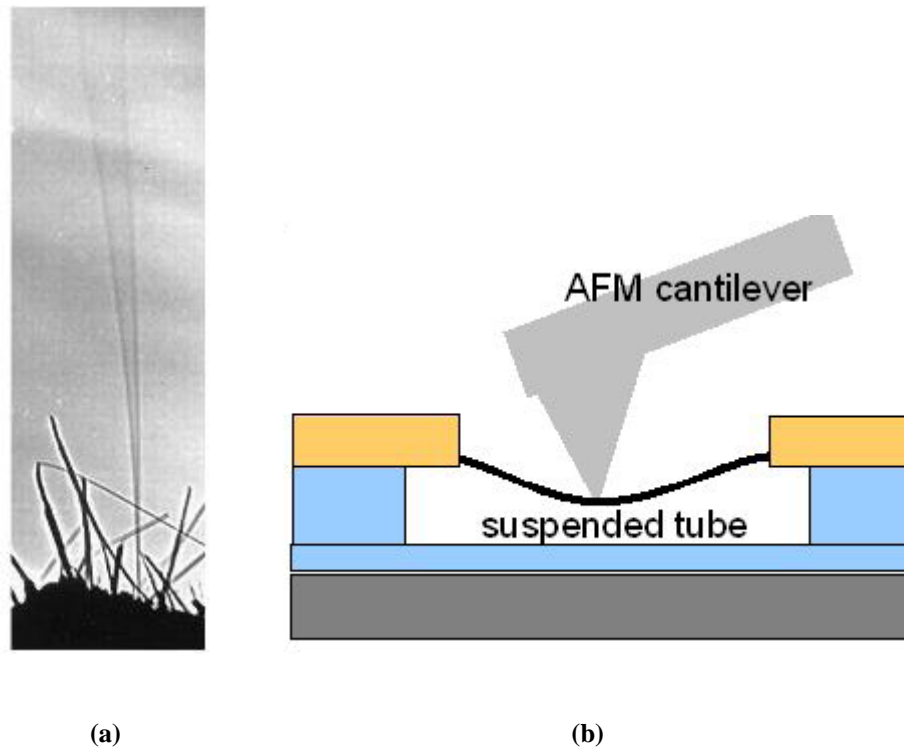


Fig 2. 7 Measuring mechanical properties of CNTs [47] , [52] . (a) Thermal vibrations of MWNT in a TEM [47] (b) A schematic of a suspended CNT stretched by an AFM tip [52] .

As the electronic properties of CNTs are highly sensitive to the geometric configurations of the constituent atoms, it is also possible to study the effect of mechanical modifications on the electronic properties of the CNT. Theoretically it has

been predicted [41] , [42] that it is possible to modify the band gap of a semiconducting CNT and induce a band gap in certain metallic tubes by applying strain to CNTs. Indeed, it has been experimentally shown that the band gap E_g of a semiconducting nanotube can be tuned by applying a small mechanical strain σ [52] as

$$\frac{dE_g}{d\sigma} \approx \pm 100 \frac{meV}{\%} \cos 3\phi \quad (2.4)$$

where ϕ is the chiral angle and the sign of the result depends on the exact wrapping vectors.

2.3.5 Previous work on CNT resonators

Early work on CNT resonators was done mainly on MWNTs in an electron microscopy system for the purpose of measuring the elastic modulus of CNTs [49] . MWNTs were grown on a holder by either pyrolysis [49] or arc-discharge [50] and were placed in cantilever configuration in either TEM or SEM. From the measured resonance frequencies of $1MHz$ [49] , the elastic modulus E could be extracted and was found to be in the range of $0.2-2TPa$. In the above experiments, the extracted quality factors were on the order of 100 to 200, which were attributed mainly to the abundance of defects in pyrolysis and arc-discharge grown nanotubes.

Later, Purcell *et al.* [53] grew MWNTs, typically $10-25 nm$ in radius and $10-40 \mu m$ long, by CVD, which typically produces close to defect free tubes. Actuation was done electrostatically in this experiment. A nanotube, grown on a metallic tip, was placed

between two electrodes to form the doubly-clamp configuration. The detection of the resonance was performed using the CNT as a field emitter. The measured frequencies were on the order of 1MHz , similar to results of the previous research. Since the detection scheme of measuring the emission current was highly nonlinear in the amplitude of vibration, the shape of the resonance did not look Lorentzian as expected. Nonetheless, the effective quality factor for the resonance was measured, and was found to be roughly 2400, higher than the previous results. For ultrasensitive applications like biosensor and high-frequency applications like RF communications, however, resonators with higher resonant frequency and better quality factors are demanded.

Despite of the success of the detection methods described above, they still suffered several disadvantages. Firstly, using a TEM or SEM, or applying several hundred volts to detect the resonance is unrealistic for any industrial application in reality. Secondly, the electron beam used for imaging in TEM and SEM interacts with the CNT and even damages it structurally, which has been ignored in previous research and will be investigated in details in this thesis. Lastly, all of these techniques are limited in their sensitivities to tens of nm vibration amplitudes by the resolution of the imaging beam. Such poor sensitivity may push the operation of these resonators into the nonlinear regime.

2.4 Electron Microscopy

2.4.1 Scanning Electron Microscope

The scanning electron microscope (SEM) is used extensively to study the surface of materials rather than their internal arrangement. Its ability to resolve fine details lies intermediate between the optical microscope and the high resolution TEM. SEM magnifications can go to beyond 300,000X and most semiconductor manufacturing applications nowadays require nanometer resolution and below. SEM inspection is often used in the analysis of die/package cracks and fracture surfaces, bond failures, and physical defects on the die or package surface.

During SEM inspection, a beam of electrons is focused onto a spot volume of the specimen, resulting in the transfer of energy to the spot. These bombarding electrons, also referred to as primary electrons, dislodge electrons from the specimen itself. The dislodged electrons, also known as secondary electrons, are attracted and collected by a positively biased grid or detector, and then translated into a signal. To produce the SEM image, the electron beam is swept across the area being inspected, producing many such signals. These signals are then amplified, analyzed, and translated into images of the topography being inspected. Finally, the image is shown on a CRT screen.

The energy of the primary electrons determines the quantity of secondary electrons collected during inspection. The emission of secondary electrons from the specimen increases as the energy of the primary electron beam increases, until a certain limit is reached. Beyond this limit, the collected secondary electrons diminish as the energy of the primary beam is increased, because the primary beam is already activating electrons deep below the surface of the specimen. Electrons coming from such depths usually recombine before reaching the surface for emission.

Aside from secondary electrons, the primary electron beam also results in the emission of backscattered electrons from the specimen [54] . Backscattered electrons possess more energy than secondary electrons, and have a definite direction. As such, they can not be collected by a secondary electron detector, unless the detector is directly in their path of travel. Backscattered electron imaging is useful in distinguishing one material from another, since the yield of the collected backscattered electrons increases monotonically with the specimen's atomic number.

The versatility of SEM enables it the indispensable equipment in this project, in which SEM is performed to analyze the micro- and nanostructures in plan view. A Philips XL 30 microscope equipped with a field emission gun (FEG) operating at an acceleration voltage between 2 and 10 *kV*, with a working distance of typically 10 *mm*, and in secondary electron (SE) image mode is used.

2.4.2 Transmission Electron Microscope

Transmission electron microscope (TEM) operates on the same basic principles as the optical microscope but uses electrons instead of light. It has been developed further to make fuller use of the special properties of electron illumination, principally the higher resolution, but also the ability to carry out various forms of elemental and crystallographic microanalysis [55] . Electro-optically, TEM has little in common with the SEM apart from the use of an electron gun and a condenser lens system to produce a focused electron beam. Differences as well as connections between the configurations of both SEM and TEM are illustrated in Fig 2.8.

TEM has an evacuated metal cylinder of height 2 m with a source of illumination on top. An acceleration voltage of 80 kV to 300 kV is set between the cathode and anode. Electrons are accelerated through a small hole in the anode.

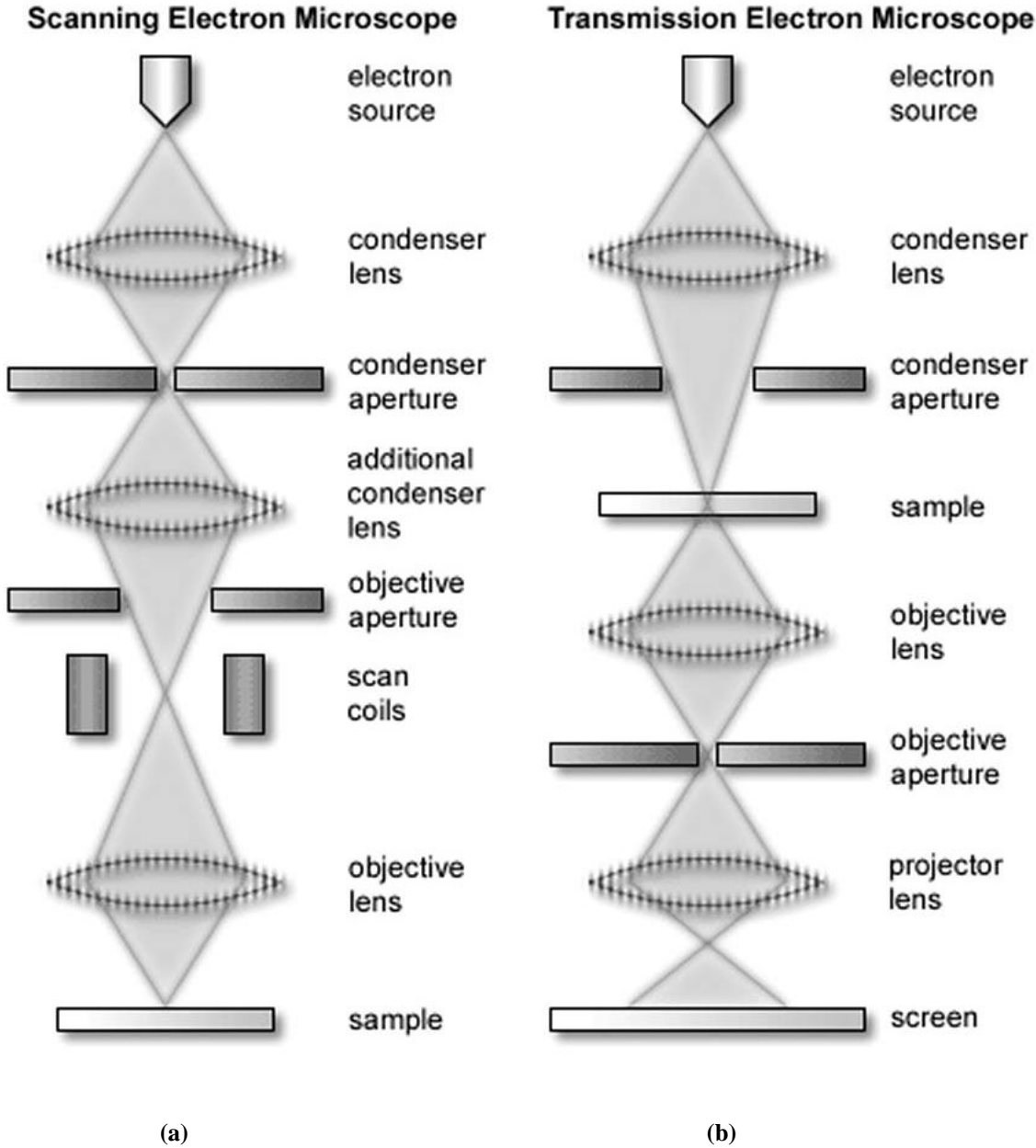


Fig 2. 8 Electron path and schematics of SEM and TEM [56] . (a) SEM and (b) TEM.

The simplest TEM has two image-forming lenses and is an exact analogy of the compound light microscope. The illumination coming from an electron gun is concentrated on the specimen by a condenser lens. After passing through the specimen the electrons are focused by the objective lens into a magnified intermediate image. This image is further enlarged by a projector lens and the final image is formed on a fluorescent screen, a photographic film or a CCD camera [55] . Nowadays, TEMs can reach atomic resolution using voltages of 200 *kV* and higher. Objects to the order of a few angstroms ($10^{-10} m$) can be observed and investigated with the aid of TEM and the possibility for high magnifications has made TEM a valuable tool in both medical, biological and materials research.

CHAPTER 3

CATALYTIC GROWTH OF CARBON NANOTUBES

3.1 Objective and Purpose

This chapter focuses on synthesizing CNTs through catalytic CVD process. The catalytic growth in combination with the CVD is the simplest way to generate a relatively large amount of CNTs. Through the plasma enhanced CVD (PECVD) method, well-aligned and ordered CNT structures have also been synthesized in a controlled process on patterned planar surfaces. Growing CNT directly on tungsten wire substrate gives rise to satisfactory electrical contact, which facilitates the subsequent electrical characterization work. Various growth parameters influencing the quality and morphology of the CNTs grown are also investigated in this chapter.

3.2 Chemical Vapor Deposition

Chemical reactions take place which transmit gaseous molecules, called precursor, into a solid material on the surface of the substrate in a typical CVD process. Microfabrication processes widely use CVD as a versatile technique to deposit diverse materials such as silicon and carbon in various forms including monocrystalline, polycrystalline, amorphous, and epitaxial.

Various configurations have been employed for CVD: horizontal or vertical tube reactors, showerhead reactors or reactors with plasma enhancement. The reactor chamber used in this project can synthesize CNTs through both thermal CVD and PECVD. When operating in thermal CVD mode, samples are heated separated from the gas dispense and the chamber wall, which indicates the chamber wall is “cold” compared to the heating substrate. While growing CNT in PECVD mode, inside the reactor with plasma enhancement, direct-current plasma is created by an electrical discharge between the top electrode and grounded substrate. The excited electrons collide with gas molecules to form ions, reactive neutrals in plasma. An advantage of PECVD is the ability to deposit at much lower temperatures and pressures than would be required for thermal CVD. Nevertheless a severe disadvantage is usually a higher disorder and hence more defects in the created structures and a lack of uniformity over larger surface areas, which is observed during the synthesis processes. Therefore mainly thermal catalytic CVD grown CNTs are investigated in this project; the results of PECVD growth of CNTs will also be discussed briefly at the end of this chapter.

In the frame of this chapter a catalytic growth of CNTs is performed by CVD of hydrocarbons (acetylene in this project). Ferrous chemicals on tapered tungsten tips or transition metals (Fe, Ni, Co) patterned on a flat substrate (Si/SiO₂) are used as catalysts. The advantage of coating ferrous chemical on tungsten tips is to facilitate the following electrical characterization while the patterning on flat substrate is to help synthesize large-scale CNTs and also compare growth yields in regions with and without catalysts, and thus determine the role of the catalysts. The decomposition of the acetylene gas and the CNT growth are activated by the catalyst in the process. During the CVD procedure

the precursor gas acetylene is decomposed catalytically to $2C+H_2$ and acts as carbon source for the assembly of the nanostructures.

3.2.1 Growth mechanism

When heat is applied to substrate coated with catalyst film, the increased surface mobility of the catalyst atoms causes the film to coalesce into nanoclusters [57] . The thickness of the catalyst film, growth temperature and time determine the size of these nanoclusters jointly [58] , [59] .

There is a further consideration with respect to the catalyst layer. Chemical interaction might take place between the catalyst and substrate when heat is applied. If there is a reaction, the catalyst material will dissipate, ending its utility for initiating CNT growth. This is a problem especially when using silicon as the substrate with transition metals, as these transition metals would diffuse into the substrate at the growth temperatures. Therefore <111>-oriented boron doped silicon with native SiO_2 layer is chosen as alternate substrate in this project since this thin barrier of SiO_2 can help eliminate the above problem mentioned.

Depending upon the strength of the interaction between the catalyst metal and the substrate upon which the catalyst is deposited, two different growth models have been proposed [60] . These two models are illustrated in Fig 3.1. In each case, carbon is extracted from the hydrocarbon precursor gas and diffuses through the catalyst particle before taking its place in the forming CNT. The growth model when there is weak

interaction between the catalyst particle and the substrate is known as “tip growth”, as the catalyst particle keeps staying at the tip of the CNT. The model when strong interaction appears is known as “root growth”, as the catalyst particle remains anchored to the substrate at the base of the grown CNT. In this project, location of catalyst particle and morphology of CNTs observed support tip growth model only, which implies that possibly the interactions between the catalyst materials chosen and the substrates in this project are not strong enough to keep the catalyst particles riveted to the substrates.

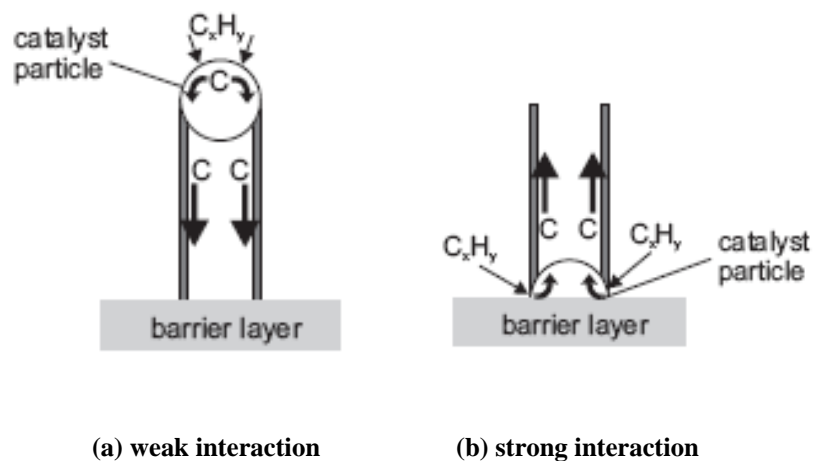


Fig 3. 1 Growth models for catalytic CVD growth of CNTs [60].

3.3 Methodology

The growth of CNTs carried out is done in catalytic CVD processes at low pressure. Prior to the growth step, either etched thin tungsten wire or $\langle 111 \rangle$ -oriented boron doped silicon with native SiO_2 layer is served as substrate for CNT growth. Chemical

containing catalyst for CVD growth is then coated on disposed substrate before proceeding to CVD process. Fig 3.2 shows a basic flow chart of the growth process in which thin tungsten wire is used as substrate. The flow chart of the growth process using silicon wafer as substrate is similar. The various growth parameters contributing in the CVD process are identified as follows:

- Influence of different catalysts used
- Concentration of catalyst in chemical solution
- Effective duration for CNT growth
- Precursor used
- Gas flow rate
- Temperature for growth
- Pressure for growth

The effects of influence of different catalysts used, duration of growth, catalyst concentration, and working temperature on growth will be studied in the following sections. In these experiments, only one growth parameter is varied at a time to observe and distinguish the effect of this individual parameter on the growth results of CNTs. The experiments which have resulted in satisfactory growth of CNTs are also repeated to ensure reproducibility.

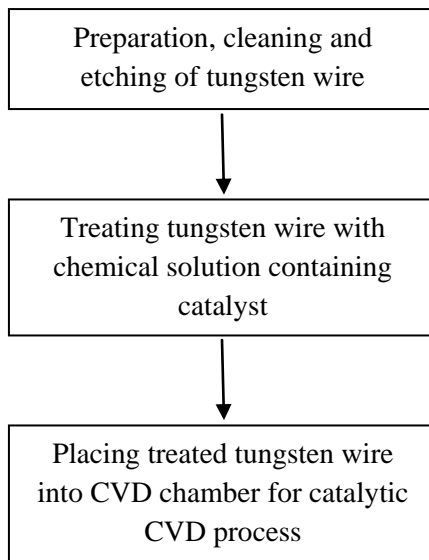


Fig 3. 2 Process flow for catalytic CVD growth of CNTs using tungsten wire as substrate

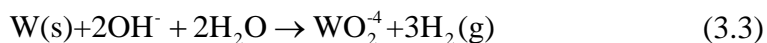
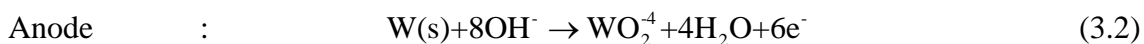
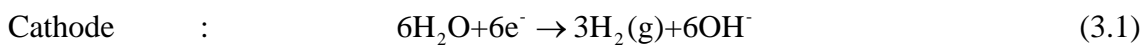
3.4 Experimental Setup

A succession of substrate treating and preparation processes antedates the effectual CVD growth. The using of tungsten tip as substrate is described for illustration here.

In the first place, tungsten wire is chosen as the primary substrate for growing CNTs which are to be electrically characterized in subsequent steps. A wire tip also enables more degrees of freedom in accessing and manipulating the CNTs in both SEM and TEM. Moreover, tungsten possesses very high melting point of about 3422 °C, which is way above the processing temperature of the growth process (~700-800 °C). If large areas of CNT films with specific patterns are desired, silicon wafer is used as substrate. <111>-oriented boron doped silicon with native SiO₂ layer is chosen to grow large areas of well aligned and ordered CNT films.

Tungsten wires are first etched at one end to achieve sharp tips. The diameter for these specific tungsten wires is 0.125 mm. Choosing this small value of diameter is to facilitate the later characterization in TEM since the depth of field in TEM is usually very small and hence for the purpose of easy manipulation and observation, the diameter of the tungsten wire on which the CNTs are grown should be small enough. Etching the tungsten wires serves partially for the above purpose; while the other purpose is to clean the surface of tungsten wire.

Tungsten wire is immersed 1-2 mm vertically into the premixed 10% potassium hydroxide (KOH) solution and acts as the anode in this electrolysis reaction. Bias is then applied across the electrodes, which causes tungsten wire to dissolve into the potassium hydroxide solution, which mainly takes place at the meniscus of the solution, such that the wire is etched at the meniscus and the lower part drops off, hence the tungsten wire tapers towards one end. The simplified chemistry behind the above electrochemical etching process is described in the following equations.



The tungsten undergoes an oxidative dissolution to tungstate anions (WO_2^{4-} in this case) and water is consumed to produce hydrogen gas during the etching process. Fig 3.3 shows the setup of etching equipment.

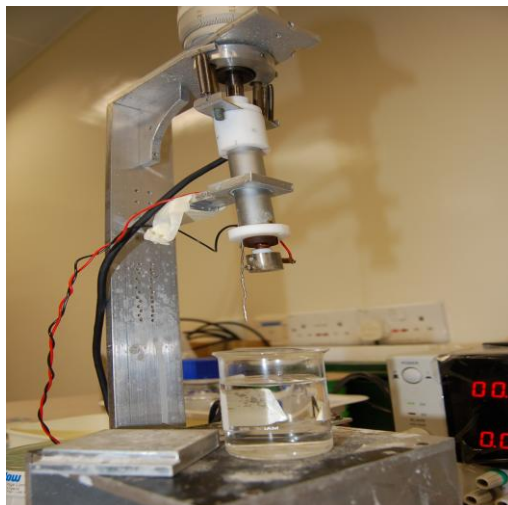


Fig 3. 3 Equipment setup for tungsten wire etching

Morphology of the tips after etching process shows different qualities of the resultant tips in Fig 3.4. The radius of curvature of the etched tip can not be either too small, inducing fragility of the tip during CVD process and undesirable vibration of the tip which disturbs the resolution of CNT resonance, or too large, which is not suitable for manipulation at nanoscale. Typically, values around tens of nanometers are desired in this project.

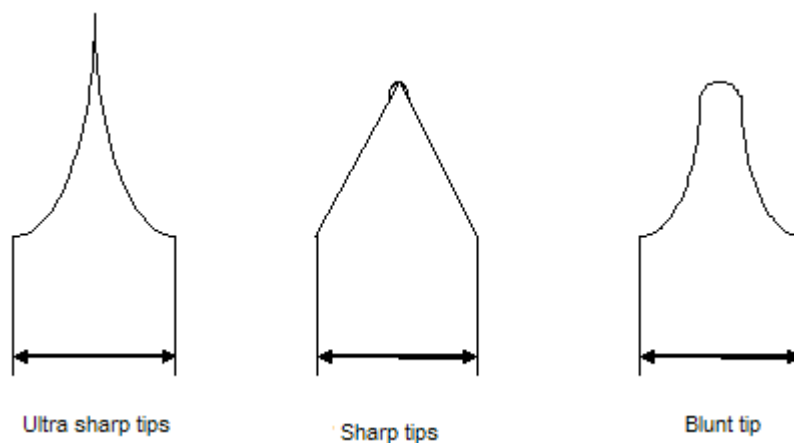


Fig 3. 4 Morphology of etched tungsten tips.

The tapered tungsten wires are then cleaned in a standard cleaning procedure by first immersing the wires in acetone for five-minutes ultrasonic cleaning to remove larger particles. It is then followed by immersing the wires into isopropyl alcohol (IPA) for another five-minutes ultrasonic cleaning to remove remaining smaller particles. The tips are then dried in the oven.

The catalyst used in the experiments for tungsten wire substrate is ferric chloride ($\text{FeCl}_3 \cdot 6\text{H}_2\text{O}$). The solid ferric chloride particles are dissolved in DI water and stirred in the ultrasonic bath for 15 minutes. The ultrasonic vibration helps expedite the dissolve process. The solution is then placed for 24hours until all the solutes are dissolved and a homogeneous aqueous solution in nut-brown is obtained.

The cleaned tungsten tips are then placed in a clean beaker and sufficient ferric chloride solution is added to cover these tips. These treated tips are then left in oven to dry at about $120\text{ }^\circ\text{C}$ for about 10 minutes.

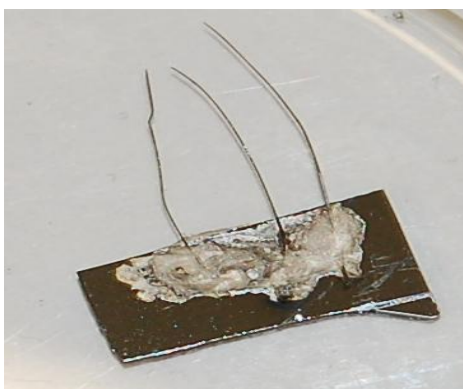


Fig 3. 5 Tapered tungsten tip mounted on silicon wafer for CVD process.

After the above treatments, these tips are mounted on silicon wafers by applying silver paint at the bulky end of these tips as shown in Fig 3.5. The mounted tips are then put

into CVD chamber for the catalytic CVD process, which will be discussed in details later.

Electron beam lithography (EBL) is used to design and edit the patterns on <111>-oriented boron doped silicon wafer. After EBL design and evaporation of catalyst materials in the evaporator, the silicon wafer is coated with catalyst materials in patterned regions and hence ready for subsequent CVD processing.

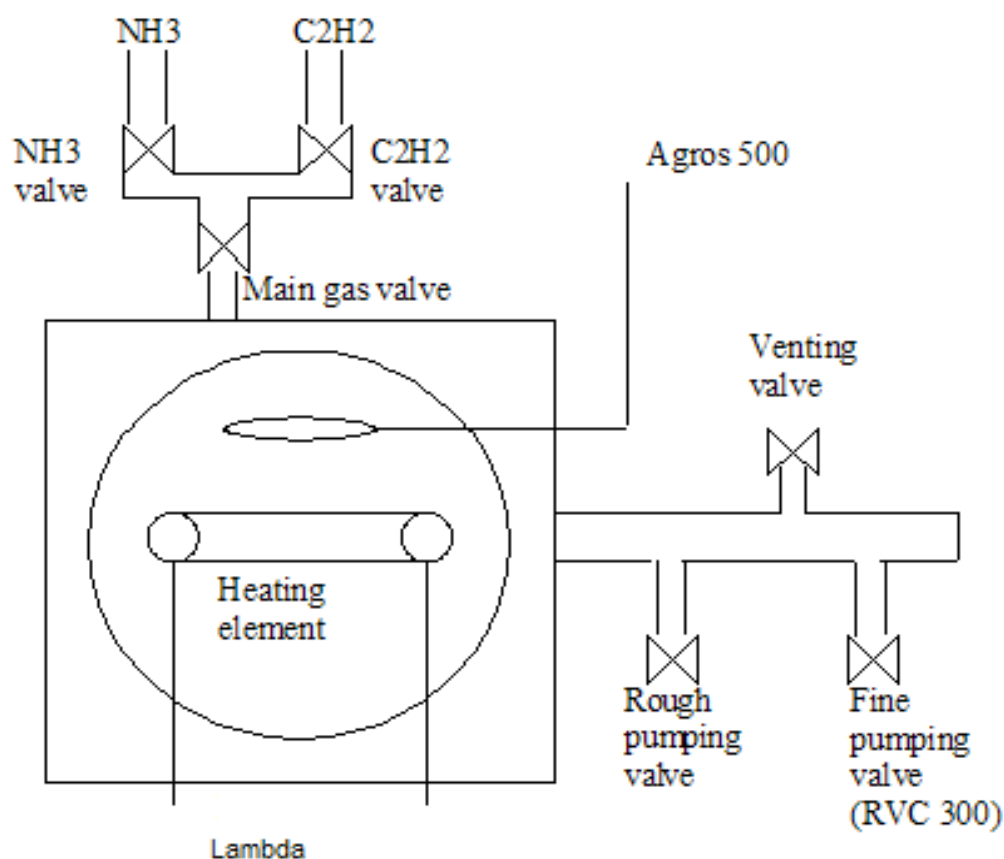
3.5 CVD growth of CNTs

In this project both thermal and plasma enhanced catalytic CVD methods are used to synthesize CNTs. The catalytic CVD process, which involves mainly the CVD chamber and its peripheral setup and connections, is the most practical method to create CNTs on extended surfaces. Both the side-view and top-view schematic diagrams of the CVD chamber used are shown in Fig 3.6.

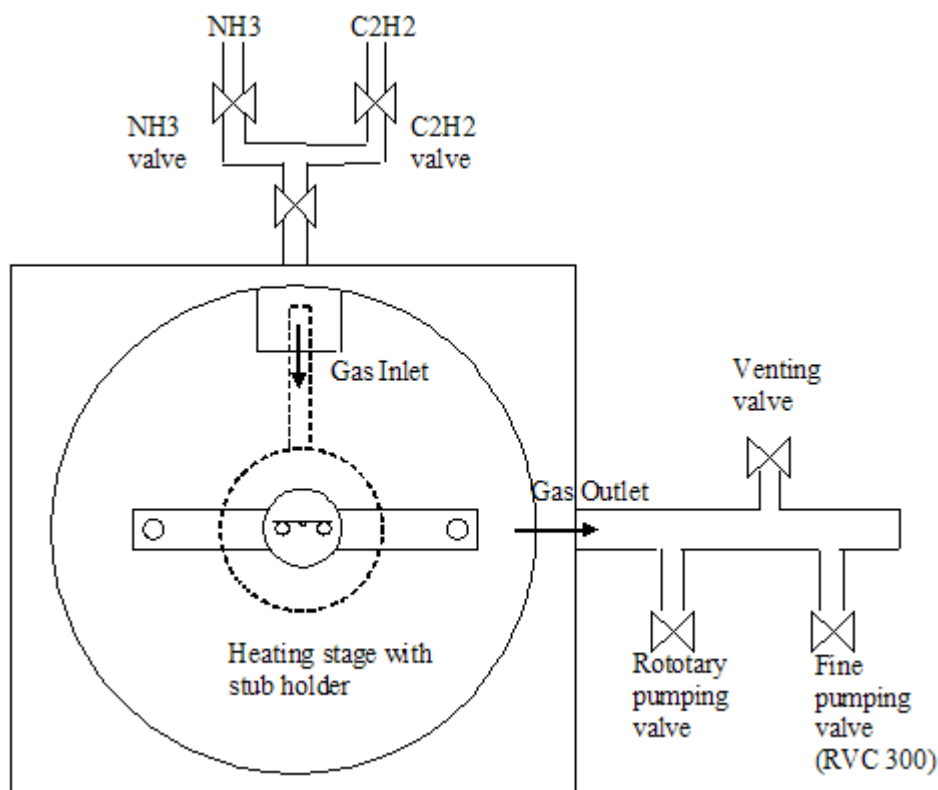
Both the flow rates (*sccm*) of NH_3 and C_2H_2 are controlled by the Matheson gas flow controller not shown in Fig 3.6. Temperature of the heating element is controlled by the Lambda which provides the current for the heating element. Plasma parameters are adjusted by Agros 500. Pressure in the chamber is controlled jointly by the rotary pump, fine (RVC 300) and rough pumping valve shown in Fig 3.6.

The whole general operation procedure conducted in the CVD chamber is as follows: Firstly, place the sample on the heating element and pump down the chamber by opening rough pumping valve, and the main gas valve. Meanwhile, set the flow rate for

both NH_3 and C_2H_2 via the Matheson controller. Once the pressure in the chamber reaches the base level, open the NH_3 gas valve to fill the chamber with NH_3 . Close the rough pumping valve and use the fine pumping valve (RVC 300) to adjust the pressure in the chamber to the required level. Afterwards, the element is heated up to the required temperature and the pyrometer is used to monitor the temperature on heating substrate. When growth temperature is reached, the C_2H_2 valve is opened to release the C_2H_2 gas into the chamber for CNT growth. In the PECVD procedure, Agros 500 is operated to adjust the plasma parameters at this stage. Once the duration for CNT growth is passed, the heating element is turned down slowly to off and C_2H_2 valve is turned off, which stops the growth process.



(a) Side-view of the CVD chamber



(b) Top-view of the CVD chamber

Fig 3. 6 Schematic diagrams of CVD chamber used in the experiments. Courtesy by and adapted from S. H. Lim.

After a period of cooling (usually 5-10 minutes), the NH_3 valve is closed. The rough pumping valve is opened to the largest to pump down the chamber in order to get rid of the NH_3 gas inside the chamber.

Once the base pressure is reached, the main gas valve and rough pumping valve are closed followed by shutting off the rotary pump and venting the chamber using the venting valve. The sample is then observed and characterized in Philips XL30FEG SEM as shown in Fig 3.7.



Fig 3. 7 Philips XL30 FEG scanning electron microscope

3.6 Morphology

In order to better understand the catalytic growth, parameters such as catalyst composition, deposition temperature, and catalyst concentration as well as deposition time are examined systematically in this section.

3.6.1 CVD process without catalyst

To confirm the catalyst's effect on growth result of CNTs, control experiments are done without coating any catalyst onto the tungsten wire. The growth parameters are as follows:

Table 3.1 Parameters for growth without catalyst

Substrate	Growth time	Catalyst	Temperature	Pressure	C ₂ H ₂ flow rate	NH ₃ flow rate
Tungsten wires	5 minutes	NIL	750°C	1.6mBar	5.5 sccm	60 sccm

Fig 3.8 shows the results of CVD process without catalyst indicated in Table 3.1. There is no CNT found on the surface of tungsten wire as shown in Fig 3.8.

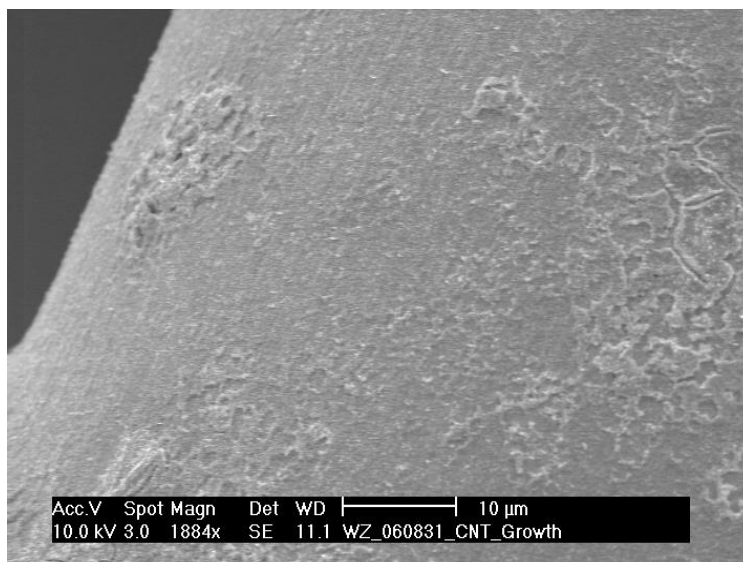


Fig 3. 8 Tungsten wire without catalyst after CVD process

Another PECVD experiment conducted on patterned silicon wafer can also help demonstrate and compare the effects of using and not using catalyst on the growth yield

of CNTs. The growth conditions are indicated in Table 3.2 and the growth results are shown in Fig 3.9.

Table 3.2 Parameters of PECVD process demonstrating effects of catalyst

Substrate	Growth time	Catalyst	Temperature	Pressure	C ₂ H ₂ flow rate	NH ₃ flow rate
Silicon wafer	5 minutes	Nickel (2nm thick)	750°C	1.6mBar	5.5 sccm	60 sccm

From Fig 3.9 distinct differences are observed between the growth yield on catalyst-coated patterns and the sterile glades. Well aligned CNT forests flourish on the patterns where catalyst (Ni) layer have been deposited; while almost very few CNTs appear on

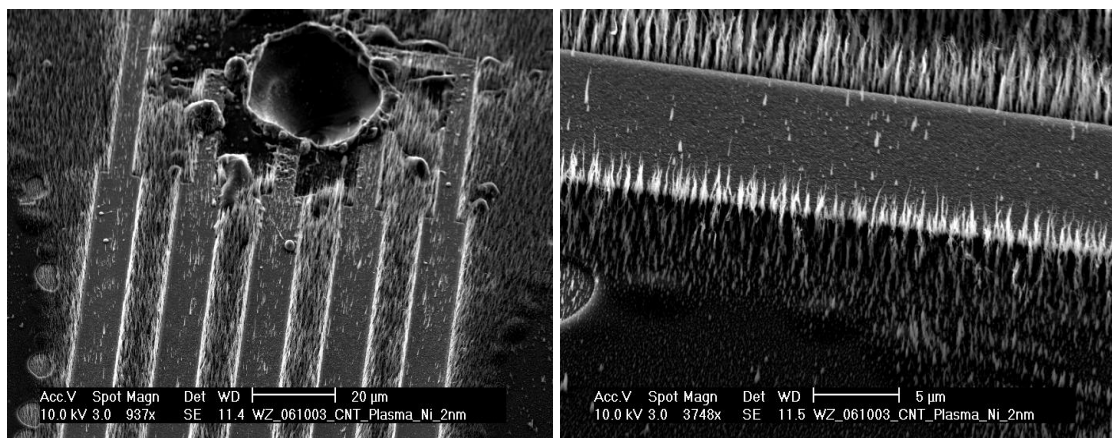


Fig 3. 9 Growth yields on catalyst-coated patterns and the sterile glades. (a) Well-aligned CNTs flourish on patterns of Ni layer with very few CNTs appear on unpatterned areas (b) Sporadic CNT-shape structures scatter on unpatterned areas due to sputtering of catalyst onto these areas during evaporation of catalyst layer

the surface areas among these patterns. Sporadic CNT-shape structures do scatter on the glades and this kind of exception is believed to be attributed to the sporadic sputtering of catalyst onto the unpatterned areas during evaporation of Ni layer, due to the relatively compact and narrow dimensions of predefined patterns on silicon wafer. The step of sputter depositing uses a sputter agent comprising argon. For sputtering applications in the low-pressure regime, argon has the additional advantages of high atomic mass (and hence greater effectiveness as a sputtering agent) and a low binary scattering cross section, with associated long mean free paths.

3.6.2 Influence of different kinds of catalysts

As displayed in Fig 3.10, it is found that the use of iron catalyst results in the best growth result of CNTs, whereas the use of a pure nickel catalyst results in inferior growth and zinc catalyst brings about the worst result. Although zinc is widely used as catalyst for synthesizing CNTs, ZnO nanostructures are shown to possess superior optoelectronic and piezoelectric properties useful in nanoscale transistors, sensors, electron emitters, and many other systems. The large-scale formation of heterojunctions of ZnO with other nanomaterials (particularly CNTs) should extend the scope of ZnO nanomaterials for potential applications. Although recent work has demonstrated the large-scale growth of aligned ZnO nanowire arrays, the formation of large-area ordered heterojunctions of ZnO nanostructures with other semiconducting materials such as CNTs has been much less discussed in the literature. In particular, the growth of aligned CNT–ZnO heterojunction arrays remains a big challenge. The potentially intimately

connected heterojunctions between the aligned CNTs and ZnO nanostructures might possess interesting optoelectronic properties attractive for many potential applications, including their use as electro-optic sensors and field emitters. Therefore, the possibility of using zinc as catalyst for synthesizing CNTs and synthesis of large-scale aligned CNT–ZnO heterojunctions is investigated in the thesis. Recently, water-assisted catalytic growth of aligned carbon nanotube–ZnO heterojunction arrays has been investigated by Dai Liming and his colleagues [82] .

As shown in Fig 3.10, the iron-catalyzed CNT exhibits long length and small diameter which enables it the desirable candidate for the subsequent experiments. The diameters for nickel-catalyzed CNTs with worm-like shapes are larger than the iron-catalyzed ones, while almost no CNTs appear on the zinc-catalyzed surface after CVD growth.

The result shown in Fig 3.10 is also consistent with a former study investigating potential CNT catalysts by examining the phase diagrams of a wide variety of metals conducted by C. P. Deck [61] . Deck suggested that the binary carbon phase diagrams of iron and nickel, both of which were found to be effective in catalyzing the growth of CNTs, were found to have distinct similarities not found with other elements such as zinc. The former two exhibited some carbon solubility (~0.5-1.0 wt. % carbon) in the solid solution within the temperature ranges studied (700-850°C).

	Growth time	5 minutes
--	--------------------	-----------

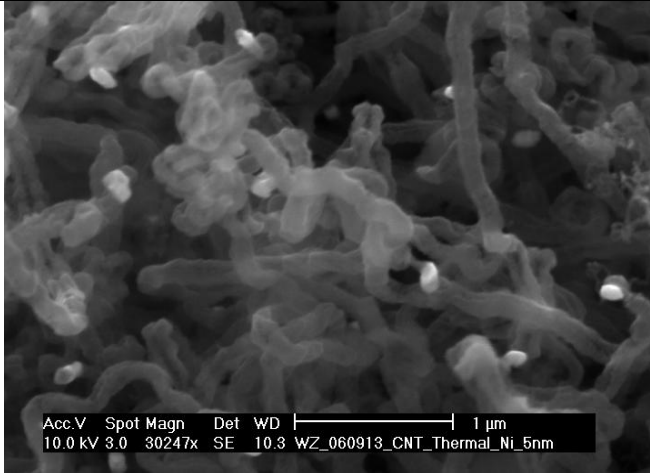
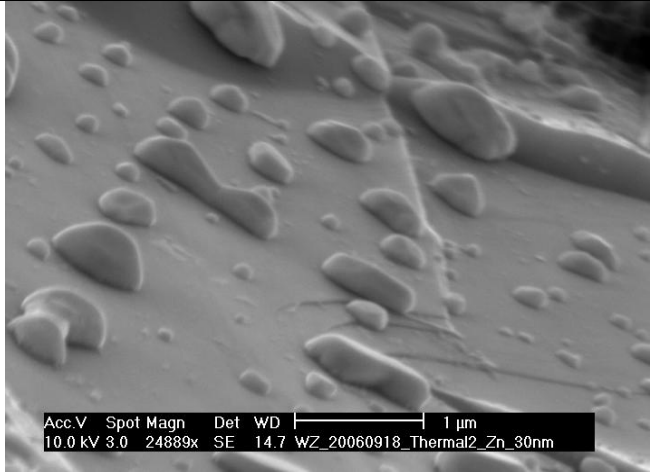
	Catalyst	Fe
	Temperature	750°C
	Pressure	1.6mBar
	C₂H₂ flow rate	5.5 sccm
 <p>Acc.V Spot Magn Det WD 1 μm 10.0 kV 3.0 30247x SE 10.3 WZ_060913_CNT_Thermal_Ni_5nm</p>	Growth time	5 minutes
	Catalyst	Ni
	Temperature	750°C
	Pressure	1.6mBar
	C₂H₂ flow rate	5.5 sccm
 <p>Acc.V Spot Magn Det WD 1 μm 10.0 kV 3.0 24889x SE 14.7 WZ_20060918_Thermal2_Zn_30nm</p>	Growth time	5 minutes
	Catalyst	Zn
	Temperature	750°C
	Pressure	1.6mBar
	C₂H₂ flow rate	5.5 sccm

Fig 3. 10 Effect of different catalysts on the CNT growth*

* Flow rate for NH₃ is 60 sccm for all three experiments.

Deck also pointed out those unsuccessful catalysts might have no significant solubility of carbon in the metals. In the carbon-zinc systems studied, the solubility limit of carbon in zinc is extremely low. Carbon cannot diffuse in significant quantities into the nanoscale catalyst particles, and therefore, these particles cannot act as nucleation sites for the formation of CNTs.

With other potential metal catalysts, sufficient carbon solubility can be observed in the solid solution; however, multiple carbides readily form. According to Deck [61] , graphite precipitation does not occur until the formation of all these carbides has occurred, and hence requires a much higher carbon concentration in the system. The time required for the kinetics of this carbon diffusion and carbide formation can delay or inhibit the graphite precipitation to an extent which prevents the formation of CNTs given the growth conditions used in these experiments.

Given the results attained in experiments described in Fig 3.10, iron is chosen as catalyst for CNT growth in this project.

3.6.3 Catalyst concentration

Ferric chloride solutions are prepared with four different densities, ascending from 0.2 *g/ml*, 0.5 *g/ml*, 1.0 *g/ml* to 1.2 *g/ml*, for investigating the effect of catalyst concentration on the CNT growth. Fig 3.11 shows clearly that the use of higher catalyst concentrations results in an increase of the resultant CNT density. But at concentrations higher than 1.0 *g/ml*, agglutination and agglomeration of CNTs appear. They do not

grow anymore as individual tubes but in larger clusters entangling with the others. This is surely not the ideal configuration for the study of the CNTs' properties in the subsequent experiments.

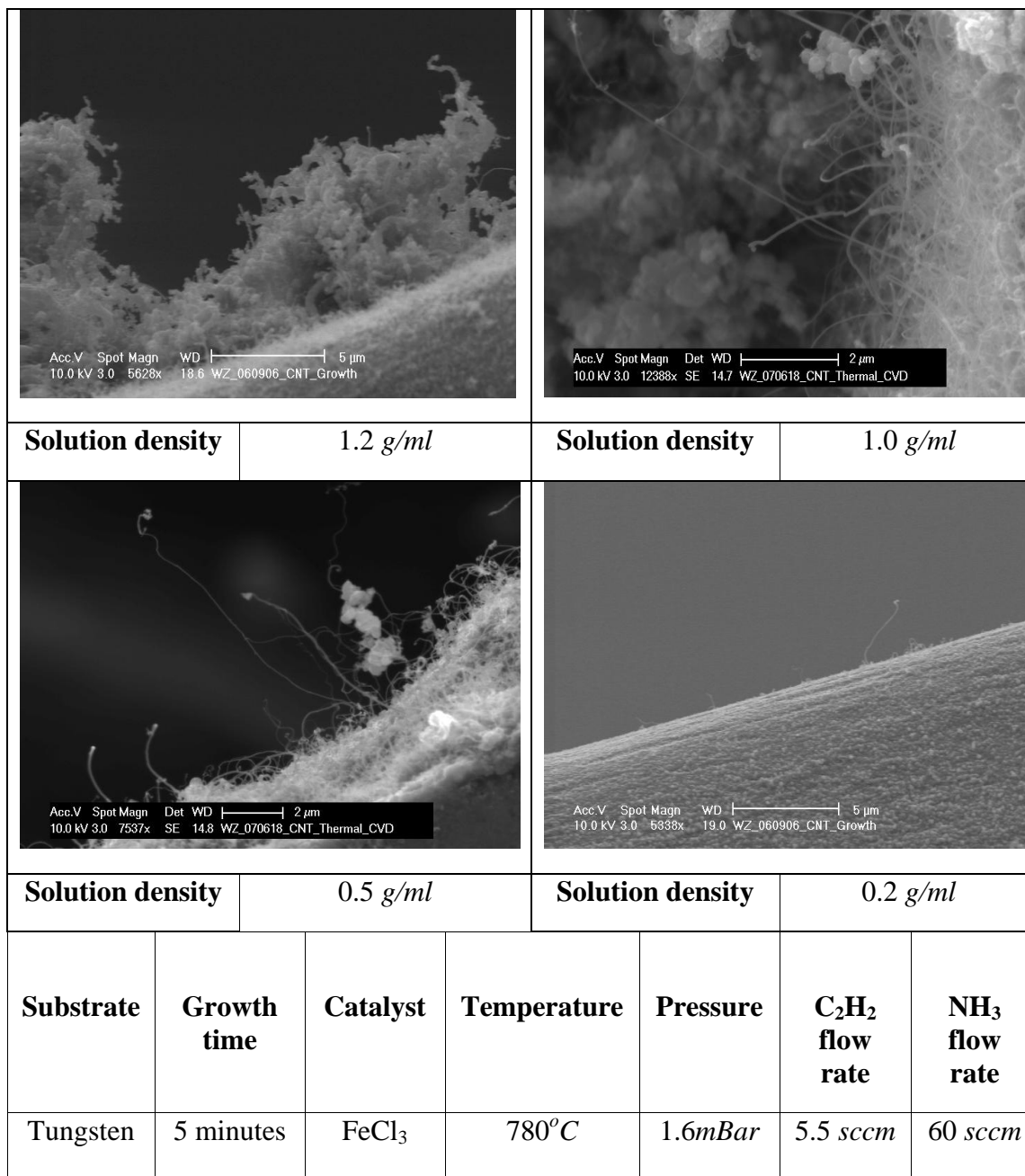


Fig 3. 11 Effect of concentration on CNT growth

In the successive experiments, the discussion is thus focused on the ferric chloride solution with a concentration of 1.0 g/ml, which exhibits the best result for CNT growth. Using catalyst of this concentration delivers the highest CNT density without clustering of the tubes as shown in Fig 3.11.

3.6.4 Growth duration

It was also found that the growth of the CNTs is a very fast process: under the prevailing conditions the growth already takes place during the first 5 minutes. Fig 3.12 shows the evolution of the CNT growth with time duration ranging from 2 minutes to 10 minutes at 780°C. After the initial annealing without CVD process, four identically prepared samples are separately subjected to CNT growth for 2 minutes, 5 minutes, 7 minutes and 10 minutes respectively, with all other parameters identical. In the first two minutes, CNTs have already started growing; whereas the average length is quite small ($\sim 3 \mu\text{m}$). Only 3 minutes later, CNTs of up to $10 \mu\text{m}$ in length are observed, which implies that the average growth rate is at least 40nm/s in this 3-minute interval. When growth duration is increased to 7 minutes, the average length of CNTs observed also significantly rises to around $30 \mu\text{m}$.

Nevertheless, it is also observed that these longer CNTs are also thicker in diameter, which is caused by the longer reaction time and hence more carbon deposition onto the tube. The long reaction time provides more carbon atoms to build up more layers of graphene walls in the axial direction, hence resulting in thicker diameter. The thicker diameter of CNT can also be due to amorphous carbon deposition. When the

hydrocarbon precursor gas undergoes thermal pyrolysis, undesired amorphous carbon is deposited on the outer wall of CNTs, contributing to the resultant thickening of the CNT.

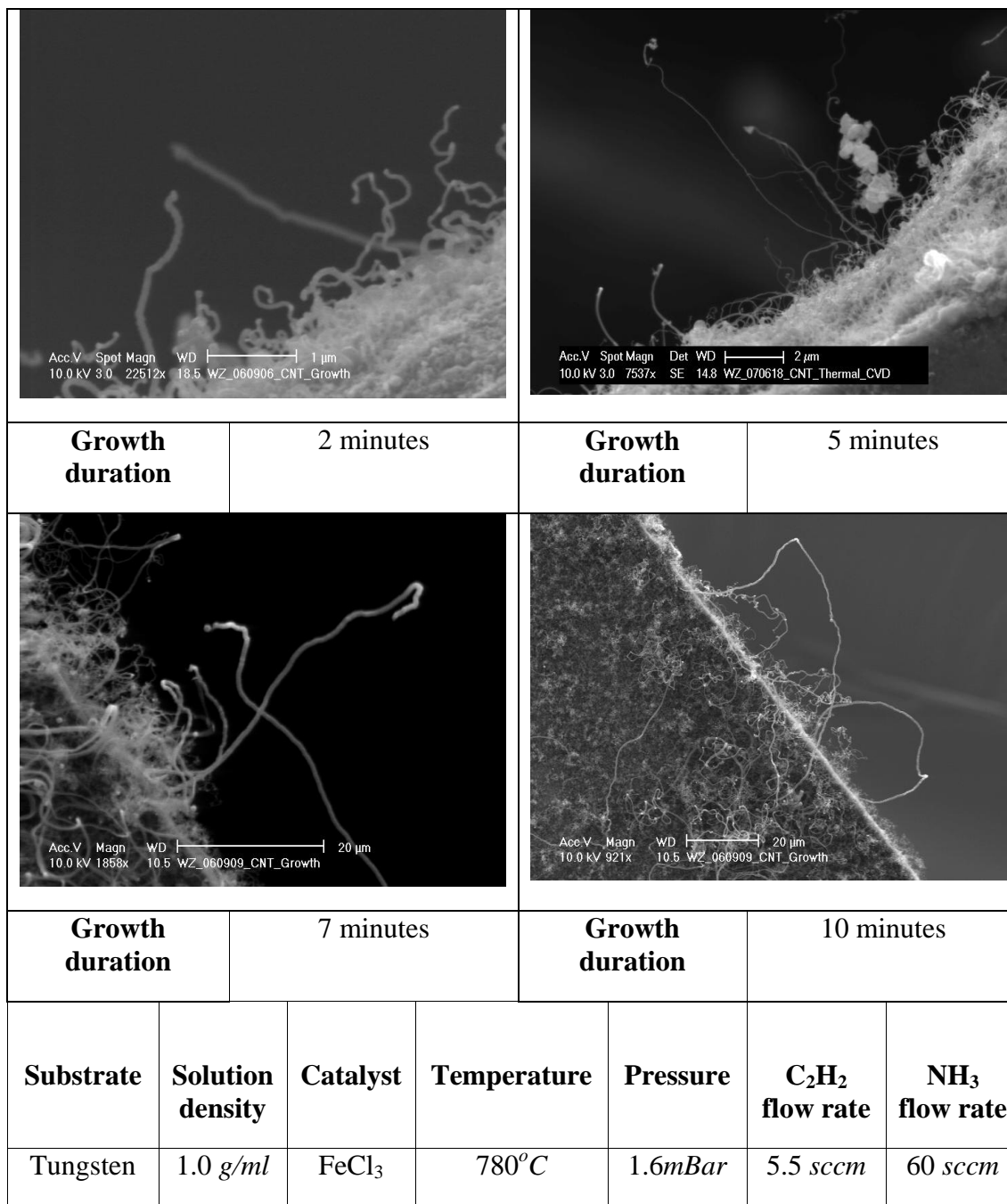


Fig 3. 12 Effect of duration time on CNT growth

When growth duration is further increased to 10 minutes, the freestanding CNTs become to pronate and fall down possibly because the mechanical structure of the CNTs can not sustain these long CNTs of 50 μm in average length or due to the pentagon-heptagon defects described in Chapter 2, which cause the CNT to bend towards the heptagon defects.

An even distribution of pentagon-heptagon defects in the structure of CNT will possibly form a coil shape nanotube, which is also observed in the experiment, as indicated by the arrows shown in Fig 3.13.

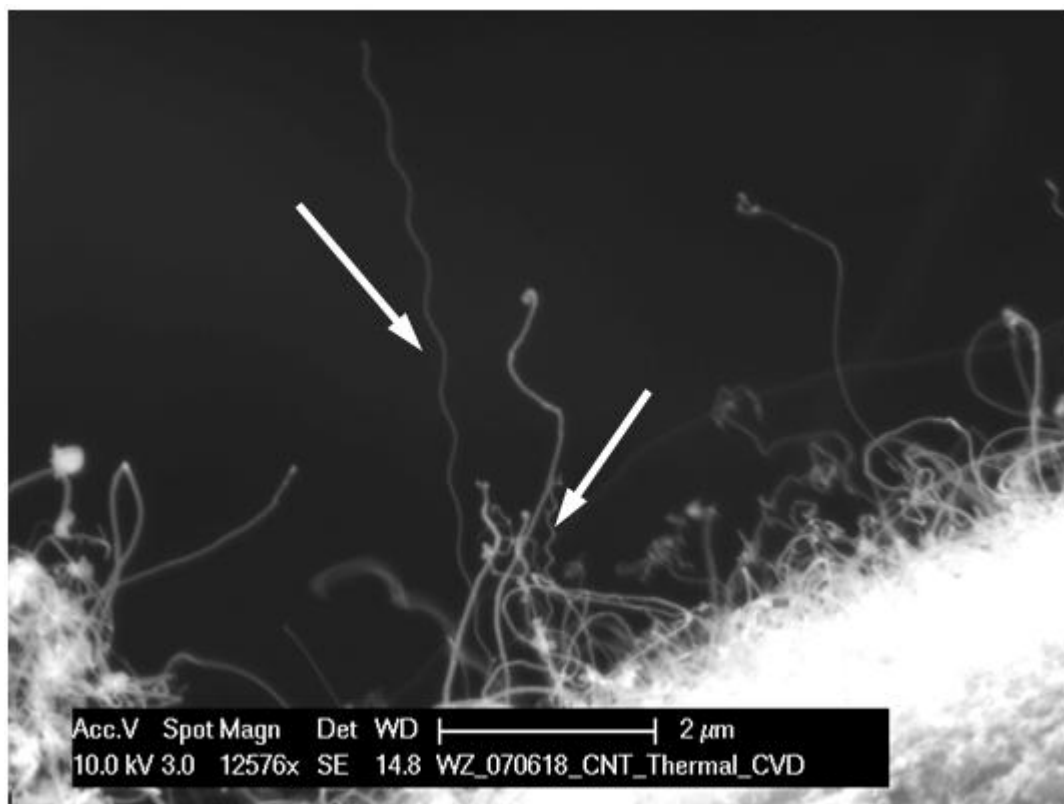


Fig 3. 13 Coil shape CNTs observed in experiments. Two coil shape CNTs, 8 μm and 2 μm in length respectively, are indicated by the arrows. The formation of coil shape is attributed to the even distribution of pentagon-heptagon defects in the structure of CNT, which cause the CNT to bend towards the heptagon.

For the subsequent electrical characterization, the optimal growth duration should be within the interval from 5 minutes to 7 minutes according to the results shown in Fig 3.12.

3.6.5 Growth temperature

Temperature is another crucial factor in thermal CVD synthesis of CNT because sufficient energy has to be afforded to the system to dissociate the hydrocarbon precursor gas so that subsequent reactions can take place. Fig 3.14 illustrates the effect of different temperatures on the growth result of CNTs.

CVD process at 650°C yields almost no obvious growth of CNTs, while the distribution density of CNTs is also sparse. This should be due to insufficient thermal energy available to the process, therefore precursor gas can not dissociate readily for the carbon supply crucial for the CNT growth. When temperature is increased to 780°C , long and upstanding CNTs are ample along the tungsten tips. Also the highest density of CNTs is observed at 780°C . Relatively thick structures are found at temperatures exceeding 800°C . When growth temperature is further elevated to 850°C , curly worm-like structures with dramatically increased diameters are observed along the tungsten tips. Acetylene starts to dissociate in the gas phase at temperatures above 800°C and the resultant carbon forms an amorphous continuous layer which also gets thicker with increased temperature.

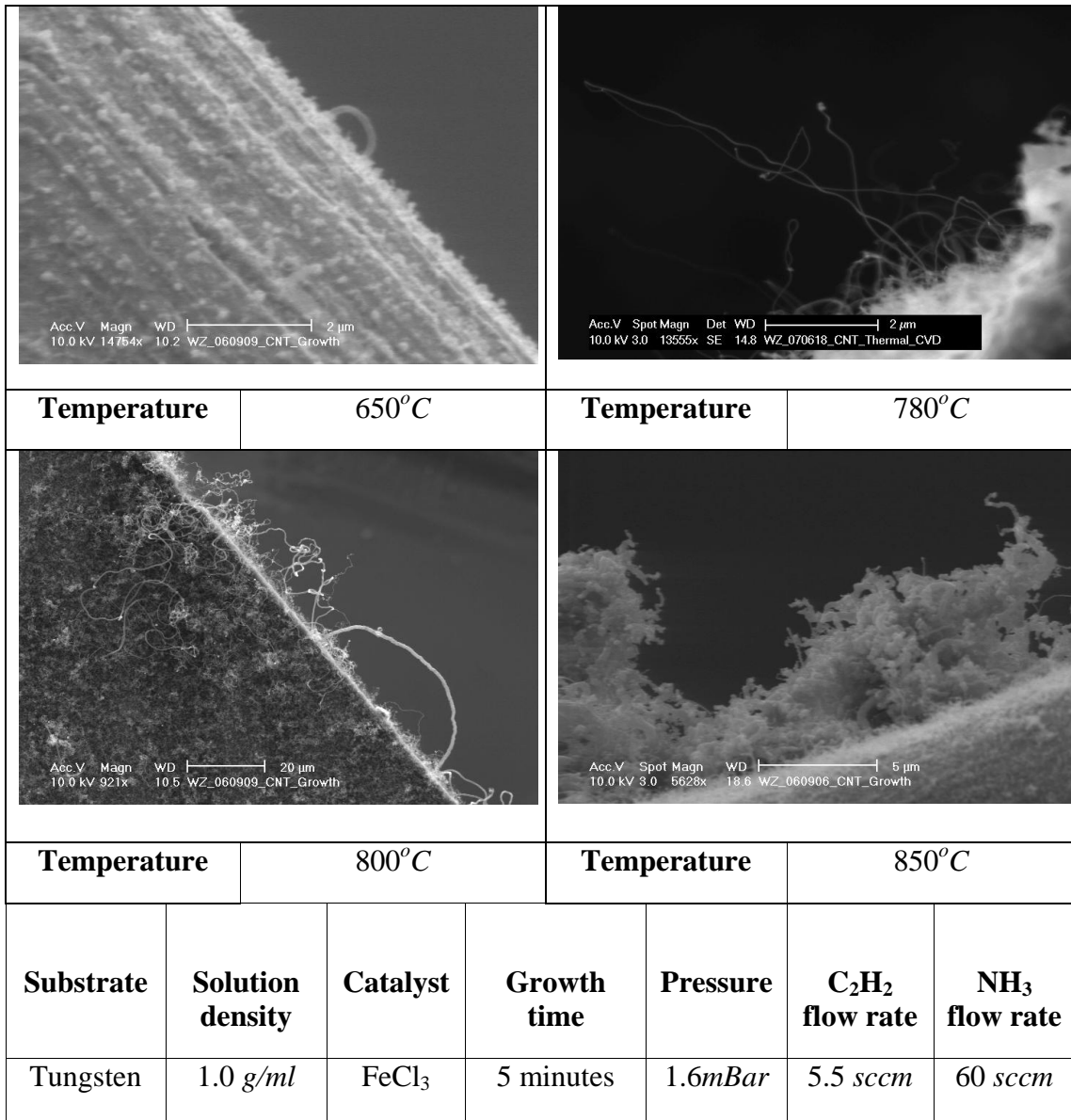


Fig 3. 14 Effect of temperature on CNT growth

Given the results shown in Fig 3.14, 780°C is chosen as the optimal temperature for growth of CNTs in this project.

3.7 PECVD growth of CNTs

Plasma-Enhanced Chemical Vapor Deposition (PECVD) is utilized since it allows the growth of oriented and aligned CNTs; meanwhile, the additional energy imparted by the plasma can effectually decrease the growth temperature required for thermal CVD, which is more compatible with the current standard semiconductor fabrication conditions.

A cleaned silicon wafer is coated with a thin metal film that serves to act as catalyst layer for CNTs growth, such as Ni, Fe, Co, using various physical deposition methods such as evaporation and sputtering. The coated samples are then placed onto the heating plate in the center of the PECVD chamber whose schematic diagram is shown in Fig 3.6, which is then pumped down to a low base pressure ($\sim 1\text{mBar}$) to evacuate atmospheric gas. The substrate is then heated to a temperature for annealing the sample in ammonia gas ambient. Hydrocarbon gas is introduced into the chamber through a network of mass flow controllers allowing to regulate the flow rate and gas composition of the mixture. A high voltage applied between the electrode above the sample and the ground causes the ionization of the gases, resulting in plasma formation. The energy from heating the substrate and from the high-voltage plasma causes decomposition of the hydrocarbon gas into its components. Although the exact growth mechanism of CNTs in PECVD process is not precisely known, one possible explanation is similar to the tip growth mechanism described previously in this chapter, which is also verified by the micrographs shown in Fig 3.15. Indeed, bright or dark catalyst particles in strong contrast to the CNTs are clearly seen at the tips of these CNTs in Fig 3.15.

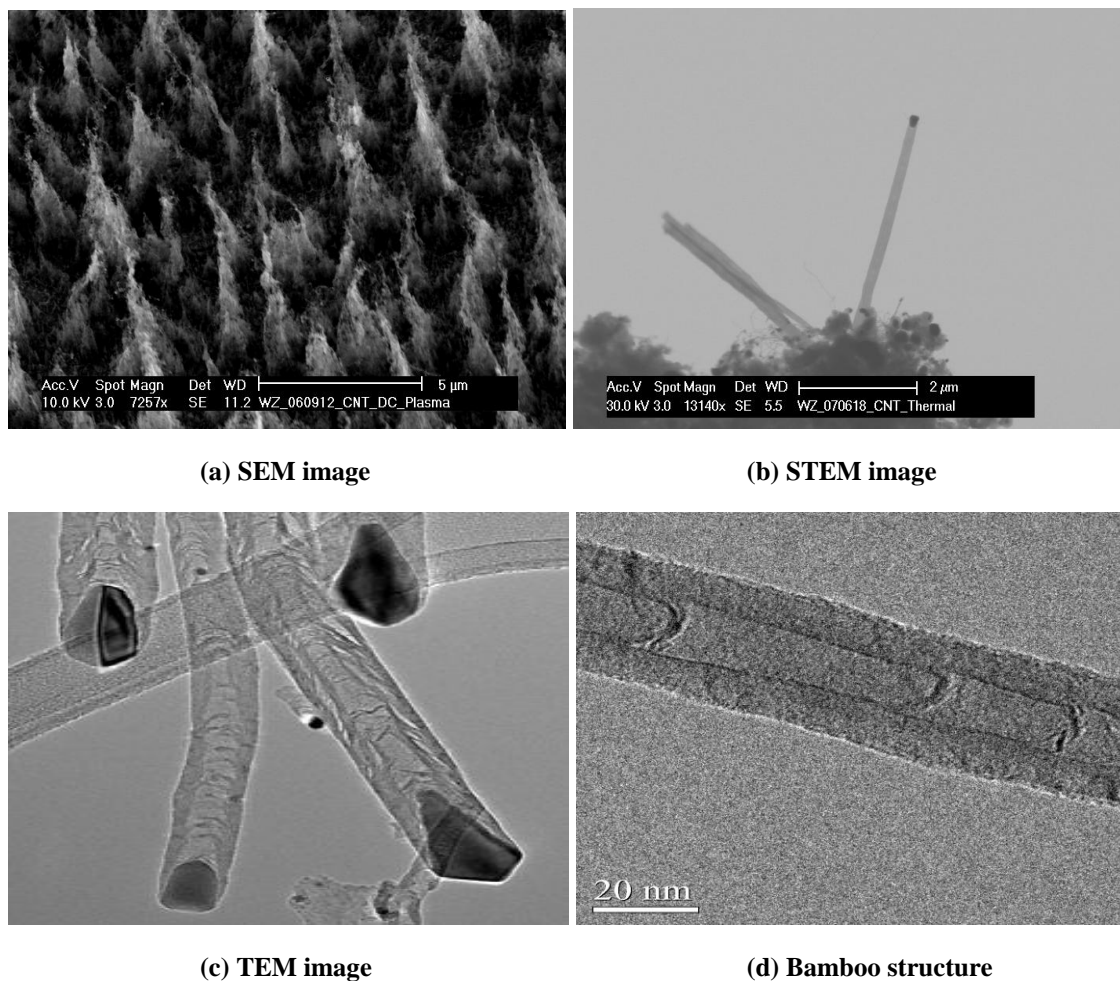


Fig 3. 15 Microscope images of PECVD-grown CNTs. (a) SEM image of aligned CNTs grown by PECVD. The bundles of CNTs appearing in Fig 3.15a are due to the weak van der Waals interaction that holds the individual CNT which is straight and perpendicular to the surface together in the bundle. (b) STEM and (c) TEM image show the catalyst dots at the tips of CNTs, indicating the “tip-growth” mechanism during this PECVD process (d) Bamboo-like structure caused by instable plasma field.

As observed in the SEM micrograph (Fig 3.15a), the electric field orientation of plasma affects the alignment of CNT growth and produces CNTs that are straight and perpendicular to the surface (The bundles of CNTs appearing in Fig 3.15a are due to the weak van der Waals interaction that holds them together in the bundle). In Fig 3.14a, b and c, catalyst dot appears at the tip end of the resultant CNT and hence implies a tip growth mechanism governing in this CVD process. From (c) and (d) in Fig 3.15, the

hollow inner bore of the CNTs is clearly seen under TEM observation. The inner bore shows regular compartment structures which suggest formations of bamboo-like CNTs [62]. This could be caused partially by the instability of the plasma field, which in turn induces the intermittent growth of CNTs and hence causes the defective structures of PECVD-grown CNTs in the experiments.

The walls of the CNTs in (c) and (d) of Fig 3.15 also appear to be wavy which suggests they are not perfect graphitic networks but only possess short-range graphitic order. The defects on the graphitic walls induce bending of the CNT walls. The defective wall structure of these CVD grown CNTs suggests tubes of possibly high electrical resistivity.

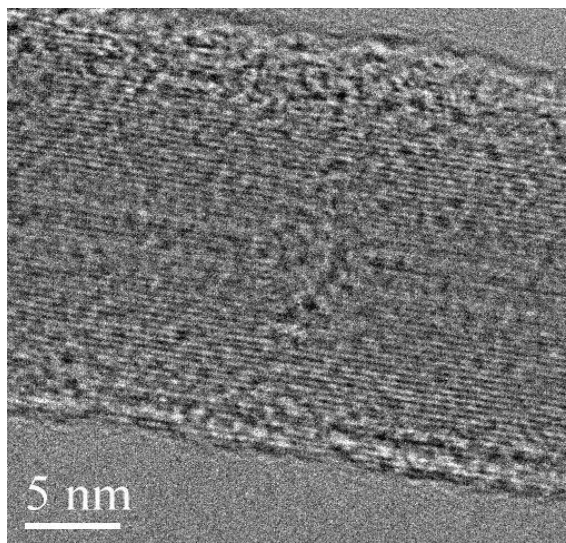


Fig 3. 16 TEM micrograph of commercial arc-discharge grown CNTs

Comparing the structures of PECVD-grown CNTs shown above with the structures of the commercial CNTs obtained from SES Research[®] shown in Fig 3.16, which are grown by the arc-discharge process, less defects and more homogeneous graphitic

networks possessing longer-range graphitic order are observed in the commercial CNTs. These commercial CNTs are typically 2-20 *nm* in diameter, with lengths ranging from 100 *nm*-2 μm , and have been treated to open the ends and to remove the catalyst nanoparticles. However these arc-discharge CNTs contain more amorphous carbon than the CVD grown CNTs which can render getting clean CNTs problematic.

3.8 Summary

To sum up, FeCl_3 solution provides the essential iron catalyst for the growth of CNT. With the concentration of catalyst increases, the density of grown CNTs increases. When duration of growth is elevated, longer CNTs are observed because the reaction time is longer for CNT to continue to grow. One undesirable result of longer growth time is the resultant thicker diameters of CNTs. While another critical issue of longer growth duration is the deposition of amorphous carbon layer. This undesirable deposition does not only affect the mechanical properties and performances of the CNT system as will be illustrated in later chapters, but will also possibly cause short circuits in potential devices and systems made from these CNTs. Temperature acts an important role in CNT growth as well. When growth temperature is low, the yield of CNTs is low and the distribution density of growth is sparse as well, possibly due to insufficient energy available for the dissociation of hydrocarbon gas and hence the impeded growth process. On the other hand, when the growth temperature is too high, the morphology and distribution density of the resultant CNTs are also undesirable. The resultant structures possess relatively larger diameters compared to those grown at lower

temperatures. 780 °C is chosen as the optimal temperature for CNT growth in the experiments.

Recently, PECVD has emerged as a key growth technique to produce vertically-aligned CNTs, possessing the advantage to grow well oriented CNTs at lower temperatures compared to previous thermal CVD process, which makes PECVD a potential nanofabrication technique compatible with current semiconductor technology. However, PECVD-grown CNTs suffer structures with more defects and less uniformity compared to thermal-grown CNTs. Many critical issues need to be addressed and solved before PECVD becomes the mainstream technique for mass production of applications integrated with CNTs.

Last but not least, the size of catalyst particle also plays a vital role in the morphology of the CNT grown via catalytic CVD process. As noted already by researchers studying carbon filaments in the 1970s [60] , the diameter of CVD-grown structures is controlled to a large extent by the catalyst particle. In order to obtain monodisperse CNTs, well-defined catalyst particles need to be assembled or delivered onto a surface. The average size of the CNTs is difficult to control with the method adopted in the experiments previously shown and the size distribution is relatively broad. This is due primarily to the fact that the catalyst particles are formed from a thin film evaporated or from ions in solution during annealing to the growth temperature, which makes the purveyance of small and monodisperse particles problematic. Recently, a new approach is demonstrated which allows to obtain CNTs of well-defined diameter by using the iron-containing cores of ferritin as catalyst [81] . Possibly the most remarkable property of the ferritin catalyst is that the outer CNT diameter matches closely the particle

diameter, which facilitates the control of the diameter distribution of the grown CNTs. However, due to the limit in the experimental facilities, investigations on either the effect of catalyst particle size or the utilization of ferritin as catalyst are not implemented in this project.

CHAPTER 4

FABRICATION, DETECTION AND CHARACTERIZATION OF CARBON NANOTUBE RESONATOR

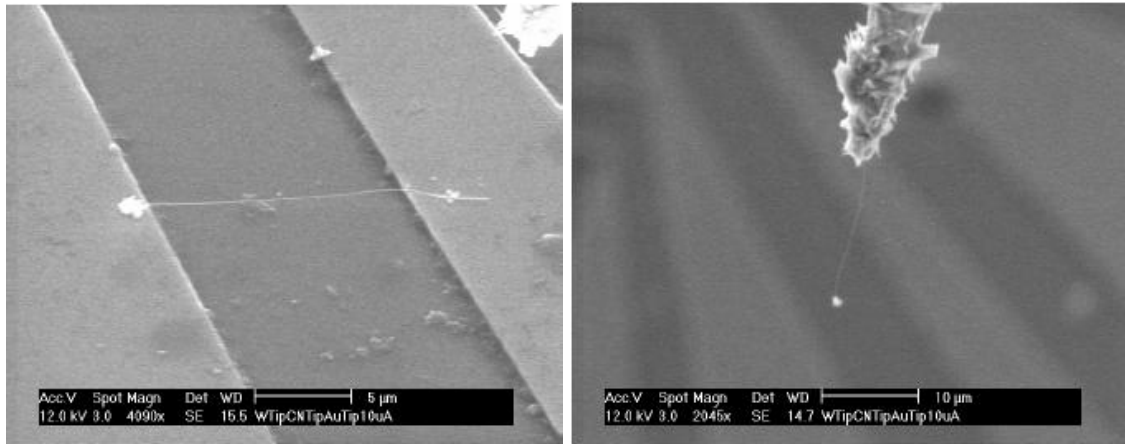
4.1 Introduction

Due to the extremely small sizes, it is difficult to realize a nanotube-based resonator with conventional actuation and detection methods such as optical and magneto-motive techniques. Besides, in face of the theoretically predicated resonant frequencies around gigahertz, inducing and detecting the motion of the vibrating element at such high resonant frequencies becomes a potentially critical challenge. Despite these challenges, nanotube-based resonators in both cantilever and doubly-clamped configurations have been realized and reported [49] [50] [53]

In this chapter, method for electrical actuation and *in situ* harmonic detection of electrically induced mechanical resonance of single MWNT cantilever is described first. *In situ* investigation of performance of cantilevered CNT resonator prototype under DC and AC bias in SEM is conducted. Details of the experimental setup and the device fabrication (section 4.2), actuation and detection techniques (section 4.3), and experimental results for characterizing the CNT resonator system (section 4.4) are also investigated in this chapter.

4.2 Experimental setup and device fabrication

Two types of configurations for CNT resonators, bridged or doubly clamped and cantilevered as shown in Fig. 4.1, are implemented in this project. Discussions will be focused mainly on resonators consisting of suspended CNTs in cantilever geometry in this thesis for the amplitude of motion is relatively larger in cantilever geometry, which facilitates the observation. There are three major parts in fabrication of both types of CNT resonator: 1) growing tubes, 2) making electrical contacts and 3) suspending the CNT (or pulling out and placing the CNT).



(a) Bridged resonator

(b) Cantilevered resonator

Fig 4. 1 Two types of configurations for single CNT resonator

The growth procedures have been investigated in Chapter 3 in details. The rest two steps will be addressed in the following sections.

4.2.1 Making contacts and pulling out the CNT

Once the CVD grown CNTs are available, they are put into Philips XL-30 FEG SEM facilitated with a three-axes nanomanipulator (Kleindiek MM3A) with two arms as shown in Fig 4.2. The biasing and tapping of electrical signals are accessed by ports located outside the XL-30 SEM connected to each arm of the nanomanipulator through a controlling circuit board.

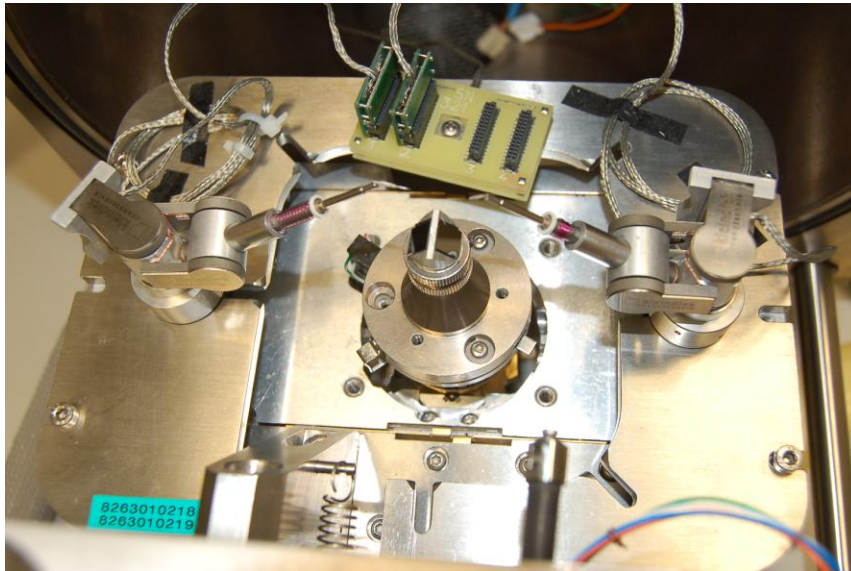


Fig 4. 2 Nanomanipulators mounted onto the SEM

To obtain free-standing CNTs the wafer or tungsten tips with CVD grown CNTs are placed onto a carbon tape fixed on the central stage in the SEM. Two electrochemically etched tungsten tips are mounted onto both arms of the nanomanipulator. To conduct investigations on CNT resonator, well-separated individual protruding CNTs are desired. To pick up a single CNT from the CNT forest, one of the electrochemically etched tungsten tips is adjusted to the vicinity of the protruding end of the chosen CNT, i.e., a

long, straight and thin tube that is uniform in its diameter, points in the direction of the tip, and stands sufficiently free from other tubes to allow being approached as shown in Fig 4.3a and the free end of the chosen CNT is indicated by the black arrow in Fig 4.3a.



Fig 4. 3 Contacting between tungsten tip and CNT and pulling-out of CNT. (a) Long, straight and thin tube that is uniform in its diameter, points in the direction of the tip, and stands sufficiently free from other tubes to allow being approached (b) Free-standing end of the bent CNT sticks to the tungsten tip a few micrometers from the tip apex (c) CNT is aligned with the tip by pulling out the tube (d) Pulled-out CNT in the cantilever geometry with the new free end which is broken from the original tube indicated by black arrow

When the tip has approached the carbon nanotube within a few hundreds of nanometers, the nanotube usually bends and sticks onto the tip. This bending possibly indicates charging on the nanotube due to the electron beam radiation. Applying a voltage difference later between the tip and the nanotube sample can show increase in the amount of bending and deflection of the tube as shown in Fig 4.4.

To provide sufficient contact surface between the tip and the nanotube for convenience of subsequent pulling-out process, the tungsten tip is first positioned about a micrometer beside the nanotube and then the nanotube is carefully approached from the side. As the nanotube bends, its free-standing end sticks to the tip a few micrometers from the tip apex, as shown in Fig 4.3b. By pulling, the nanotube is to some extent aligned with the tip and a contact length of about $3\ \mu\text{m}$ is obtained, as indicated by the black arrow in Fig 4.3c. During this approach-and-contact procedure, whether a contact really happens can also be verified by monitoring the voltage on the Keithley 237 Source Measurement Unit connected to the nanomanipulator which is set to operate in constant current mode ($0.3\ \mu\text{A}$) with the voltage compliance of $15\ \text{V}$ in addition to the visual observation in SEM. Successful initial contact of the nanotube is indicated by a drop in the voltage, to a value typically greater than $1\ \text{V}$. The relatively large equivalent resistance of the circuit is largely due to the contact not ideal enough between the CNT and the tungsten tip. The high contact resistance can also be associated with poor mechanical adhesion between the CNT and the tip, for small pulling force might render separation between nanotube and tungsten tip at this joint which foils the pulling-out attempt and subsequent experiments.

Four methods, current welding, electron beam induced deposition (EBID), use of Van der Waals force and use of electric attractive force, are utilized for realizing and improving desirable contacts between chosen CNTs and the tungsten tip or even between two CNTs for the subsequent pulling-out and electrical characterization of CNT cantilever.

4.2.1.1 Current welding

To improve the contact, the current is ramped up to 10 μA , for instance, and back down to the test current of 0.3 μA for evaluating the resistance in the current welding process. Improvement in the contact is indicated by a much smaller voltage drop. If no obvious improvement is observed, the current ramping procedure with a higher current is conducted for further improvement. This discreet multi-step current ramping procedure is implemented intentionally to avert the occurrence of CNT arcing or burn-out [63] that can arise, despite the preset voltage compliance, with a single high current ramp if the initial contact is poor. This kind of unanticipated break-off incidence does happen actually in the experiments as shown in Fig 4.3d. Breaking off part of the nanotube from the main sample occurs by Joule heating even with a current of 20 μA , which indicates a current density larger than $6 \times 10^{10} A/m^2$ for a tube with a radius of 10 nm. Although the reported maximum current density for MWNT can be as high as $10^{13} A/m^2$ [64], one possible reason for the low current conveyance capacity in the experiments can be the presence of defects in these CVD grown CNTs' structures as shown in Chapter 3. The presence of carbon contamination, which is conductive, induced by

electron beam inside the SEM, might also cause a sudden current spike that can possibly exceed the current carrying capacity of the CNT, thus rendering the breaking off of this CNT due to the sudden aggrandizement in current flow. When a final current ramp indicating an acceptable improvement in contact completes the current welding process, the welded CNT is then pulled out from the substrate for further processing.

4.2.1.2 EBID of carbonaceous substance

Although the inextricable electron beam induced deposition (EBID) entangling with characterization of samples in SEM is undesirable occasionally, such as the damaging short circuit caused by EBID of amorphous carbon outside the nanotubes occurring in the current welding attempt of pulling out the nanotubes, EBID of this carbon film can also contribute distinguishingly in enhancing the contact between the nanotubes and tungsten tips.

When the initial contact between nanotubes and tungsten tips is achieved by approaching tungsten tips toward carbon nanotubes (Fig 4.4a), the field of vision in the SEM is then zoomed in to the contact region between the nanotube and the surface of the tungsten tip (Fig 4.4b). Selective area slow scan is conducted within the contact region and a carbon film is then deposited onto the contact region to fix the CNT to the tip (Fig 4.4c & d). This carbon film acts as a paste that anchors the CNT onto the tip. The deposition is realized by the electron beam dissociation of contaminants, mainly hydrocarbon molecules, inside the SEM chamber.

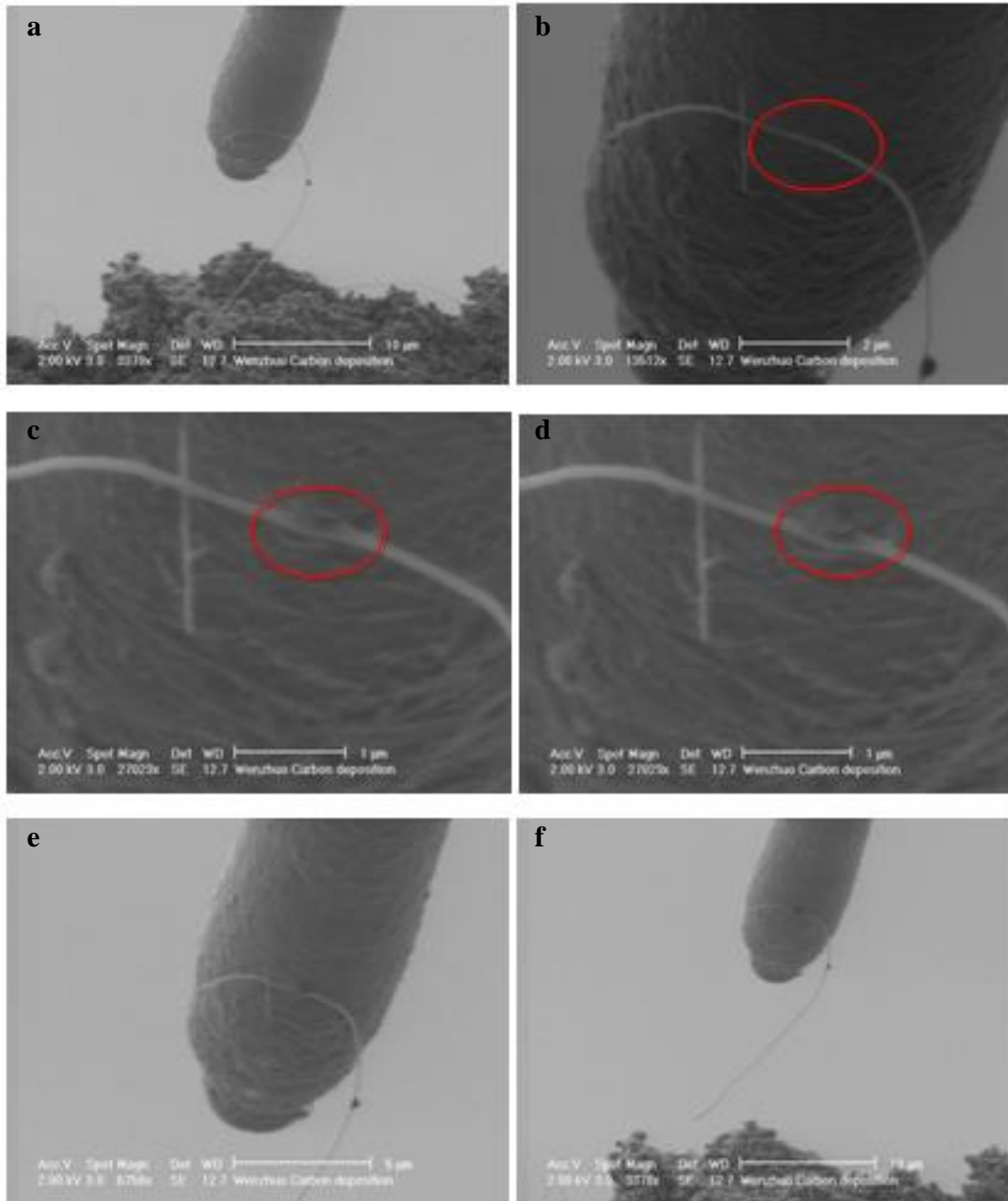


Fig 4. 4 EBID of carbonaceous substance to improve the contact between the CNTs and tungsten tips. (a) Initial contact between nanotubes and tungsten tips is achieved by approaching tungsten tips toward carbon nanotubes (b) Selective area viewing the contact region between the nanotube and the surface of the tungsten tip in SEM (c) (d) Selective area slow scan is conducted within the contact region and a carbon deposition is observed on the contact region to fix the carbon nanotube to the tip (e) EBID welding finished (f) CNT is pulled away from the substrate and becomes a nanocantilever along the supporting tungsten tips.

After the deposition, this nanotube is pulled away from the substrate and becomes a nano-cantilever along the supporting tungsten tips (Fig 4.4e & f). Although the above EBID soldering is conducted parochially, intending to deposit the carbonaceous substance within the restricted region, as indicated by the red circles in Fig4.4, as well as avoiding contaminating the whole carbon nanotube, the contamination often coats an area broader than the visual field selected. This might damage the structure and cause changes in mechanical properties of the whole CNT system by introducing exotic and additional substance to the CNT investigated. This undesired effect will be characterized and discussed further in Chapter 5 when the resonant oscillation of CNT cantilever is investigated.

The doubly-clamped CNT resonator can also be implemented in this EBID method as shown in Fig 4.5. A free-standing CNT attached to the tungsten tip is brought to the patterned electrodes as shown in Fig 4.5a and b. The free end of this CNT is first anchored to the electrode via EBID of carbonaceous substance; the whole CNT is then placed and aligned across the trench to touch onto the other electrode while this end of CNT is also fixed by EBID of carbon layer, as shown in Fig 4.5c, d, e and f.

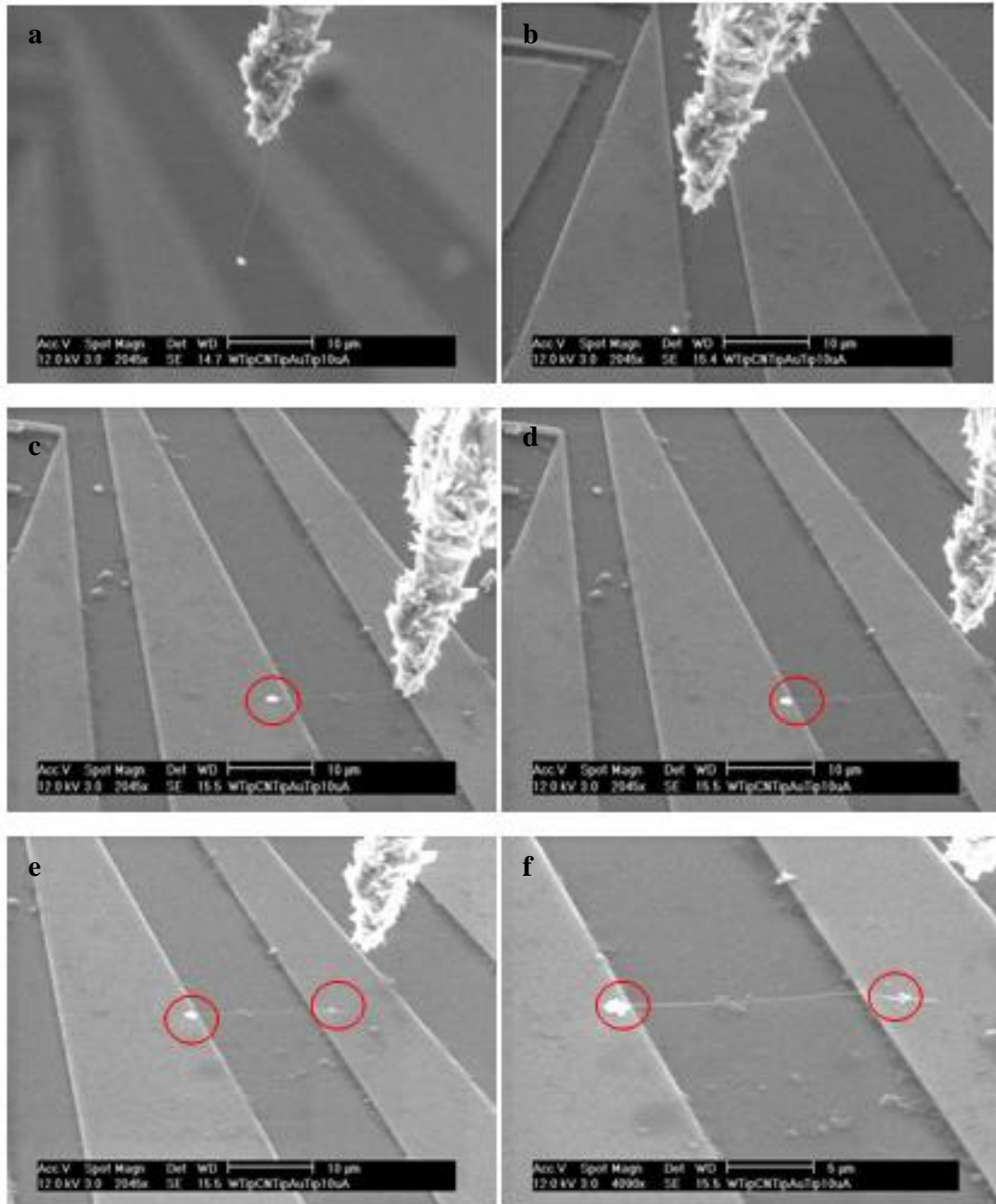


Fig 4. 5 Doubly-clamped CNT resonator implemented via EBID method. (a) (b) A free-standing CNT attached to the tungsten tip is brought to the patterned electrodes (c) The free end of CNT is anchored to the electrode via EBID of carbonaceous substance (d) The whole CNT is placed and aligned across the trench to touch onto the other electrode (e) The other end of CNT is also fixed by EBID of carbon layer (f) Doubly-clamped CNT resonator after EBID process.

4.2.1.3 Use of Van der Waals force

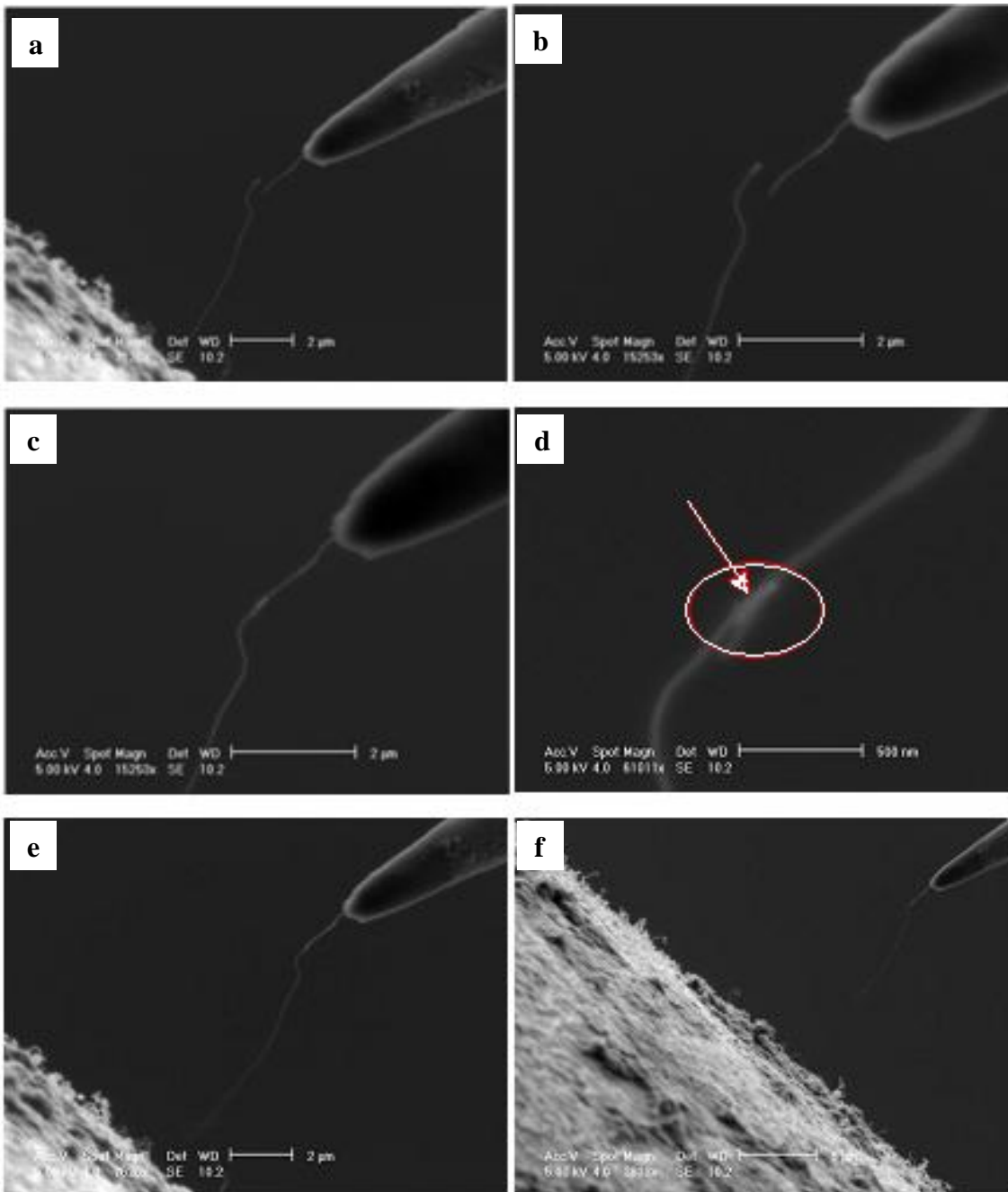


Fig 4. 6 Pulling out CNT via Van der Waals force (a) One tungsten tip with a short CNT at the tip is approaching to another long, free-standing CNT (b) The short CNT tip is placed approaching the free end of the new long CNT (c) These two CNTs are attracted to each other by the Van der Waals force (d) The arrow indicates the new connection and contact region between the two CNT tips formed via Van der Waals force (e) (f) The long CNT is pulled out and a longer CNT tip consisting of two individual CNTs is formed.

The utilization of Van de Waals force in manipulating CNT in a desired way can be illustrated by pulling out one long CNT through a previously attained short CNT to increase the length of the CNT tip, as shown in Fig 4.6. One tungsten tip with a short CNT along the direction of the tip, which is achieved after breaking-off of a long CNT via current welding as described previously, is approaching to another long, free-standing CNT as shown in Fig 4.6a. The short CNT tip is then placed approaching the free end of the new long CNT (Fig 4.6b) and these two CNTs are attracted to each other by the Van der Waals force, as shown in Fig 4.6c and d. The arrow in Fig 4.6d indicates the new connection and contact region between the two CNT tips formed via Van der Waals force. The long CNT is then pulled out and a longer CNT tip consisting of two individual CNTs is formed (Fig 4.6e and f). In this method, neither external electrical bias nor selected area slow scan is needed. However, this kind of contact achieved by Van der Waals force is not as strong as the one made in previous two methods. Usually in the experiment, CNT picked up via this method exhibits poor contact and is susceptible to external disturbance such as movement of the tungsten tip and even the scan by electron beam during image acquisition.

4.2.1.4 Use of electric attractive force

A dc electric voltage around 5 V is applied between a new CNT on the substrate and the CNT tip on tungsten tip achieved after process described in 4.2.1.3 as shown in Fig 4.7.

The tips of these two CNTs are indicated by arrows shown in Fig 4.7a and b. The tips of these two CNTs are attracted to each other by electric attractive force and a new

connection is established within the circled contact region. This new CNT is then pulled out as shown in Fig 4.7d. A CNT loop is also formed in Fig 4.7d due to the vibration of the free end of the long CNT and the attraction of this end by the biased tungsten tip.

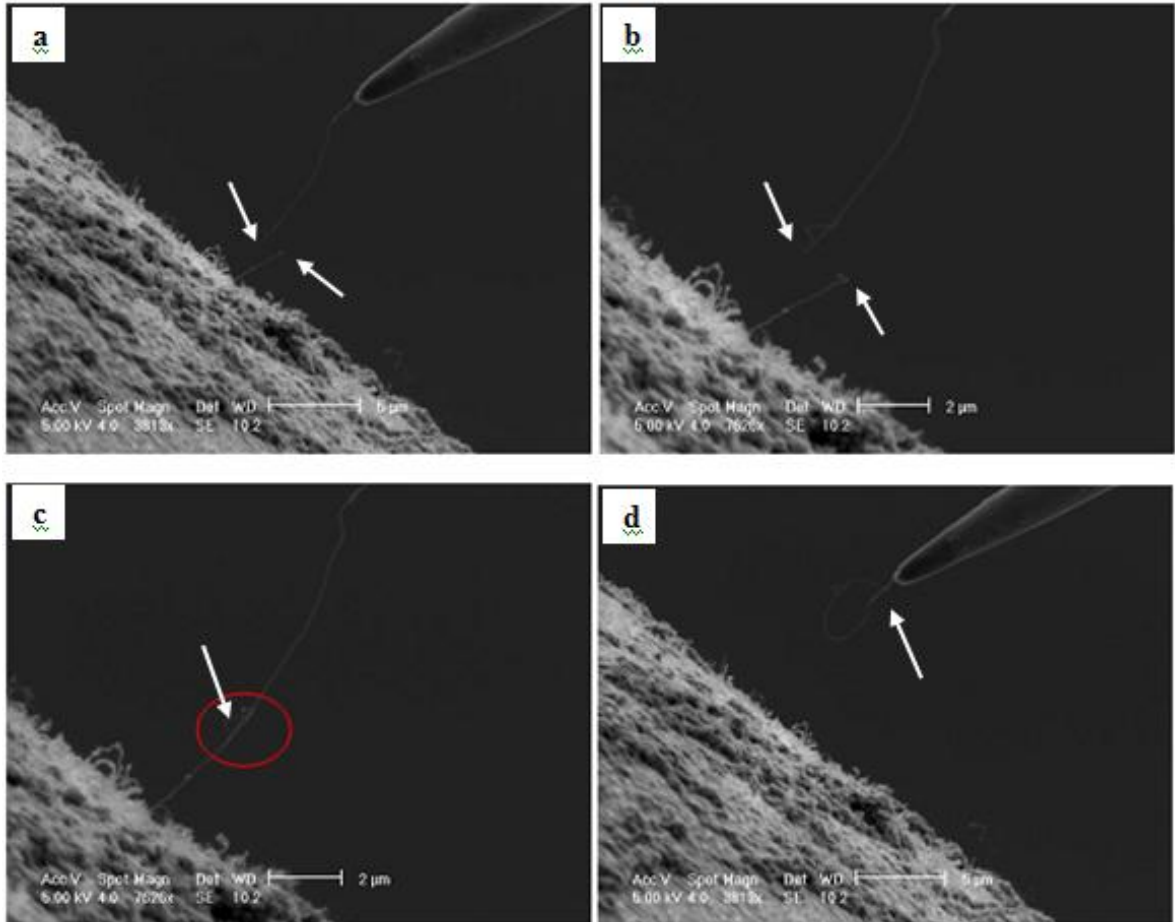


Fig 4. 7 Use of electric attractive force for pulling out CNT (a) (b) The tips of the two CNTs are indicated by arrows. A dc electric voltage around 5 V is applied between a new CNT on the substrate and the CNT tip on tungsten tip. (c) The tips of these two CNTs are attracted to each other by electric attractive force and a new connection is established within the red-circled contact region (d) The new CNT is pulled out and a CNT loop is also formed by the vibration of the free end of the long CNT end and the attraction of this end by the biased tungsten tip.

These above four methods enable us to select individual CNT from the CVD grown CNT samples and fabricate nano-cantilever and nano-resonator consisting of a single CNT.

4.3 Actuation and detection

4.3.1 Actuation setup

The nanotube motion is actuated through electrostatic interactions by biasing the counter electrode and the CNT. Experimental setup for harmonic actuation of electrically induced mechanical resonance in an individual MWNT resonator is illustrated in Fig 4.8. The counter electrode is approached to the vicinity of the free end of the MWNT. A dc bias and an ac signal from a sine wave signal generator, which generates the oscillating electric field, are applied between the nanotube and the counter electrode. By tuning the frequency of the ac signal, the cantilevered nanotube can be excited such that maximum amplitude is achieved when the frequency of the drive signal matches the mechanical resonance frequency of the nanotube cantilever system.

The amplitude of dc voltage is first set to 5 V in order to enhance the amplitude of the potential oscillation of the nanotube while this amplitude is varied later to investigate the relationship between dc bias and the oscillation; the V_{p-p} value of ac bias, on the other hand, is set to the achievable minimum value (50 mV) in order to minimize the intervention of the oscillating field on the electron beam and hence optimize the image quality observed and acquired, for increase in the V_{p-p} value of ac bias is found to render the deterioration of blurring appearing in the SEM images.

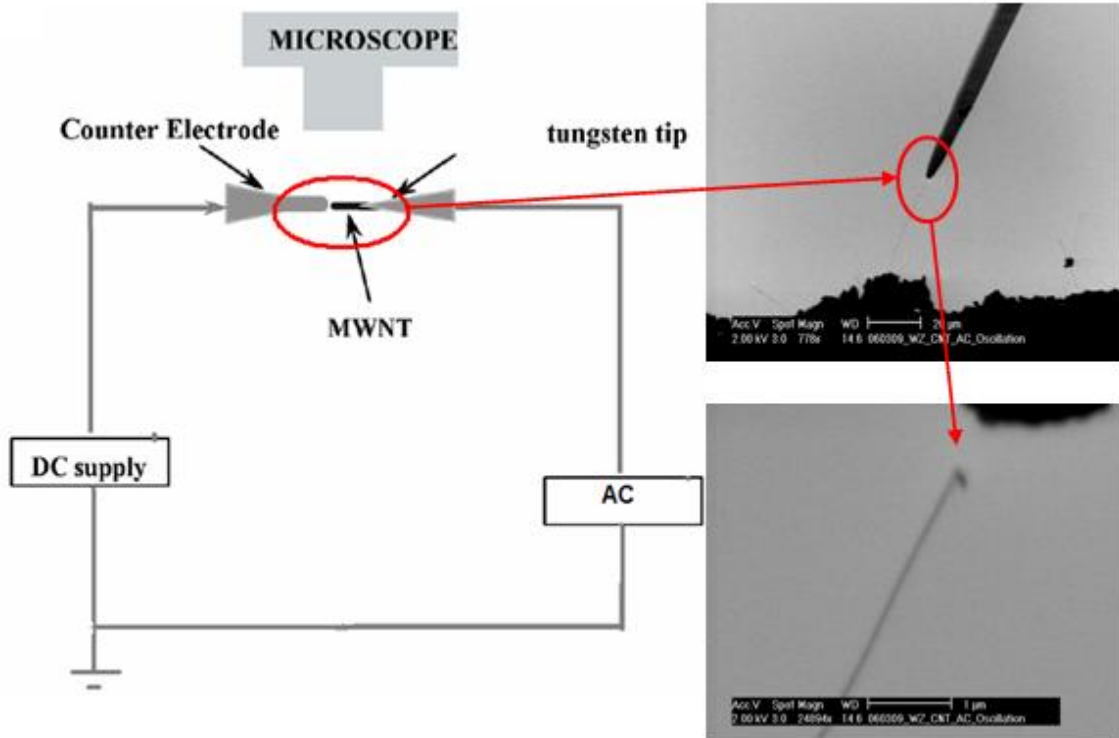


Fig 4. 8 Experimental setup for harmonic actuation of electrically induced mechanical resonance in an individual MWNT resonator. A dc bias and an ac signal from a sine wave signal generator, which generates the oscillating electric field, are applied between the nanotube and the counter electrode. Visual observation is conducted directly in SEM.

4.3.2 Detection setup

The *in situ* observation of nanotube oscillation is first conducted in the TV mode of XL 30 FEG SEM. This mode of acquisition allows watch the resonance in the SEM chamber live.

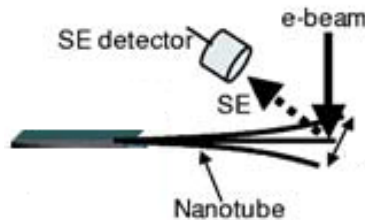


Fig 4. 9 Schematic of the experimental setup for oscillating nanotubes

When resonance is reached, in order to probe the oscillation and determine the amplitude of resonance of the nanotube, an electron beam with beam diameter of less than 1 nm is focused using an integrated mode onto the nanotube which protrudes from the supporting substrate as shown in Fig 4.9. The attributes of resonance can be acquired visually when the laterally resonating nanotube traverses the electron beam. This technique provides direct measurement and determination of oscillating frequency and amplitude of the nanotube.

4.4 Experimental results of CNT resonator system

The electrically induced mechanical resonance of CNT resonator can be characterized with the aid of nanomanipulator and SEM. To determine the atomic structure parameters which are of crucial importance to the oscillation of CNT resonator, TEM is utilized to conduct further investigations after the initial SEM characterization.

4.4.1 Observation and characterization of oscillation in SEM

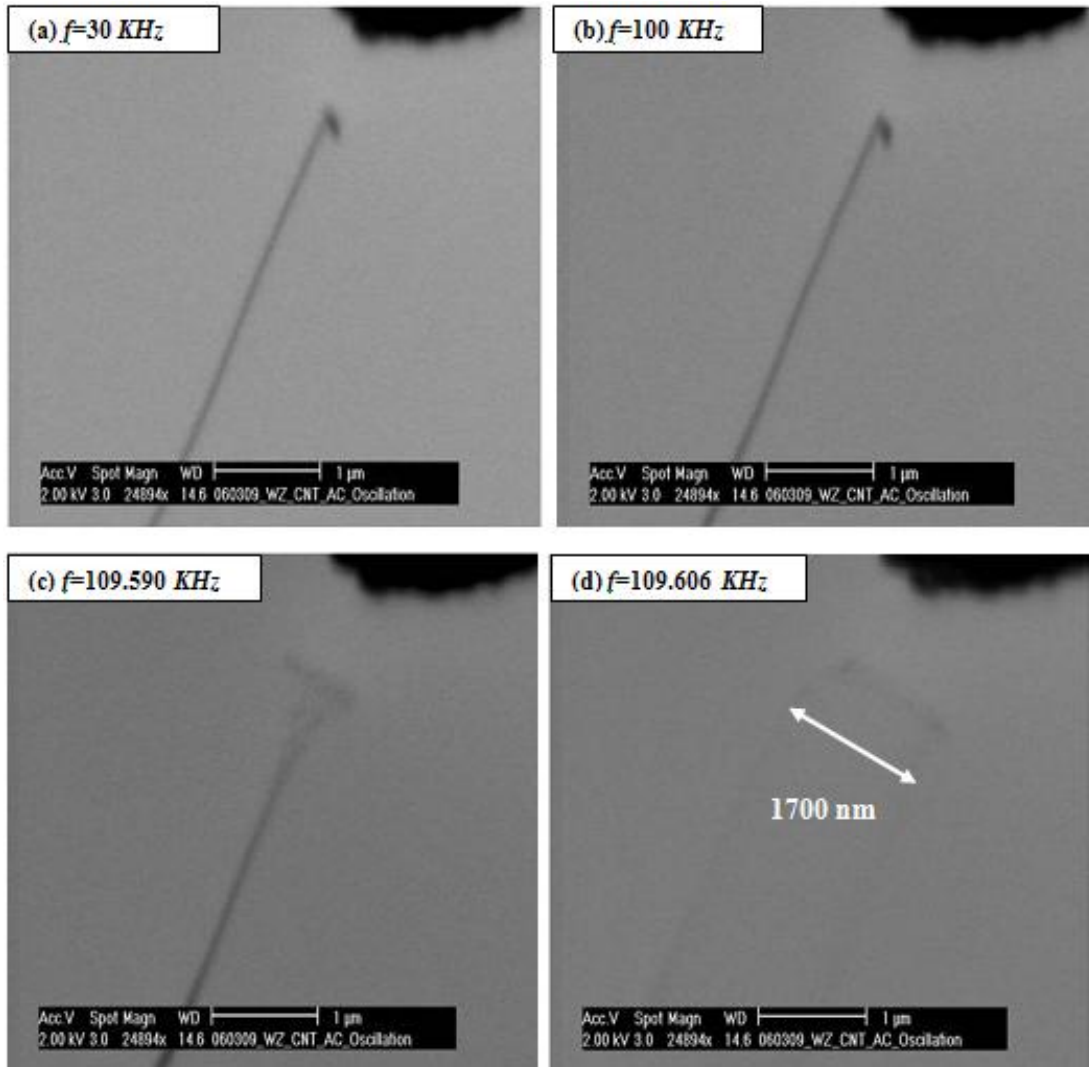
4.4.1.1 Forward process and resonance peak observed

The frequency of the ac bias is first increased (forward process) in the hope to observe the oscillations of the implemented CNT resonator. The initial amplitude of dc bias is 5 V and keeps constant in this forward process. The V_{p-p} value of the ac signal is 50 mV. The frequency is increased from hertz range up to megahertz range. Eight selected frequencies along this forward process out of the acquired data points are illustrated in

Fig 4.10. The maximum amplitude of oscillation observed appears at the actuating frequency of 109.608 *KHz* as seen from Fig 4.10d. For frequencies smaller than this value, the amplitude of oscillation increases corresponding to the increase in frequency value, as shown from Fig 4.10a to d; while a small increase of 2 *Hz* above this value causes an dramatic decrease in oscillation amplitude and further increase renders more distinct drop in amplitude till almost complete cease of oscillation which can be seen from Fig 4.10e to h. The amplitude-frequency curve acquired accordingly shows the typical Lorentzian shape for a fundamental mode resonance centered at $f=109.608$ *KHz* as shown in Fig 4.11; according to the full-width-at-half-height (FWHH) value, the quality factor Q is 9743 for this nanotube resonator, which is consistent with the quality factors, in the range of 10^3 - 10^5 , with which typical NEMS operate. These values are much higher than those typically available with electronic oscillators, but still inferior to MEMS counterparts.

Recently, the quality factor for the nanotube cantilever has been theoretically predicted based on molecular dynamics simulation for a SWNT and a double wall nanotube [65]. The predicted Q factors are smaller than 1500 at room temperature. In that case, however, the examined nanotubes were very short which were around 2 *nm* in length; therefore the resonant frequency roared up to 10^{12} *Hz*. That value of frequency is comparable to the phonon frequency. Therefore, the oscillation energy may easily couple with the phonons and can be converted into phonon oscillation. This coupling thus raises the system temperature and the energy for the oscillation has to be dissipated. On the contrary, resonant frequencies under the experimental conditions in this project are lower than 1 *MHz*, which differs greatly from the theoretical calculation and

therefore the quality factor takes a higher value resulting from the effective conservation of the oscillation energy compared to that theoretical calculation [65] .



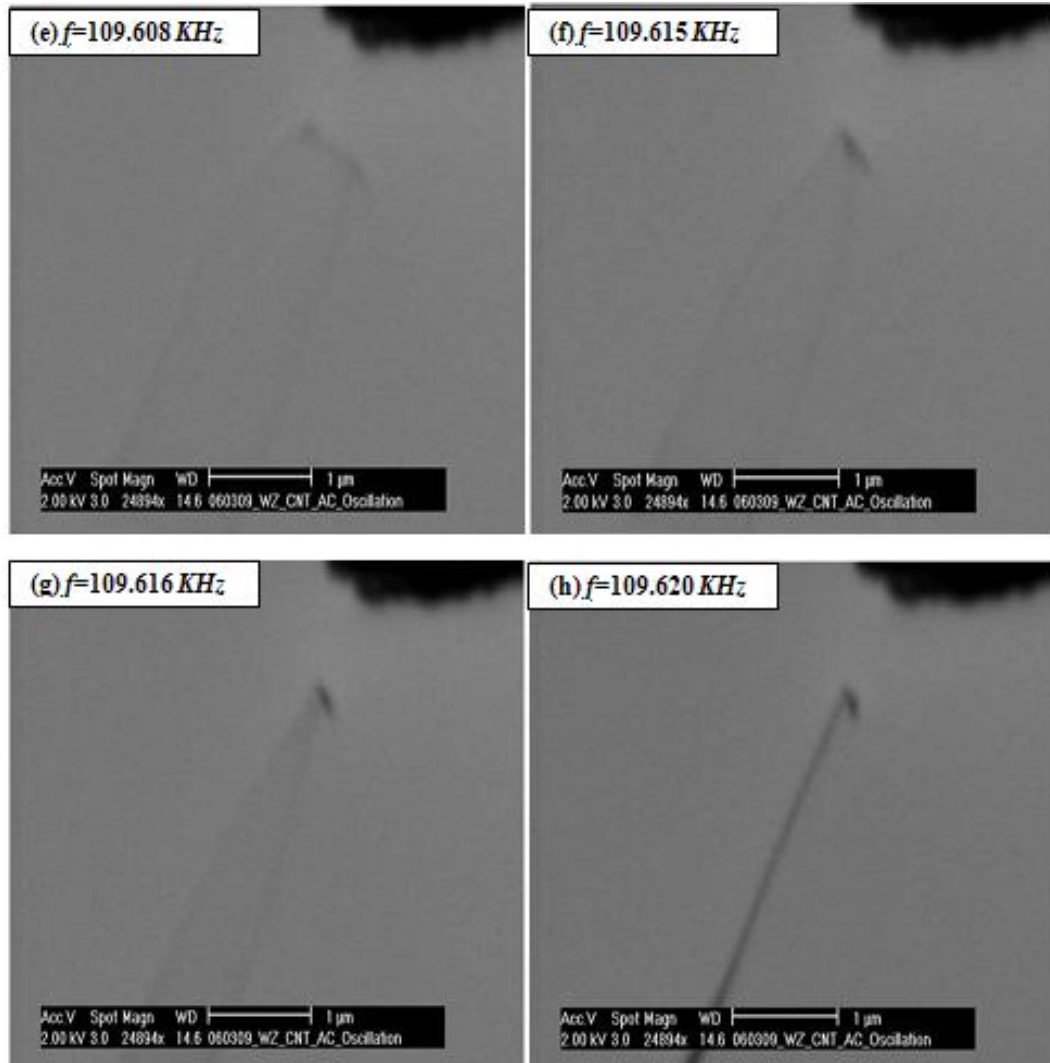
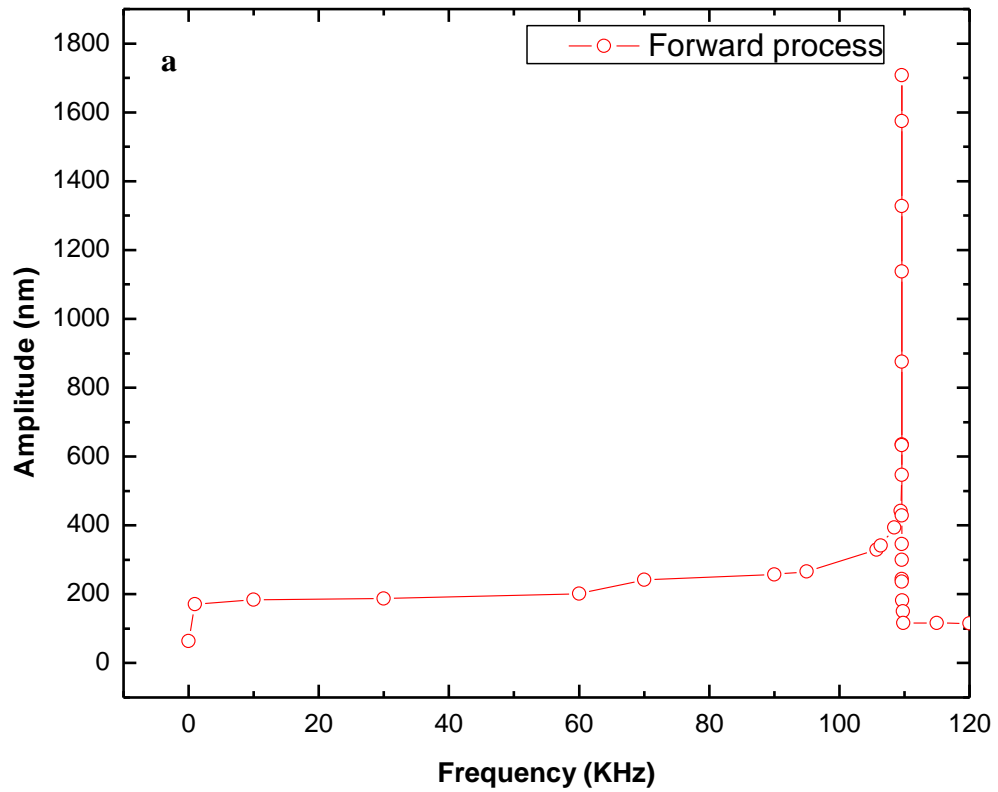


Fig 4. 10 Eight selected frequencies out of the acquired data points along the forward process, which starts from (a) to (h), exhibit the first order resonance of this CNT system. Fundamental resonance frequency is shown in (d) as 109.606 KHz.

Oscillation of CNT cantilever versus frequency (forward process)



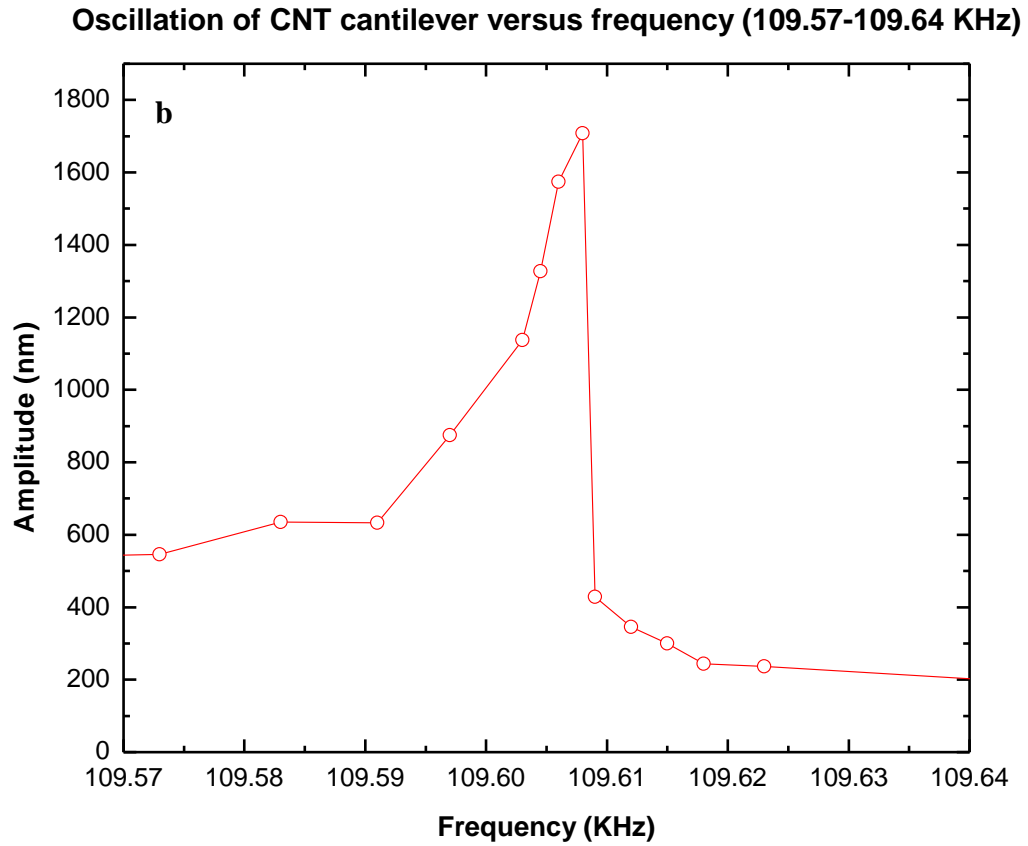


Fig 4. 11 The amplitude-frequency curve of the CNT resonator acquired according to the data points along the forward process. This fundamental resonance is a typical Lorentzian shape centered at $f=109.606$ KHz and the quality factor Q is 9743 for this nanotube resonator. Errors arise from both the digital resolution of the CRT screen for imaging acquisition and the measurement directly on these acquired images. In the following parts of this thesis, this criterion for determining the errors in measurement holds for processing of all the acquired images from SEM.

4.4.1.2 Backward process and sub-resonance peaks observed

When frequencies are further increased by even a small addition (a few kilohertz) after the first resonance peak, which is the natural resonance of the CNT system observed, the amplitude of oscillation drops dramatically. No more resonance peaks are observed with increasing the frequency further and hence the actuating frequency is decreased backwards. Surprisingly, not any resonance peak even at the previous resonant frequency can be observed again and the oscillation behavior of this CNT resonator seems to be irreversible.

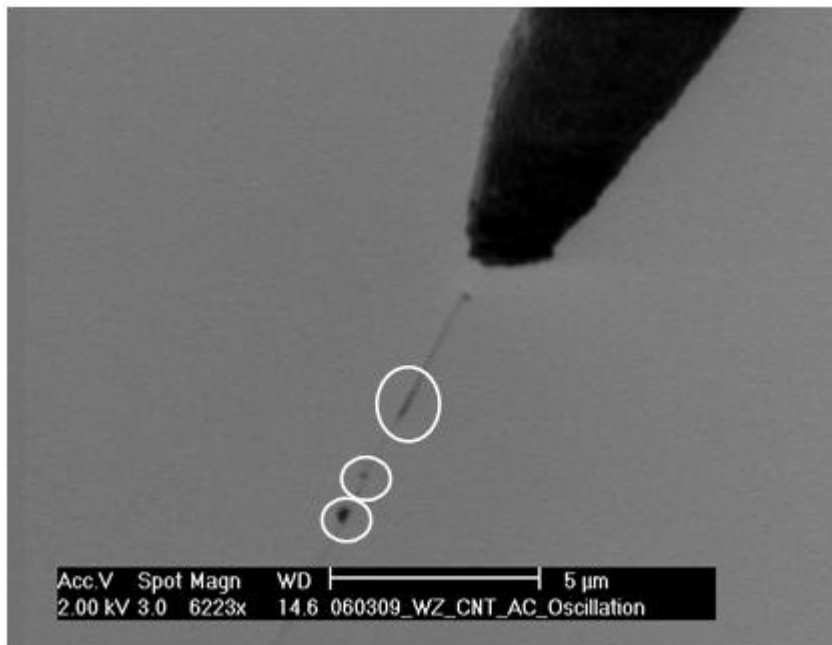


Fig 4. 12 Augmentation of diameter at some sites along the nanotube is observed as indicated by the circled black bulky parts, which is attributed to the EBID of amorphous carbon onto the CNT.

Meanwhile, augmentation of diameter at some sites along the nanotube is observed as indicated by circles in Fig 4.12. According to previous discussions, these black bulky parts are deposition of amorphous carbon layer caused by EBID of hydrocarbon

existing gas inside the SEM chamber. This CNT resonator might have been “disabled” so that it could oscillate at all or some changes in properties of this CNT resonator system cause the shift of the resonant frequency of this CNT resonator.

To verify whether this CNT resonator can still oscillate, the actuating frequency is maintained at a value of 109.202 *KHz* which is around the previous resonant frequency while the amplitude of dc bias is varied. The corresponding amplitude-dc bias curve is obtained as shown in Fig 4.13.

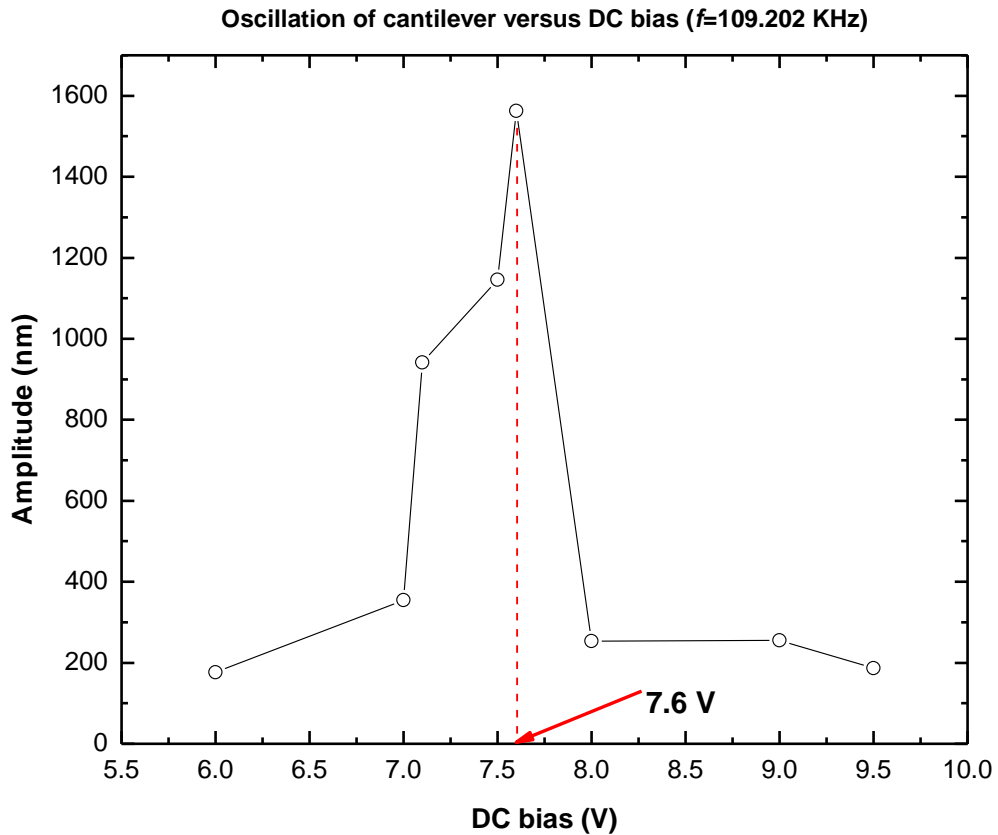


Fig 4. 13 The amplitude of oscillation-dc bias curve obtained for $f=109.202$ *KHz*, with dc bias from 5 V to 9.5 V. Amplitude peaks when dc bias is 7.6 V.

With actuating frequency adjusted around the previous resonant value, the amplitude of oscillation of this CNT peaks when dc bias is 7.6 V, rather than the previous 5 V. This implies that this CNT resonator still survives after EBID contamination while the properties of this CNT system have definitely been altered.

Since this CNT can still oscillate, the dc bias is set back to 5 V and the frequency continues to decrease backwards. When frequency is decreased to 108.680 KHz, a second resonance peak is observed. From Fig 4.14 which compares the resonance amplitudes of both the resonance at 108.680 KHz and 109.606 KHz, darker and thicker structure appears when $f=108.680$ KHz while no obvious discrepancies at first glance can be distinguished between the amplitudes for both occasions.

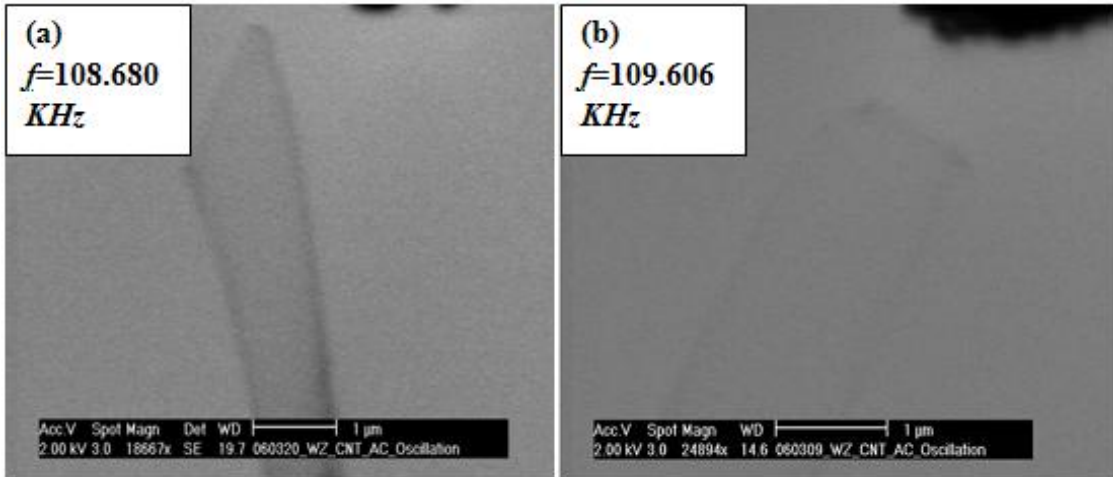


Fig 4. 14 Comparison between the resonance amplitudes for $f=109.606$ KHz in forward process and $f=108.680$ KHz in backward process. Darker and thicker structure appearing in (a) indicates EBID of carbonaceous substances.

After measurement, the amplitude-frequency curve depicting Fig 4.14 is shown below in Fig 4.15a. In Fig 4.15a, the widening of the resonance peak can be observed in the resonance in backward process compared to the one in forward process. This indicates

the decrease in quality factor and hence the deterioration of “quality” of this CNT system. Besides, the amplitude for resonance peak in backward process is also a bit smaller than the one for natural resonance peak in forward process. This fact also indicates that this CNT cantilever has been degraded along the whole process suffered.

When frequencies are further decreased, more sub-resonance peaks are observed and the corresponding amplitude-frequency curves are obtained as shown in Fig 4.15b and c.

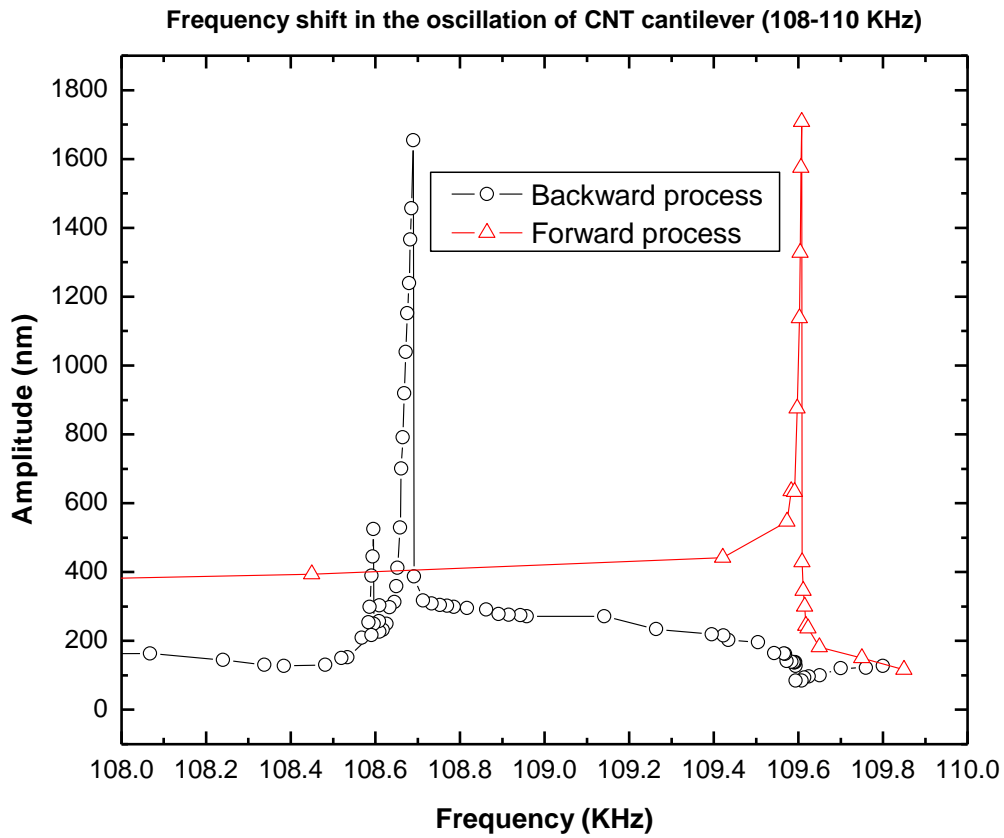
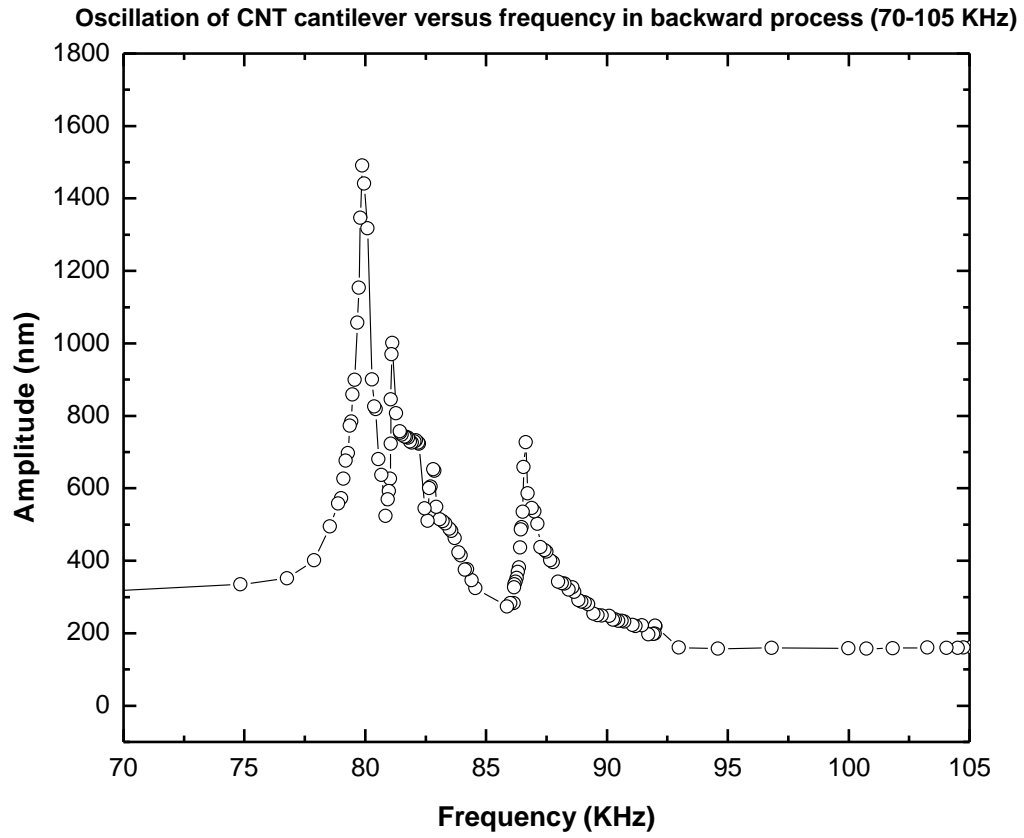
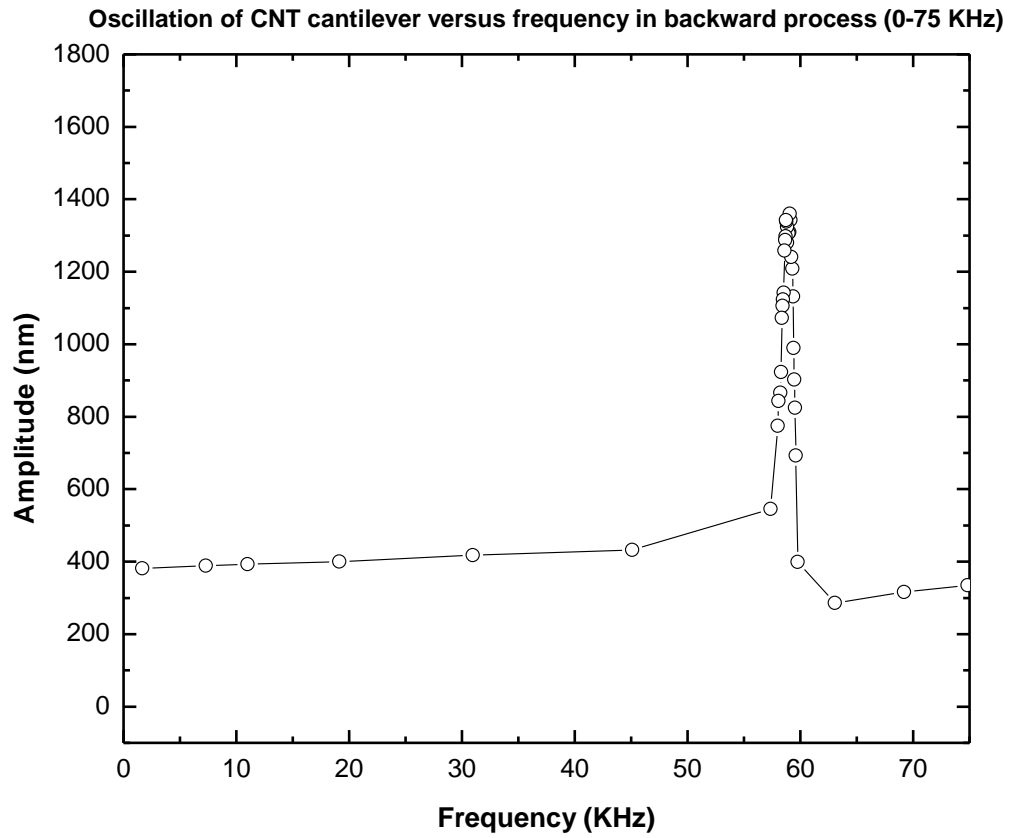


Fig 4. 15 Amplitude-frequency curves observed for forward and backward processes. (a) Amplitude-frequency curve comparing the natural resonance peak in the forward process and the first resonance peak observed in the backward process . Widening of the resonance peak in backward process indicates the decrease of quality factor of the CNT cantilever compared to resonance peak in forward process.



(b) With frequency further decreased, the second main resonance peak in the backward process is centered around 79.880 KHz.



(c) The third main resonance peak in the backward process is centered around 59.073 KHz.

4.4.1.3 Integrated mapping of electrically induced mechanical resonance

To better investigate and understand the behavior of this CNT resonator in both the forward and backward processes, the full mapping of electrically induced mechanical resonance is achieved by integrating Fig 4.15a, b and c as shown in Fig 4.16.

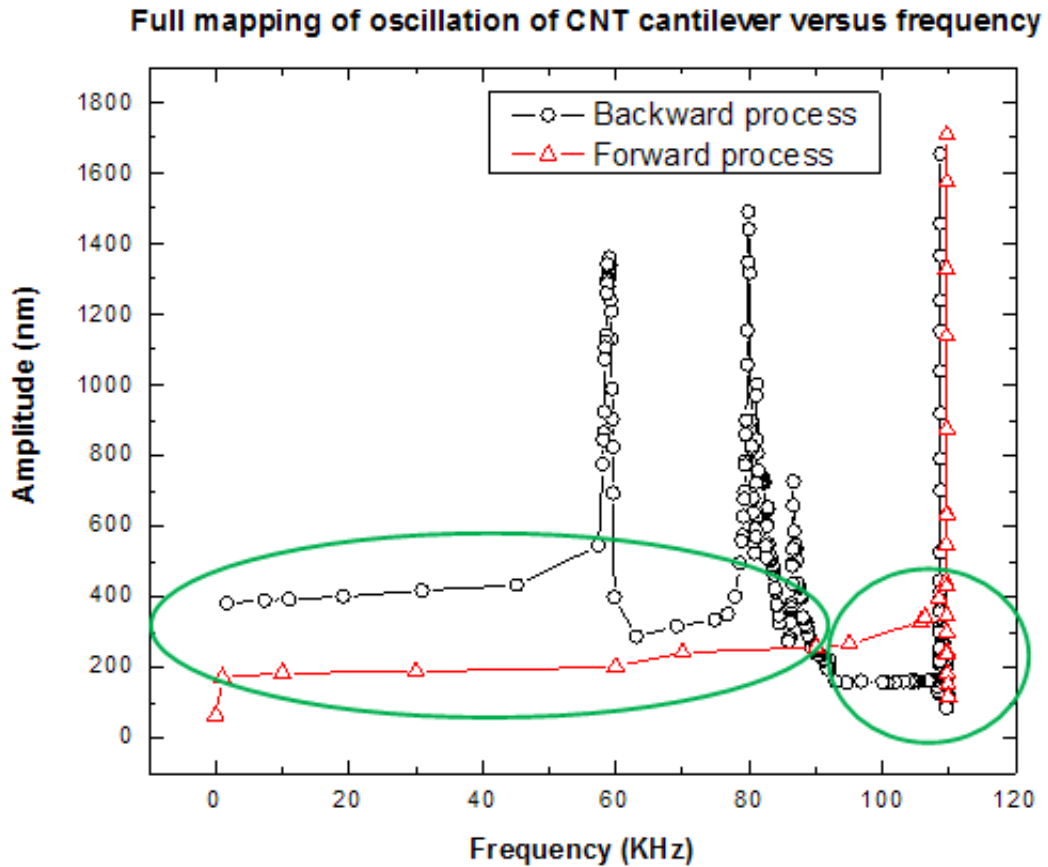


Fig 4. 16 Integrated mapping of electrically induced mechanical resonance. Peak 1 (red), 2, 3 and 4 (black) are observed successively.

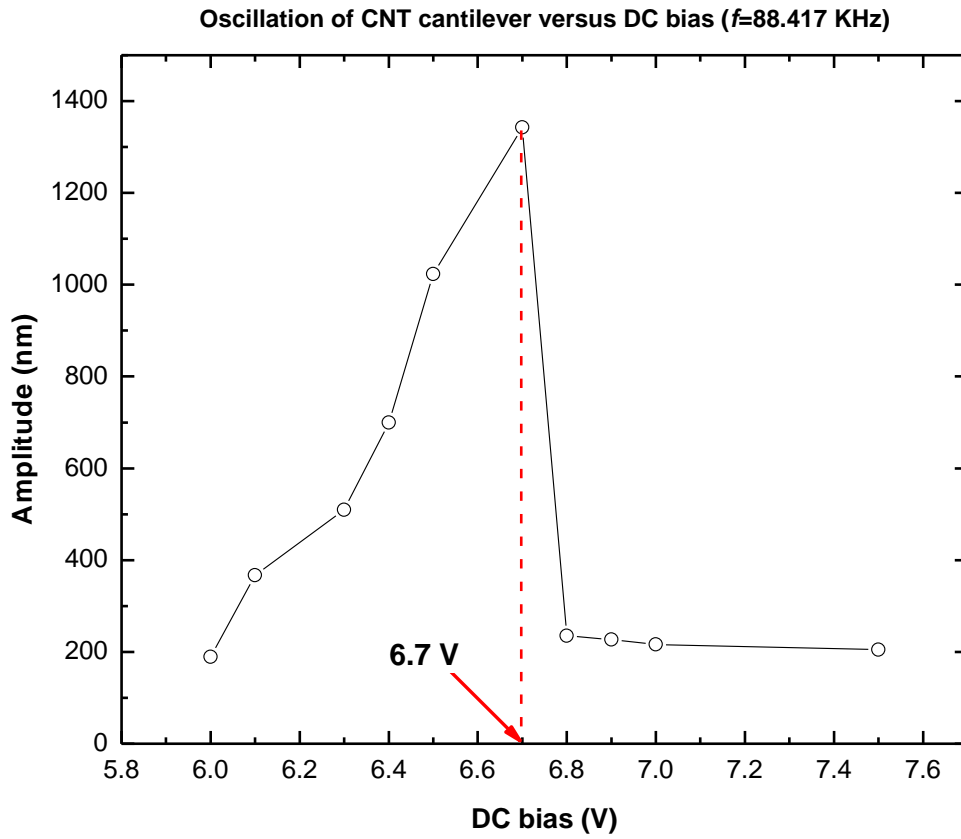
Interesting and significant information can be observed and derived from Fig 4.16. First of all, with the progressing of this experiment, the amplitude value of resonance peak decreases monotonously from peak 1 to peak 4 with the decrease of the actuating

frequency. Secondly, the width of resonance peak increases monotonously from peak 1 to peak 4 with the decrease of the actuating frequency. Thirdly, as indicated by the green circles in Fig 4.16, within the region between peak 1 and peak 3, the amplitude values along the forward process curve are always larger than the amplitude values of corresponding frequencies along the backward process curve, except within the confined region near the vicinity of peak 2. However, within the region from adjacency of peak 3 to the origin point, all the amplitude values on the backward process curve are larger than the corresponding values on the forward process curve. Finally, when frequency is adjusted back to zero again, the amplitude of the oscillation or the diameter of this CNT has been dramatically aggrandized compared to the initial value before this experiment started. The above observations will be investigated and analyzed in details in Chapter 5.

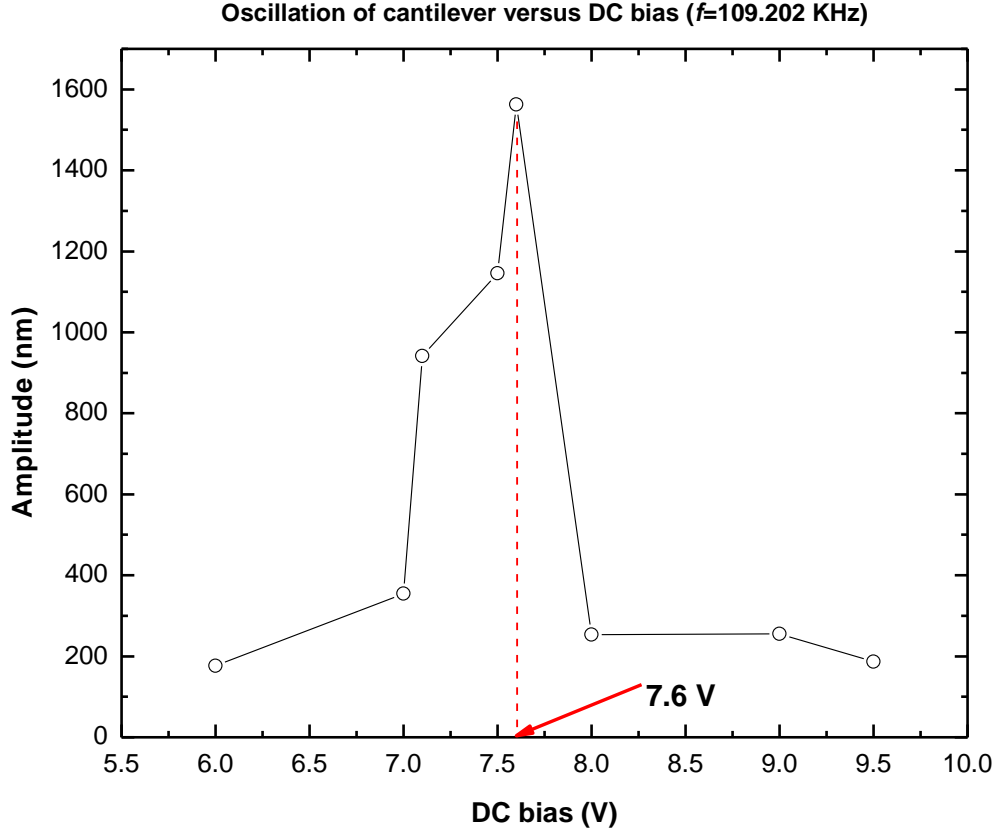
4.4.1.4 Effect of dc bias on oscillation

The fact that dc bias also affects the oscillation of the CNT resonator, specifically, enhances the oscillation at some specific values has been demonstrated in previous sections of this chapter. To verify the enhancement of resonance induced by dc bias, control experiments varying the dc bias applied at some selected frequencies have been conducted. The selected frequencies are 88.417 *KHz* and 109.202 *KHz*, at which no obvious oscillations are observed, which can also be seen from Fig 4.16. The corresponding amplitude-dc bias curves are obtained as shown in Fig 4.17.

In Fig 4.17a where $f=88.417\text{ KHz}$, the resonance peaks when dc bias is 6.7 V while in Fig 4.17b where $f=105.202\text{ KHz}$, the resonance peaked when dc bias is 7.6 V ; both are not the initially set value of 5 V . Further discussions will also be provided in Chapter 5.



(a)



(b)

Fig 4. 17 Effect of dc bias on oscillation of CNT system (a) $f=88.417$ KHz, resonance peaks when dc bias is 6.7 V. (b) $f=109.202$ KHz, resonance peaked when dc bias is 7.6 V.

4.4.2 Observation and characterization of samples in TEM

The measurements of CNT cantilever under investigation obtained from SEM characterization can only provide rough estimation and reveal nothing further about the nanostructures of the CNT. It is usually difficult to analyze CNTs using SEM due to insufficient resolution and lack of detailed information regarding the nanostructures. High electron beam energy around 10 kV or above is needed for better resolution.

Nevertheless high beam energies can cause worse hydrocarbon contamination onto the CNTs investigated, therefore rendering the CNTs appear thicker and darker than the original ones. The contamination is even worse when samples are viewed at high magnifications above 20,000 times in SEM. Moreover, images acquired in SEM will give an inaccurate measurement of important structural parameters of CNTs such as the inner and outer diameters, which are of crucial importance for the subsequent analysis.

TEM is a powerful tool for characterizing the atomic-scale structures of solid state materials. A modern TEM is so versatile that it can provide a real-space resolution better than 0.2 *nm* and also give a quantitative chemical and electronic analysis from a region as small as 1 *nm* [66] . It is feasible to receive a full structure characterization from TEM. In order to study the properties and structure of individual CNT and understand the property-structure relationship, TEM characterization is indispensable in this project and subsequent analysis.

4.4.2.1 Preparation procedures

In order for TEM characterization to be carried out, very thin tungsten wires with diameters around 100 μm are used as substrates for CNTs growth. The tungsten tips with CVD grown CNTs are then mounted onto a copper TEM sample holder using silver paint and inspected in SEM before subsequent TEM observation. Quick inspection in SEM is to ensure that the tungsten wire mounted possesses enough CNTs as candidates for characterization in TEM as it usually takes a long period to finish pumping down in TEM.

One challenge in TEM sample preparation is mounting the tungsten tip onto the copper TEM sample holder. The holder is extremely small and the tungsten tip has to be trimmed short in order to fit the small geometry of the holder. This trimming process also requires estimation of the location where CNTs are dense; hence extra precaution is needed not to cut away the wrong section. The brittleness of the tungsten tip after growing CNTs is also problematic.

4.4.2.2 Results in TEM

The growth parameters for MWNTs investigated previously as CNT-cantilevers in this chapter are shown in Table 4.1, which are determined and adopted according to the discussion conducted in Chapter 3.

Table 4. 1 Growth parameters of MWNT for CNT-cantilever

Substrate	Growth time	Catalyst	Temperature	Pressure	C ₂ H ₂ flow rate	NH ₃ flow rate
Tungsten	5 minutes	Iron	780°C	1.6mBar	5.5 sccm	60 sccm

The observation and characterization results in TEM are shown in Fig 4.18. These TEM images confirm that CNT structures are formed because the inner part of these structures is hollow and there are visually distinguishable boundaries indicating the number of walls (graphene shells) of these CNTs.

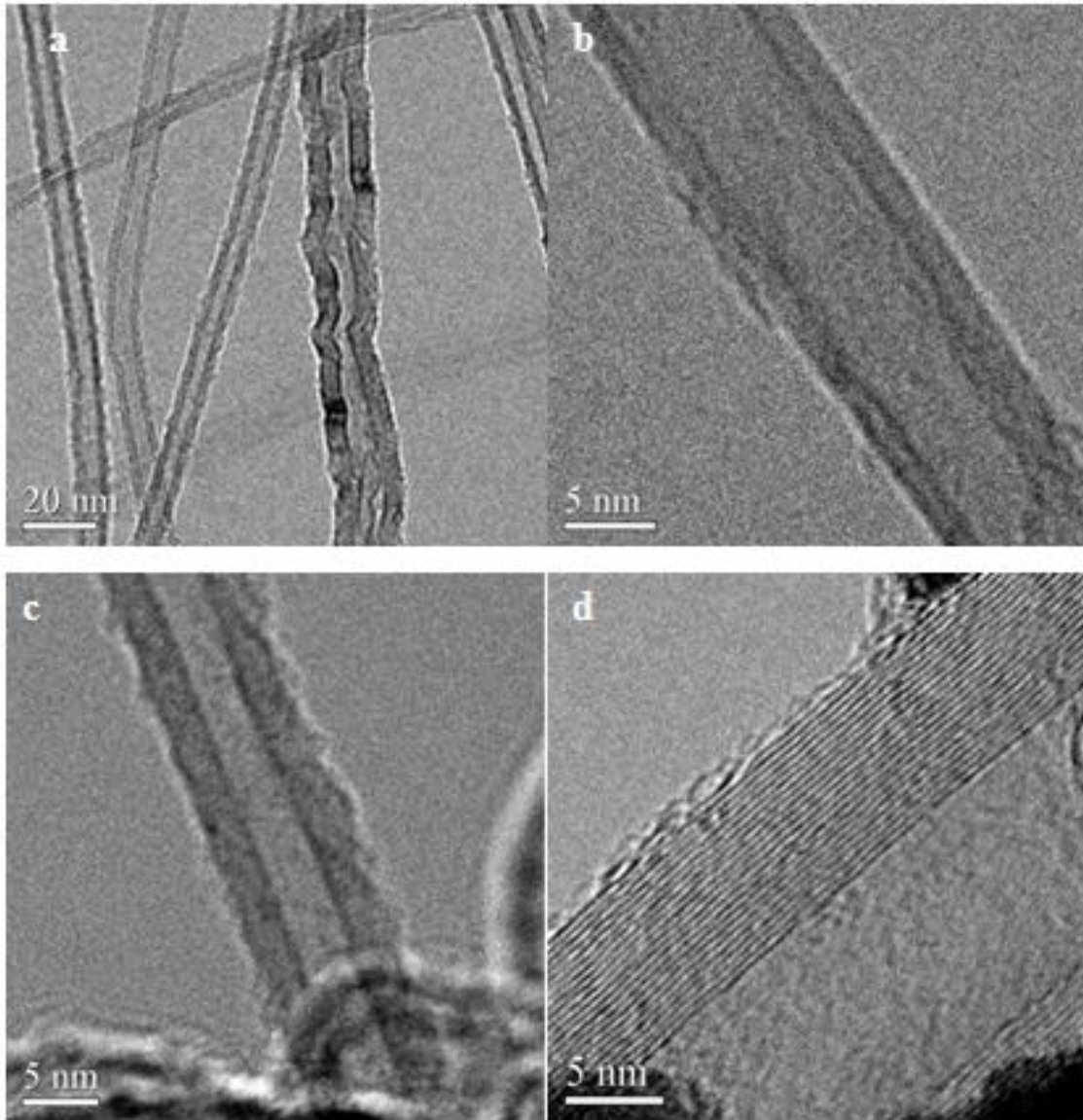


Fig 4. 18 TEM images of catalytic CVD grown MWNTs. (a) CNTs with average diameters of 10nm. (b) (c) CNTs with diameter about 10nm (d) MWNT with outer diameter around 25nm and 22 graphene shells (walls).

These TEM images exhibit CNTs with diameters around 10 to 20 *nm*. As compared to images of these CNTs acquired in SEM, these diameter values are much smaller and

more accurate. Most of the CNTs suffer the carbon contaminations found on the outer shell of CNTs as clearly observed in Fig 4.18b and c. Fig 4.18d indicates a MWNT clearly and the number of the walls is counted as 22. This particular CNT is investigated as the cantilever in previous sections and further detailed analysis of this CNT-cantilever will be conducted in Chapter 5.

4.5 Summary

Free standing cantilevered CNT resonator is fabricated with the aid of nanomanipulator and SEM. Electrical actuation and *in situ* harmonic detection of electrically induced mechanical resonance of single MWNT cantilever is conducted in this chapter. *In situ* investigation of performance of cantilevered CNT resonator prototype under DC and AC bias in SEM is carried out. Continuous redshift in resonant frequency and broadening of resonance peak of this NEMS resonator under electron beam in SEM is observed. The structural parameters of the CNT under investigation are attained in TEM. The experimental results achieved in this chapter pave the way for further analysis of performance of the CNT resonator and evaluation of the feasibility of CNT resonator as ultrasensitive mass sensor in Chapter 5.

CHAPTER 5

ANALYSIS of CARBON NANOTUBE RESONATOR PERFORMANCE

5.1 Introduction

In this chapter a quantitative model for describing the specific actuation method and theoretical output signal of the CNT resonator motion introduced in Chapter 4 is presented first (section 5.2). Pragmatic considerations based on this theoretical model help determine and choose these methods rather than others.

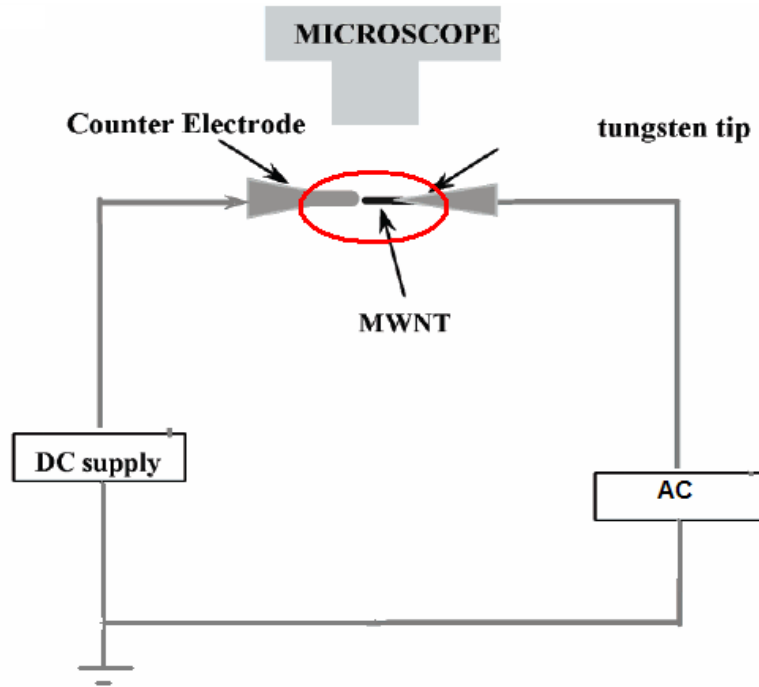
Carbon nanotube possesses the hollow structure and hence it should be natural using a hollow tube model to describe the CNT resonator. An analysis of the measurement results attained in Chapter 4 of the CNT resonator device is provided afterwards. First, important parameters such as bending modulus which describe and characterize CNT resonator and its performances is calculated using the hollow tube model and compared with both the theoretically values predicted and experimental results reported (section 5.3). Possible mechanisms and reasons for discrepancies between the experimentally calculated and theoretical values are then discussed further. An interesting and insightful phenomenon observed during the experiment is the continuous redshift in resonant frequency and broadening of resonance peak of this NEMS resonator. This variation is attributed to the consecutive deposition of carbonaceous substances onto the resonator. Discussion of the relationship between carbon contamination, or the loaded mass, and resonant frequency shift using classical theorem has also been conducted.

Based on the discussions in section 5.3, the capability and feasibility of CNT resonator acting as ultrasensitive mass sensor is examined and discussed in details in section 5.4.

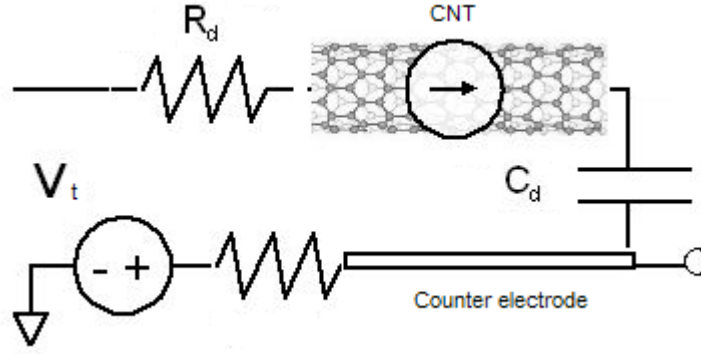
An evaluation and appraisal of the performance of CNT resonator under investigation and the feasibility of catalytic CVD grown CNT as building blocks for NEMS as well as potential applications are then concluded and proposed at the end of this chapter (section 5.5).

5.2 Model for actuation and theoretical values of output signal

The motion of CNT is actuated through the electrostatic interaction via the configurations described in Chapter 4 which recurs and has been modified into equivalent circuit as shown in Fig 5.1.



(a)



(b)

Fig 5. 1 Schematic of experimental setup and equivalent circuit for actuation of CNT motion (a) Experimental setup for actuation as shown in Chapter 4 (b) In this equivalent circuit, the CNT is not aligned parallel to the counter electrode as depicted here; it is still aligned axially with the counter electrode.

A dc voltage V_d induces the additional charge on the CNT tip given by $q = C_d V_d$, where C_d is the capacitance between the tip of CNT and the counter electrode. The attraction between charge q and its opposite charge $-q$ on the counter electrode causes an electrostatic force outwards along the CNT. If $C'_d = dC_d/dz$ is the derivative of the gate capacitance with respect to the distance between the tip of the tube and the counter electrode, the total electrostatic force on the tube is

$$F_{el} = \frac{1}{2} C'_d V_{dc}^2 \quad (5.1)$$

If this dc voltage is modulated by some driving frequency ω ,

$$V_t = V_{dc} + \underbrace{\tilde{V}_{ac} \cos \omega t}_{V_{ac}} \quad (5.2)$$

The total electrostatic force on the tube is

$$F_{el} = \frac{1}{2} C'_d V_{dc} (V_{dc} + 2V_{ac}) \quad (5.3)$$

where the term proportional to V_{ac}^2 has been neglected for the purpose of fundamental demonstration of nanotube oscillator prototype.

Here F_{el} has two parts: the dc term controlled by the dc voltage V_{dc} and the ac term produced by the ac component of the actuation bias V_{ac} .

$$F_{el}^{dc} = \frac{1}{2} C'_d V_{dc}^2 \quad (5.4)$$

$$\tilde{F}_{el} \approx C'_d V_{dc} V_{ac} \quad (5.5)$$

The dc term is used to control the resonator tension, and the ac term sets the resonator into motion. As the driving frequency ω approaches the resonance frequency ω_0 of the CNT resonator, the displacements of the tip of the resonator become larger and larger.

Although directly visual observation to determine the motion of NEMS resonator is utilized in the experiments, a fully electrically controlled detection method is highly advantageous for any possible future applications and research such as detecting the motion of the nanotube on resonance. A model for predicting and evaluating the possible output signals produced by the motion of the NEMS resonator is provided as follows first.

As is extracted from Fig 5.1b, the output signal is contributed mostly by the induced capacitive current. To calculate and evaluate this current, the circuit shown in Fig 5.1b is further simplified mathematically as seen in Fig 5.2.

The hemline of the triangle in Fig 5.2 identifies the trace of tip of the investigated nanotube during oscillation. Some approximations have been made here since this trace in reality is an arc rather than the straight line shown in Fig 5.2. However, as shown in Fig 4.10, the maximum amplitude for oscillation is only around $1 \mu m$ while the length of the nanotube under investigation is around $34 \mu m$, which indicates that the central angle corresponding to this arc is roughly 1.69° . Therefore, for convenience of calculation and proof-of-concept, this arc is replaced with a straight line.

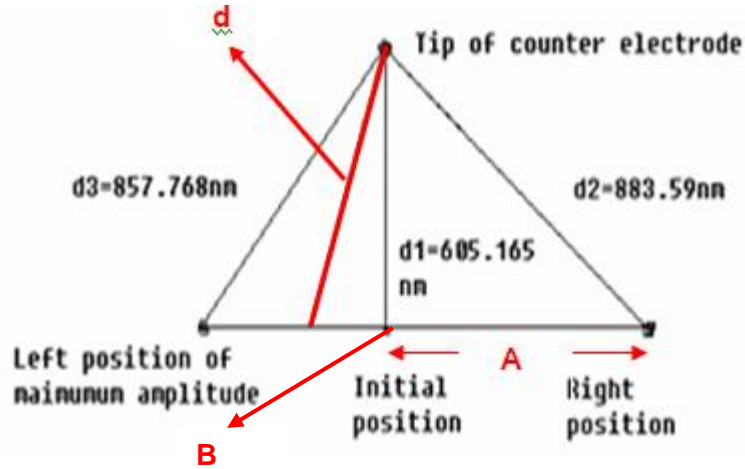


Fig 5. 2 Schematic of mathematical model for calculation of potential electrically output signal

Point B is the initial position of the nanotube tip. The displacement of each point on the trace from the initial position can be expressed as

$$x = A \sin \omega t \quad (5.6)$$

where $A = \sqrt{\left(\frac{d_2 + d_3}{2}\right)^2 - d_1^2}$ is the modified magnitude of the motion of nanotube tip.

$\omega = 2\pi f$ represents the angular velocity of the oscillation when nanotube oscillates at

the driving frequency while f is the frequency of ac bias in the actuation supply. The distance between the tips of nanotube and the counter electrode is thus expressed as

$$d = \sqrt{d_1^2 + (A \sin \omega t)^2} \quad (5.7)$$

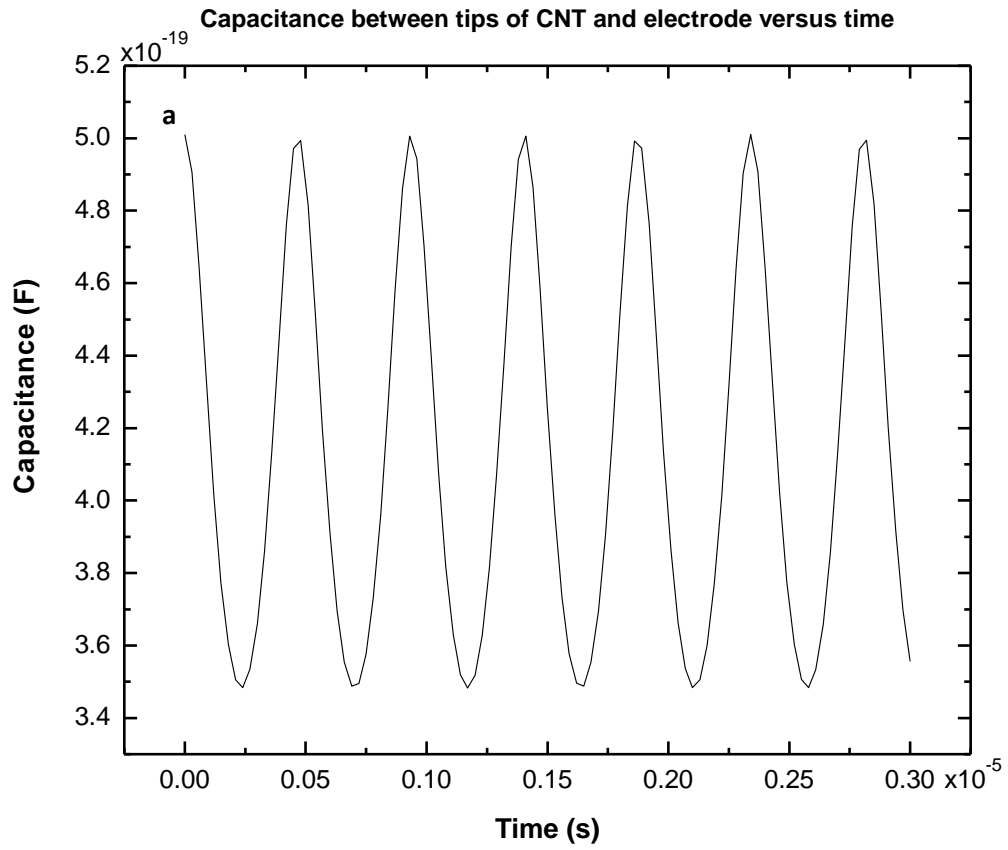
From the definition of capacitance $C = \frac{\epsilon S}{d}$, the capacitance C_d between the tips of nanotube and the counter electrode is obtained as

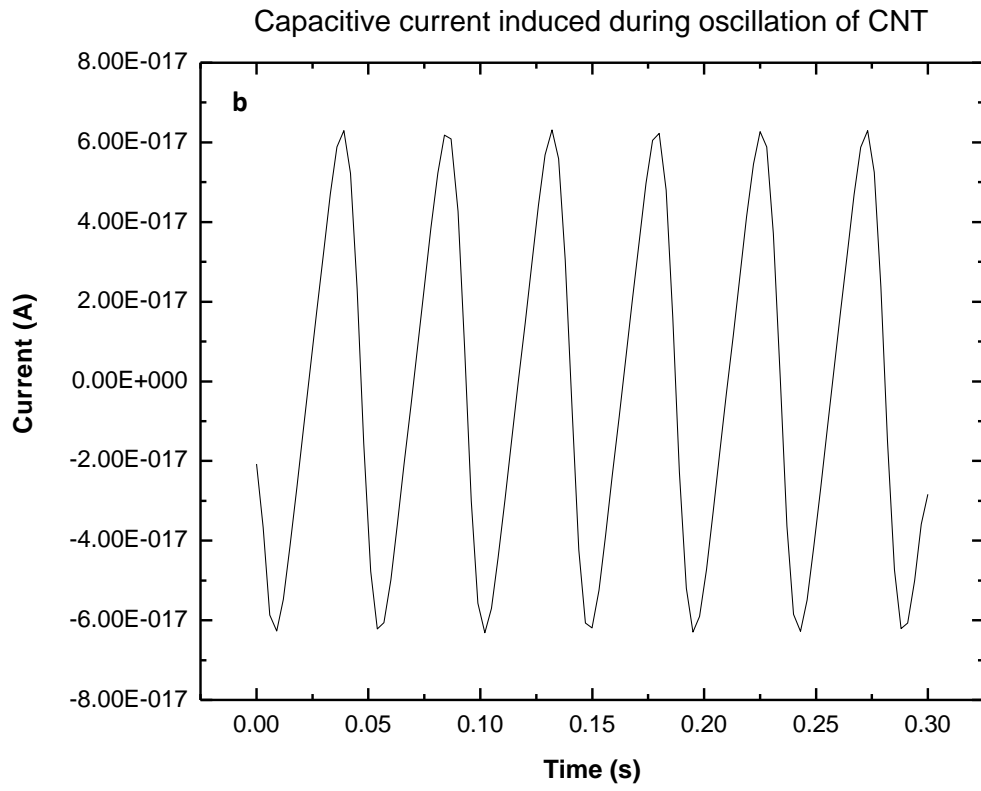
$$C_d = \frac{\epsilon S}{d} = \frac{\epsilon S}{\sqrt{d_1^2 + (A \sin \omega t)^2}} \quad (5.8)$$

Therefore the induced capacitive current is obtained and expressed as

$$I = \frac{dQ}{dt} = \frac{1}{V} \frac{dC_d}{dt} = \frac{1}{V} \frac{d \frac{\epsilon S}{\sqrt{d_1^2 + (A \sin \omega t)^2}}}{dt} \quad (5.9)$$

where Q represents the induced charge on the tip of nanotube resonator.





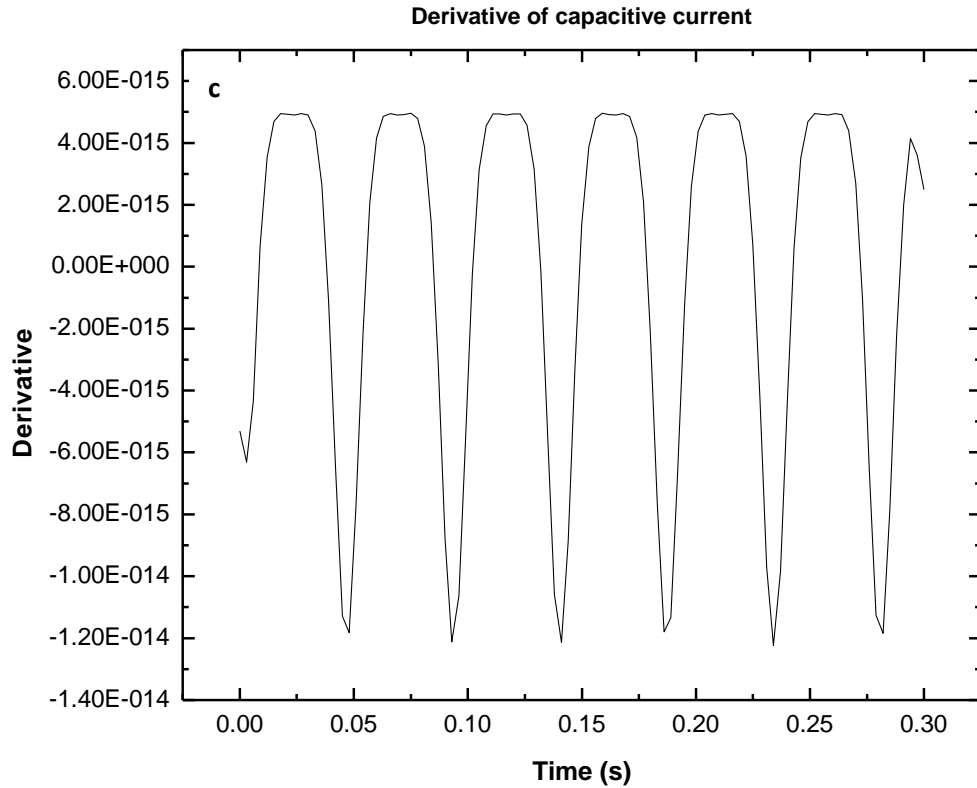


Fig 5. 3 Calculated capacitance between tips of CNT and counter electrode and output signal according to models in Fig 5.1 and Fig 5.2 at resonance of CNT resonator (a) Capacitance C_d (b) Capacitive current induced by changes in C_d between tips of CNT and counter electrode (c) First order derivative of capacitive current. f is 109.606 KHz.

Focus is placed on the resonance for the calculation, where the actuating frequency f is 109.606 KHz. Change of capacitance between tips of nanotube and counter electrode and the output capacitive current as well as the first order derivative of capacitive current in time domains are obtained as shown in Fig 5.3.

The capacitance between tips of nanotube and counter electrode varies in the quasi-sinusoidal form versus time while the induced capacitive current exhibits obliquely distorted sinusoidal characteristic. Insightful information obtained from Fig 5. 3 are that the extremely small levels of both the capacitance and the induced current. The

calculated capacitance is below $10^{-18}F$, which renders the capacitive detection complicated by the presence of parasitic capacitances that are several orders of magnitude larger. This challenge is usually overcome by the use of balanced bridge techniques or by placing an amplifier, such as, for example, a single electron transistor [9] , in close proximity to the resonator. However, this will inextricably result in complicity in both fabrication and characterization. Besides, the low-temperature requirement for performing the above amplification limits its utilization in the experiment.

The induced capacitive current is also inevitably small and ensnared within the sub-picoampere region, where noise becomes a real nightmare. The internal impedances of the measuring instrument or circuit become extremely critical to ensure an accurate measurement of such a weak current. Noises in acoustic, thermal or even electrochemical forms can contribute great undesirable errors and fluctuations in measurement.

To avoid the inaccuracies in measurement and complexities in experimental setup as well as to investigate the feasibility of CNT as NEMS resonator with high sensitivity, directly visual observation in SEM and TEM is adopted as demonstrated in Chapter 4 instead.

5.3 Characterizing resonance of the CNT resonator

In the linear regime of operation, when the displacement of the vibrating element is small, mechanical structure can be approximated as a simple harmonic oscillator. It has been shown by molecular dynamics simulations [67] , [68] that such calculations

continue to be valid as the sizes of the structures shrink down to several tens of lattice constants in cross section. Therefore, despite the extremely small dimensions and ultra-high aspect ratio of CNT, the classical continuum mechanics method has been applied to analyze the dynamic responses of CNT resonator to provide with elementary theoretical analysis and predication. Above the critical displacement of the mechanical structure various types of nonlinearities in the restoring force of the system become increasingly important. These nonlinearities can be caused by the elongation of the beam, imperfect clamping, or some kind of force gradient present in the system. This behavior of mechanical resonators is very useful for certain applications, such as memory [69] and signal processing [70]. These nonlinear behaviors known as Duffing oscillator will not be covered in this thesis.

Based on the Euler-Bernoulli beam model [71], it is well known that the equation of motion of a free vibration beam in the limit of small amplitude (linear region) is governed by the fourth-order wave equation

$$EI \frac{\partial^4 y}{\partial x^4} + \rho A \frac{\partial^2 y}{\partial t^2} = 0 \quad (5.10)$$

where E is the bending modulus, I is the moment of inertia, A is the cross-sectional area, and ρ is the density of the beam material.

The natural mechanical resonant frequency is induced in a cantilevered CNT when the applied frequency approaches the resonant frequency. Theoretically, the resonant frequency depends on the nanotube outer diameter, inner diameter, length, density, and bending modulus of the nanotube [72] as expressed by

$$f_i = \frac{\beta_i^2}{8\pi} \frac{1}{L^2} \sqrt{\frac{(D_o^2 + D_i^2)E}{\rho}} \quad (5.11)$$

where $\beta_1 = 1.875$ for calculation of first harmonics of the cantilever.

From the SEM and TEM images of the CNT resonator investigated in this project as shown in Fig 5.4, length, inner diameter and outer diameter of this CNT resonator are measured as $34.37 \mu m$, 10.73 nm and 26.54 nm respectively. If the commonly recognized values [73] for bending modulus ($1.8TPa$) and density of MWNTs (1.35 g/cm^3) are adopted, the resonant frequency for this CNT resonator is obtained as $f = 123.779KHz$.

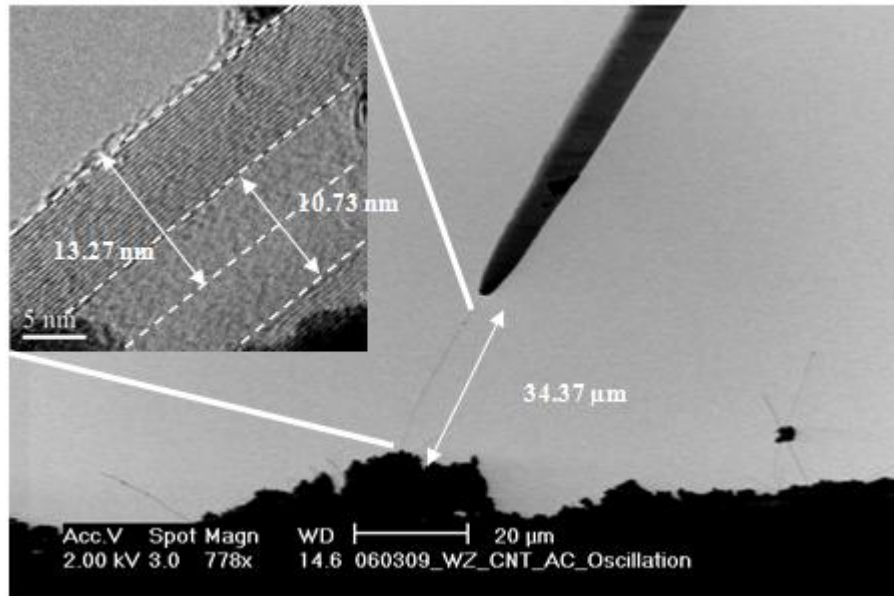


Fig 5. 4 TEM and SEM images indicating the structural parameters for CNT resonator. Inner and outer diameters of this CNT are measured as 10.73 nm and 26.54 nm from the inset TEM image. Length of this CNT is obtained as $34.37 \mu m$ from SEM image.

This calculated value tallies with the experimental result 109.606 KHz obtained in Chapter 4 quite well. However, this calculated value and the experimental result are

both much smaller than either conventionally predicated values which could reach as high as in the gigahertz range [74] or the reported experimental value around 700 *KHz* [75] . The main reason for these huge discrepancies lies mainly in the length of nanotube. In this experiment, the length of nanotube cantilever is 34.37 μm , which is quite a long tube, while the length in C.H.Ke's [74] theoretical analysis is smaller than 1 μm and the length in Nishio's experiment [75] is also around 1 μm only.

Moreover, the observed result is also smaller than the calculated value with an 11.4% deviation. This can be explained by the EBID deposition of carbonaceous substance onto the nanotube, which will also be investigated further in later sections where this deviation between the calculated first harmonics and the experimentally observed one will be reviewed. The defective structure of CNT suffering through CVD growth might also contribute to the smaller resonant frequency observed.

Similarly, the bending modulus for CNT resonator has also been extracted by replacing f_i with the experimental value 109.606 *KHz* in Equation 5.11. The resultant bending modulus is thus obtained as $E = 1.41TPa$. This calculated bending modulus value shows that the CNT obtained in this experiment is much stronger than steel, which averagely possesses a value of 200*GPa* for bending modulus, and even eclipses the diamond. The above experimentally extracted bending modulus value is also consistent with the reported experimental results [49] albeit a bit smaller than the previously used value (1.8*TPa*).

As the case stands and demonstrated above, determining the elastic properties, mainly the bending modulus, of CNTs has been one of the most hotly disputed areas of

nanotube study in recent years. On the whole, CNTs, particularly SWNTs, are stiffer than steel and are resistant to damage from physical forces. Pressing on the tip of the nanotube will cause it to bend without damaging tip or the whole CNT. When the force is removed, the tip of the nanotube will recover to its original state [66] . Quantifying these effects, however, is rather difficult and an exact numerical value of bending modulus could hardly be agreed upon.

The previous evidence would lead us to assume that the diameter and shape of the nanotube are the determining factors for its elastic modulus and the bending moduli of the MWNTs are measured as a function of their diameters (outer) [66] . A decrease in bending modulus as the increase of the tube diameter is attributed to the wrinkling effect of the wall of the nanotube during small bending. However, when working with different MWNTs, Forró *et al.* [76] noted that their modulus measurements of MWNTs in 1999 did not strongly depend on the diameter. Instead, they argued that the modulus of MWNTs correlates to the amount of disorder or defect in the structure of nanotube walls. From previous chapters of this thesis, a high density of defects have been found in CNTs produced by pyrolysis CVD process in the experiment, which are mainly induced by the introduction of pentagonal and heptagonal carbon-rings, while in theoretically ideal structure of CNTs only hexagonal carbon-rings exist. To understand the structure-properties relationship, the TEM results of CVD grown CNTs have been investigated and compared with those of the commercial CNTs.

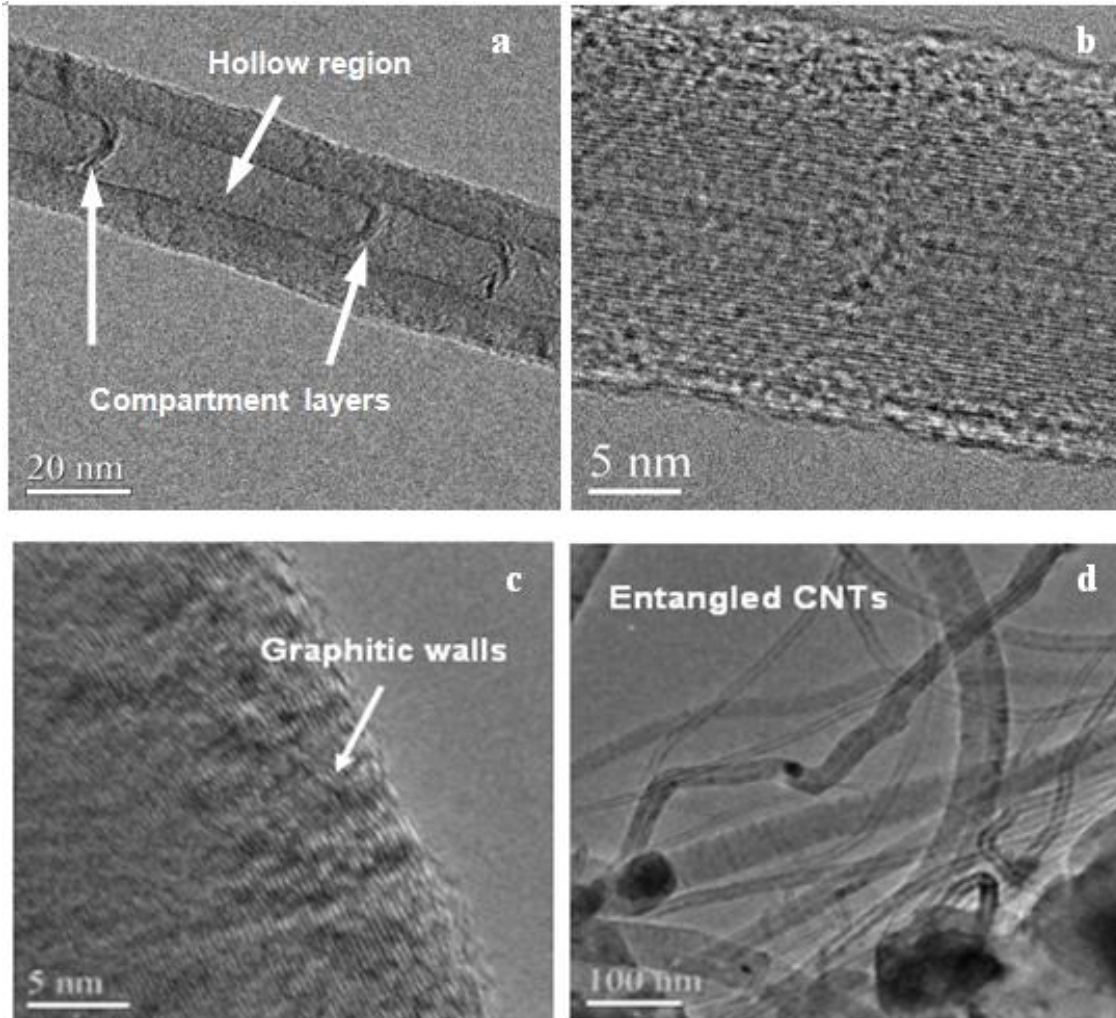


Fig 5. 5 Structures of CVD grown CNT and commercial arc-discharge CNT. (a) The compartment layers in the inner core of the CNT separate the hollow regions (b) Commercial arc-discharge grown CNT (c) Wavy graphitic walls (d) Entangled CNTs. (a), (c) and (d) are thermal CVD grown CNTs while (b) is the commercial arc-discharge CNT.

In Fig 5.5a bamboo-like structure in these CVD grown carbon nanotubes have also been observed, which is very different from those produced by arc-discharge (Fig 5.5b). The walls of CVD grown CNTs appear to be wavy (Fig 5.5c) which suggests they are not perfect graphitic networks but only possess short-range graphitic order. The defects on the graphitic walls induce bending of the carbon nanotube walls, which might cause the decrease of bending modulus and hence the worse elastical performance. These wavy

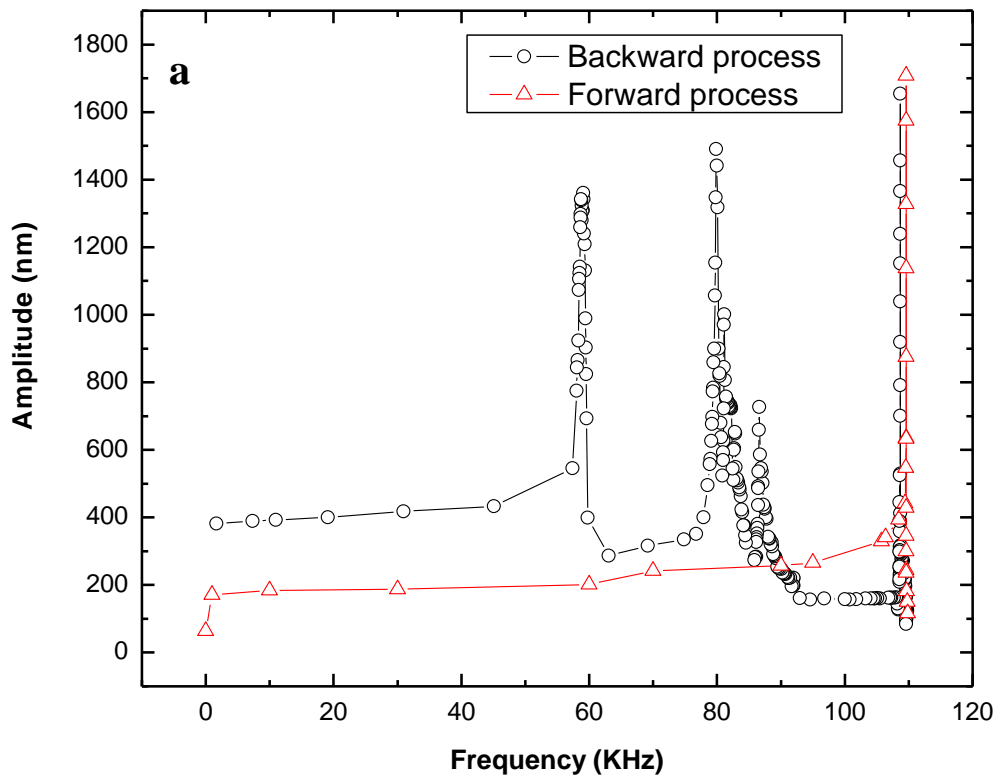
graphitic walls contain a high density of point defects because of the introduction of pentagons and/or heptagons as mentioned previously.

The geometrical shape makes significant contribution to the measured bending modulus, which is different from Young's modulus. However, with the decrease in nanotube diameter, the bending modulus approaches the Young's modulus. Young's modulus is another important quantity defined to characterize the interatomic interaction force [66] and is the double differentia of the bonding energy curve between the two atoms. This indicates that Young's modulus is an intrinsic property at the atomic level and is thus independent of the sample geometry. For the CNT resonator case investigated in the experiments, the bending of the CNT is determined not only by the intrinsic Young's modulus but also by the geometrical shape of the CNT, such as the wall thickness and tube diameter. The value extracted previously by *in-situ* SEM experiments is the bending modulus.

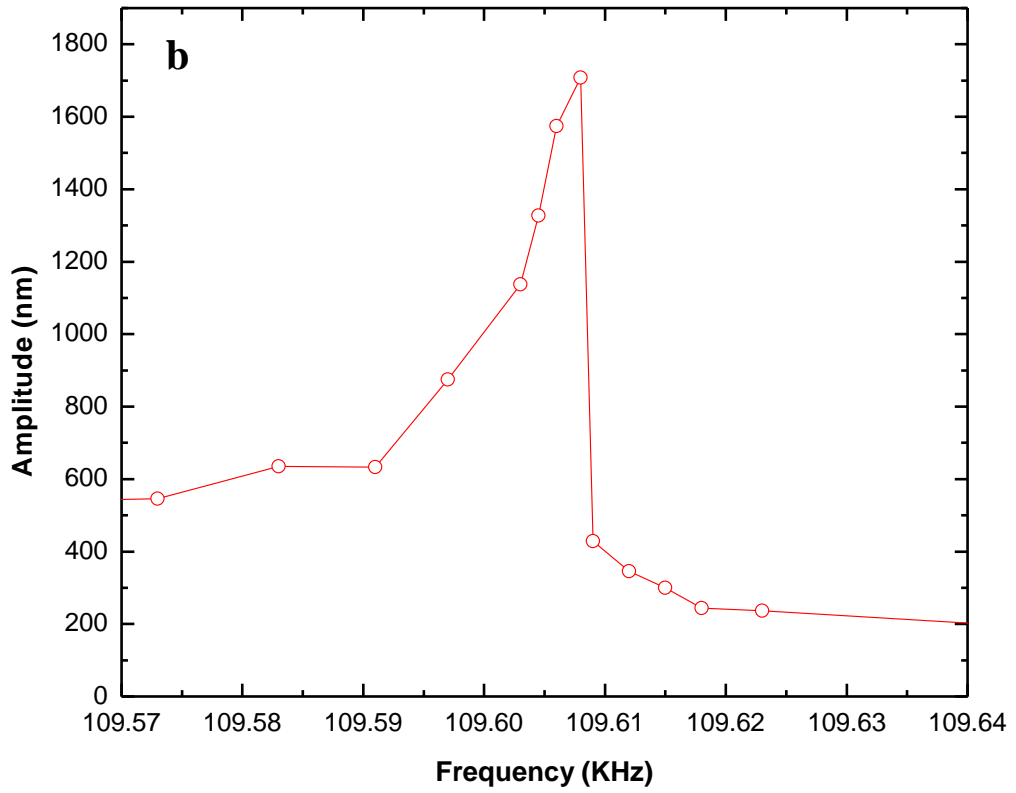
From the integrated mapping of electrically induced mechanical resonance of CNT resonator attained in Chapter 4 as shown in Fig 5.6, insightful information which could help describe and characterize the CNT resonator and its performances have been acquired. Fig 5.6a, which is the integrated mapping of resonance of CNT resonator during the experiment, illustrates an obvious trend of decline in the amplitude of resonance with a broadening of corresponding resonance peak, which is characterized by FWHM, full width at half maximum. Fig 5.6b, c, d and e represent the resonance peak 1, 2, 3 and 4 respectively. The variations in both amplitude and FWHM of the oscillation are attributed to the EBID of carbonaceous substance onto the nanotube. The electron beam used for imaging in SEM interacts with the CNT and even damages it

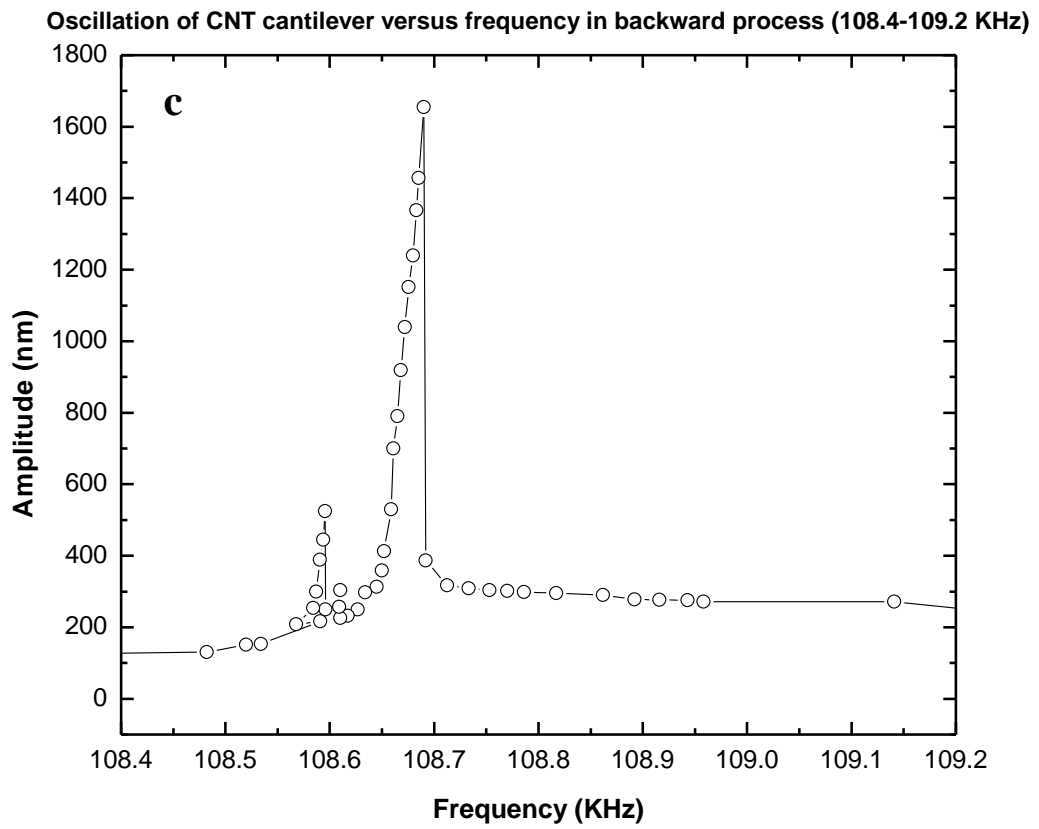
both structurally and electrically. Although the above facts are disadvantages of directly investigating and characterizing vibration of CNT resonator in SEM and TEM, this phenomenon does help us study and fathom some potential applications of CNT resonator such as ultra-sensitive mass sensors for sensing extremely small mass changes.

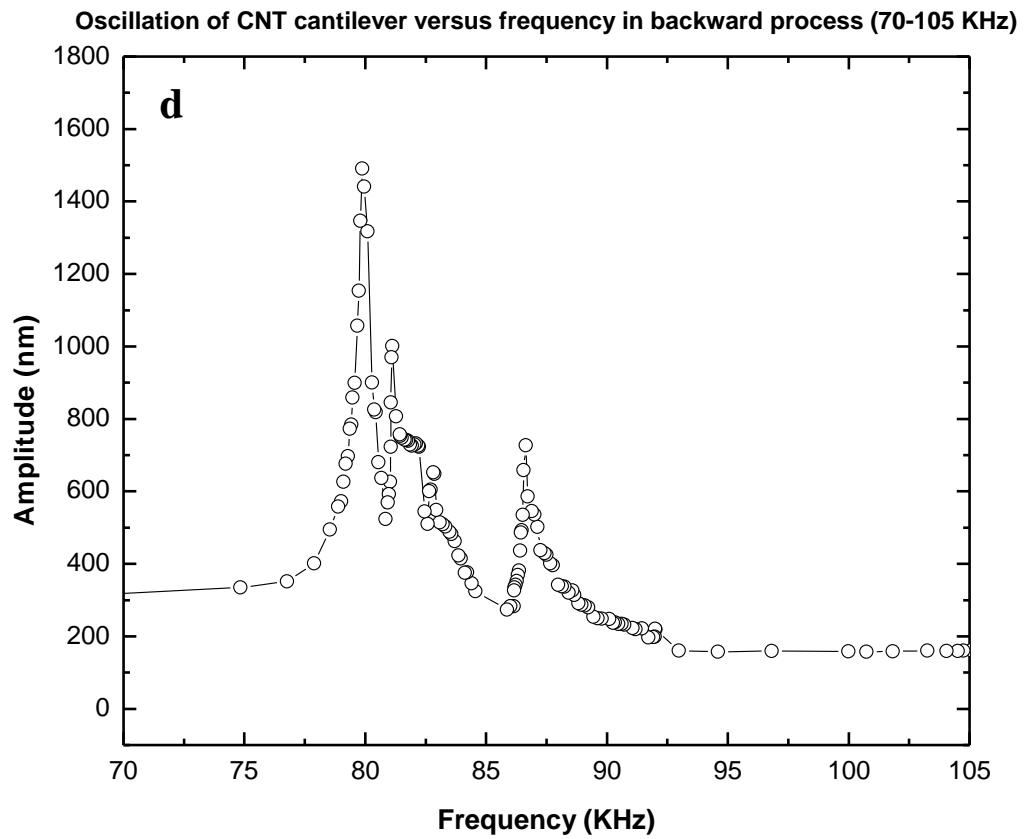
Full mapping of oscillation of CNT cantilever versus frequency



Oscillation of CNT cantilever versus frequency (109.57-109.64 KHz)







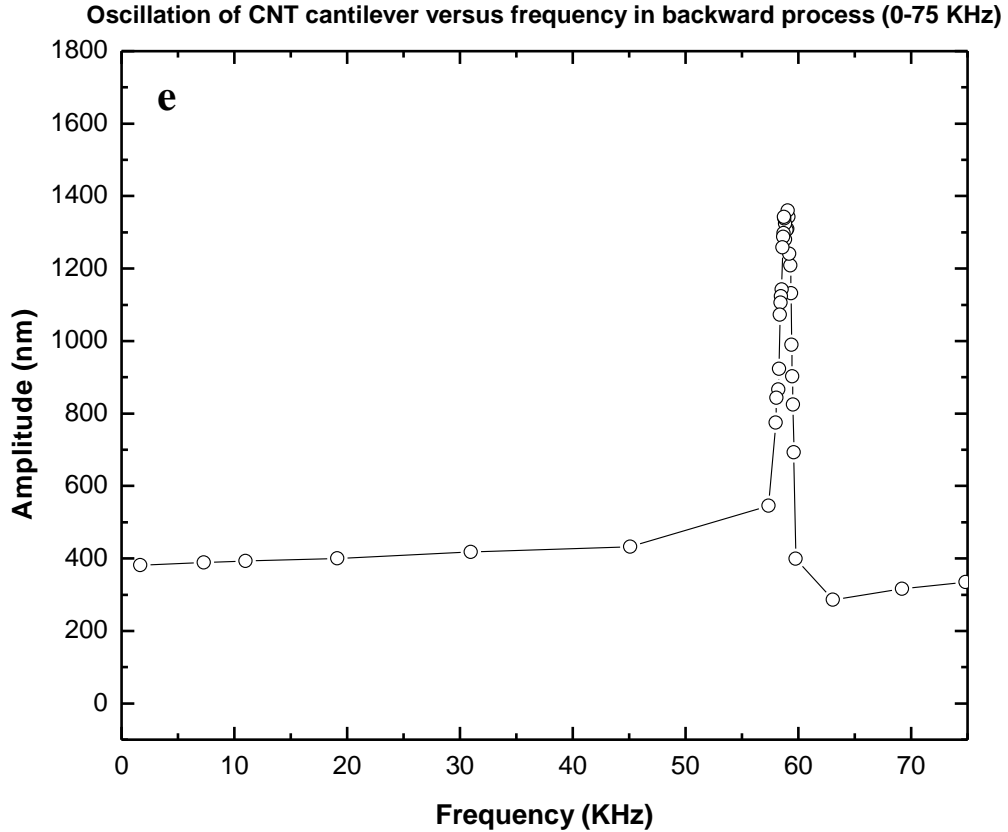


Fig 5. 6 Mapping of electrically induced mechanical resonance of CNT resonator (a) Full mapping of oscillation amplitude of CNT cantilever versus frequency. Peak 1, 2, 3 and 4 are observed successively. Zoomed-in curves indicate peak 1, 2, 3 and 4 are shown in (b), (c), (d) and (e) respectively.

Table 5.1 illustrates the resonant frequency corresponding to resonance peak 1, 2, 3 and 4 obtained from Fig 5.6, and bending modulus and quality factor of the CNT resonator system corresponding to each peak calculated using Equation 5.11. The density, inner diameter, outer diameter and the length of this CNT resonator obtained in Fig 5.4

remain the same for each resonance peak despite the contamination caused by EBID of amorphous carbon.

Table 5. 1 Parameters characterizing resonance of CNT system

	Peak 1	Peak 2	Peak 3	Peak 4
Resonant frequency	109.606KHz	108.680KHz	79.880KHz	59.073KHz
Bending modulus	1.41TPa	1.39TPa	0.75TPa	0.41TPa
Quality factor	9743	7728	132	65
Δf	11Hz	14Hz	604Hz	906Hz

As a matter of fact, from results obtained in Table 5.1 and Fig 5.7, the effective vibrating element during the experiment is found to be consisted of both the CNT itself, which is the principal constant part, and the increasingly added carbonaceous substance, indicated in Fig 5.7 as the dark parts, which means the characterization an analysis deal with the CNT-added carbon system rather than the pristine CNT before the experiment. The results in Table 5.1 also indicate that the contamination does not deposit at the irradiated tip in the real experimental scenario, but also along the rest part of the CNT.

With the decrease in resonant frequency, bending modulus of the nanotube resonator system keeps decreasing as shown in Table 5.1. Although the value of bending modulus for system at peak 4 has fallen to almost one-third of the value for system at peak 1, the resonator system preserves toughness which is still almost twice that of the steel.

Quality factor (Q), the ratio of the energy stored in the resonator to the energy loss per cycle due to damping, is one of the most important parameters characterizing a resonator. The inverse of the quality factor describes the relative energy loss per cycle

and characterizes the degree of loss in a resonator. Maximizing Q or minimizing the energy loss per cycle is thus important for most applications. Expression $Q=f/\Delta f$ is used to calculate the quality factor in Table 5.1, where f and Δf represent the resonant frequency and bandwidth which is the width of the range of frequencies for which the corresponding amplitude is at half of its peak value.

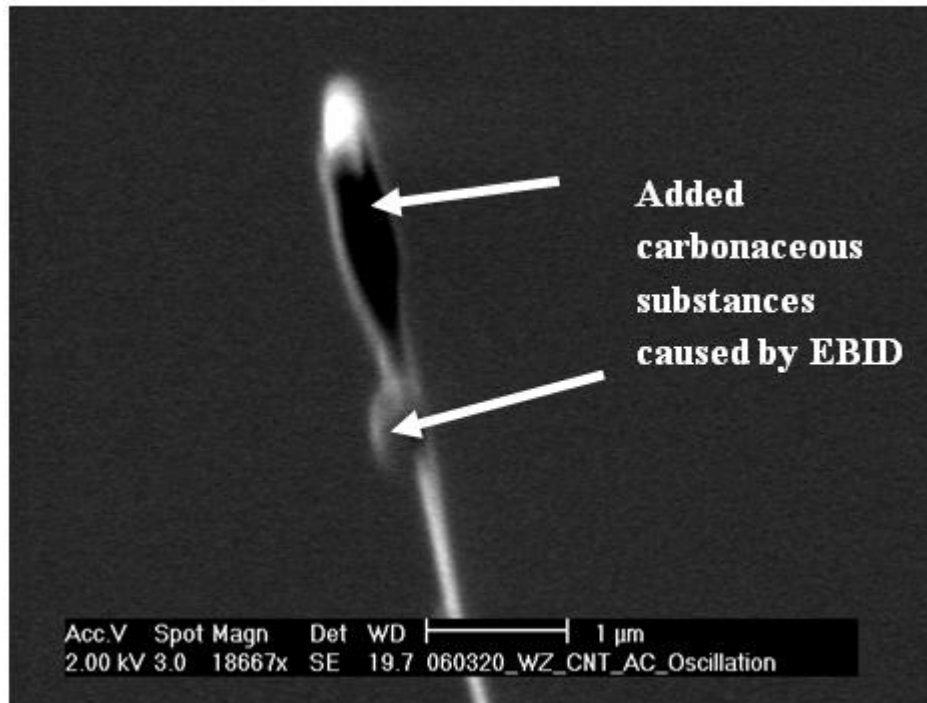


Fig 5. 7 Added carbonaceous substances caused by EBID during electron scanning, indicated as the black bulky part along the CNT.

The quality factor of this resonator decreases dramatically from peak 1 and peak 2 to peak 3 and peak 4, qualitatively speaking, which means the performance of this resonator gets worse and worse. The resultant smaller degree of internal dissipation when system operates at peak 1 and peak 2 thus imparts to CNT resonator low operating power levels and high attainable sensitivities. It is also important to note that large Q does imply a reduction of bandwidth, which can be seen from the broadening of

resonance peaks which are quantified and compared by Δf in Table 5.1. From peak 1 to peak 4, the value of Δf increases from 11 Hz, which is keen-edged, to 906 Hz, which amounts to almost 1 KHz. The extremely sharp peak around natural resonant frequency of this CNT resonator seems to be deleterious to performance of the potential NEMS devices.

As the devices keep being miniaturized, their respective Q s decrease with the surface-to-volume ratio. This phenomenon has been attributed to losses associated with dissipation at surfaces, giving promise for high quality factors from well-terminated structures such as CNTs [6] . Quality factors for the CNT resonator obtained in Table 5.1 at the initial stage (peak 1 and 2) of the experiment are consistent with the typical Q range for NEMS predicated, around 10,000-100,000 [77] .

5.4 Ultra-sensitive mass sensor

As need for rapid, ultrasensitive, and economical detection for biochemical entities like virus particles becomes ever more important, nanoscale fabrication techniques are increasingly being used to create nanomechanical sensors and highly sensitive lab-on-a-chip. With the extremely small dimensions and extraordinary properties such as high stiffness and resonant frequency which have already been demonstrated in previous sections, CNT becomes a promising candidate for building block of ultra-sensitive sensing applications such as mass sensor, biomolecule and species sensor. The

capability and feasibility of CNT resonator in the experiment acting as ultra-sensitive mass sensor are examined in this section.

The resonance frequency, f , of an oscillating cantilever is expressed as

$$f = \frac{1}{2\pi} \sqrt{\frac{k}{m^*}} \quad (5.12)$$

where k is the spring constant and m^* the effective mass of the cantilever system. In the experiment, $m^* = m_{CNT} + m_C$, where m_C is the added mass of carbonaceous substances induced by EBID. If the carbonaceous substances deposited onto the CNT system before the first resonance peak is ignored, or CNT system at the first resonance peak is treated as the pristine CNT reference, the mass of the system at first resonance peak, which will be also used as the reference for subsequent calculation, is calculated as 20.83 *attogram* according to Table 5.1 and Equation 5.12. As shown in Equation 5.12, if the spring constant of the cantilever system remains constant, or the changes in spring constant, Δk , are negligible during the experiment, the resonant frequency shifts is mainly affected by the deposition mass, which increases as the deposition time increases. As observed in Fig 5.7, it is reasonable to assume that the added mass locates at the free end of the CNT cantilever for this is the investigated region scanned by electron beam. Therefore, the change in mass in relation to the change in resonant frequency of the whole cantilever system is derived from Equation 5.12 as

$$\Delta m = \frac{k}{4\pi^2} \left(\frac{1}{f_1^2} - \frac{1}{f_0^2} \right) \quad (5.13)$$

where f_0 is the initial resonant frequency, and f_1 is the resonant frequency after the mass

addition. Through straightforward derivation, spring constant is derived as $k = \frac{12EI}{L^3}$

where E is the bending modulus, I is the moment of inertia given by $I = \frac{\pi(r_o^4 - r_i^4)}{4}$, r_o

and r_i are the outer and inner radii of the nanotube, respectively. Thus the spring

constant is obtained in the following expression

$$k = \frac{3E\pi(r_o^4 - r_i^4)}{L^3} \quad (5.13)$$

If the cantilever beams is calibrated by obtaining its spring constant, k , using the unloaded resonant frequency measurement f , quality factor Q and bending modulus of the cantilever beam, with the values for r_o , r_i , E and L are $13.27nm$, $5.365nm$, $1.41TPa$ and $34.37\mu m$ respectively, as obtained in previous sections, the resultant spring constant k is $9.878 \times 10^{-6} N/m$. Table 5.2 illustrates the added mass and hence the mass sensitivity for the nanotube system at the time corresponding to peak 2, 3 and 4 respectively, where $f_0 = 109.606KHz$.

Table 5. 2 Added mass and mass sensitivity for peak 1, 2, 3 and 4

1attogram= 10^{-18} gram	Peak 1	Peak 2	Peak 3	Peak 4
Resonant frequency	109.606KHz	108.680KHz	79.880KHz	59.073KHz
$\Delta m = \frac{k}{4\pi^2} \left(\frac{1}{f_1^2} - \frac{1}{f_0^2} \right)$	NA	0.357attogram	18.38attogram	50.88attogram
Mass sensitivity				

$\frac{\Delta f}{\Delta m}$	NA	2599	1621	993
		<i>Hz/attogram</i>	<i>Hz/attogram</i>	<i>Hz/attogram</i>

Fabulous performance of the investigated CNT resonator as ultra-sensitive mass sensor has been demonstrated from Table 5.2. The measured added mass to the nanotube cantilever when this cantilever system reaches the state of peak 2, peak 3 and peak 4 are 0.357 attogram, 18.38 attogram and 50.88 attogram respectively. This attogram-sensing capability of CNT resonator enables its potential utilization for sensing even a single small virus, usually with the mass around a few attogram. Besides, the measured mass sensitivity for the CNT resonator is also outstanding. With an added mass to the resonator as small as 1 attogram, the resultant output will demonstrate a frequency shift in the kilohertz range. However, doubts regarding the added mass and mass sensitivity for system at peak 2 might be raised for the frequency shift shown at peak 2 is be big enough to be reasonably distinguishable; hence the resultant extremely small added mass and high mass sensitivity might not hold. Nevertheless, even considering peak 3 and peak 4 only, where the frequency shifts relative to peak 1 are large enough for distinguishing and measuring reliably, the performances are still extraordinary and excel the reported mass sensitivity of only 6.3 Hz/attogram [78] , where silicon-based NEMS resonator is investigated. Once integrated with on-chip antibody-based recognition and sample concentrators, this kind of CNT resonators may prove to be viable candidates for ultrasensitive detection of virus particles.

In the above discussion, the spring constant k is assumed invariable or the change in spring constant, Δk , is negligible. Moreover, the absorption of carbonaceous substance

is assumed to locate at the free end of the cantilever which minimizes the change in static deflection due to absorption. Nevertheless, obtained from Equation 5.12, changes in resonance frequency can result from either mass change or variation in k . The overall changes in resonance frequency are the result of competition between effects of variations in mass and spring constant: when the effect of increase in spring constant dominates, resonance frequency increases; when the effect of increase in system mass dominates, resonance frequency decreases, which has been observed in the experiments. In some cases it can also be possible that changes in adsorbed mass exactly balance changes in spring constant, thus resulting in negligible change in resonance frequency. From Table 5.1 variations in spring constant of this nanotube system are observed obviously, which renders the previous assumption of constant spring constant questionable. Adsorption-induced surface stress affects the spring constant of this CNT cantilever. When molecules (such as the amorphous carbon here in this experiment) adsorb on a cantilever surface, the resonance frequency of the cantilever changes due to mass loading. In addition to resonance frequency change, deflection (bending) may change due to adsorption-induced differential surface stress, δs . This differential surface stress ($\delta s = s_1 - s_2$, where s_1 and s_2 are the induced stresses on the top and bottom surface of the cantilever) can be large if the adsorption on one face of the cantilever is different from the other, resulting in measurable bending.

By designing cantilevers with localized adsorption areas at the terminal end of the cantilever (end loading), the contribution from differential surface stress can be minimized and changes in resonance frequency can be entirely attributed to mass

loading. Thus, it appears that four general conditions can arise due to adsorption of molecules on a cantilever:

(1) Adsorption-induced changes in spring constant can be negligible-change in resonance frequency is entirely the result of mass loading.

(2) Changes in resonance frequency due to mass loading may be negligible, but change in static deflection due to adsorption is readily observable-differential surface stress on the cantilever is high.

(3) Adsorption-induced change in spring constant is large enough to change the resonance frequency-resonance frequency is controlled by change in spring constant while the contribution of mass loading is negligible.

(4) Change in resonance frequency is a combination of effects from mass loading and variation in spring constant.

Although the adsorption of carbon molecules in the vicinity of the tip has been observed most obviously, the adsorption (or contamination) along the entire CNT cannot be ignored without discrimination.

Therefore, Equation 5.12 is modified as

$$f_1 = \frac{1}{2\pi} \sqrt{\frac{k + \Delta k}{m + \Delta m}} \quad (5.14)$$

by taking the above consideration into account and considering change in resonance frequency as a combination of effects from both mass loading and variation in spring constant. In most cases, as a matter of fact, changes in k and m due to adsorption are

very small and hence the resonance frequency after adsorption is approximated by transforming Equation 5.14 into

$$f_1 = f_0 \left(1 + \frac{1}{2} \left(\frac{\Delta k}{k} - \frac{\Delta m}{m} \right) \right) \quad (5.15)$$

where f_0 is the resonant frequency before adsorption. This expression holds as long as $\Delta k \ll k$ and $\Delta m \ll m$ so the high-order terms are ignored. m is the unloaded mass of the CNT resonator system before adsorption, which is identified at peak 1 using Eq. (1).

Table 5.3 illustrates the added mass to and the mass sensitivity for this nanotube resonator system after utilizing Equation 5.15. Comparing Table 5.3 with Table 5.1, the added mass for peak 4 is found to be larger in Table 5.1 than in Table 5.3 and hence the corresponding mass sensitivity is smaller in Table 5.1.

Table 5. 3 Added mass and mass sensitivity of CNT resonator considering loaded mass and variational spring constant

1attogram= 10^{-18} gram	Peak 1	Peak 2	Peak 3	Peak 4
Resonant frequency	109.606KHz	108.680KHz	79.880KHz	59.073KHz
Bending modulus E	1.41TPa	1.39TPa	0.75TPa	0.41TPa
Spring constant $k = \frac{3E\pi(r_o^4 - r_i^4)}{L^3}$	9.878×10^{-6} N/m	9.738×10^{-6} N/m	5.254×10^{-6} N/m	2.872×10^{-6} N/m
$\frac{\Delta k}{k}$	NA	0.014	0.468	0.709
$\frac{f_1}{f_0}$	NA	0.992	0.729	0.539
Added mass $\Delta m = m \left(2 + \frac{\Delta k}{k} - 2 \frac{f_1}{f_0} \right)$	NA	0.6249 attogram	21.04 attogram	33.97 attogram
Mass sensitivity $\frac{\Delta f}{\Delta m}$	NA	1485 Hz/attogram	1413 Hz/attogram	1488 Hz/attogram

From the values of $\frac{\Delta k}{k}$ obtained in Table 5.3, variations in spring constant are found to play more important roles in affecting the resonant frequency of this CNT resonator system as the experiment continues. At peak 4, consequentially, neglect of the changes in spring constant yields overestimation of the added mass and the underestimation of the mass sensitivity as obtained in Table 5.1. However, the assumption $\Delta k \ll k$ and $\Delta m \ll m$ are not valid at both peak 3 and peak 4 in Table 5.3, which hence lends little credibility to the calculation of added mass and mass sensitivity obtained there. To achieve more accurate results, complete series expansions of Equation 5.14 are required. The resultant expression for added mass is derived as

$$\Delta m = m \frac{\left(2 + \frac{\Delta k}{k} - 2 \frac{f_1}{f_0} \right)}{\frac{\Delta k}{2k} + 1} \quad (5.16)$$

Since the assumption $\Delta k \ll k$ and $\Delta m \ll m$ is valid for peak 2, the results obtained for peak 2 in Table 5.3 describe the performance of resonator in reality quite well while the results for peak 2 in Table 5.2 only deviate from the real cases with a small difference since the quantities of changes in both the mass and the spring constant are very small.

Replacing Δm in Table 5.3 with Equation 5.16, loaded mass and mass sensitivity of CNT resonator considering loaded mass and variational spring constant are obtained in Table 5.4. The results attained in Table 5.4 are based on the assumption that the CNT system at resonance peak 1 is the pristine CNT; nevertheless, the EBID of carbonaceous

substances onto the CNT exists as long as the electron beam is on, which means the calculated mass 20.83 attogram for the CNT system at resonance peak 1 is actually the sum of mass of CNT and the added carbonaceous substance till that moment. The $\Delta m-t$ relationship is illustrated in Fig 5.8 as follows according to the results in Table 5.4.

Table 5. 4 Loaded mass and mass sensitivity of CNT resonator considering loaded mass and variational spring constant

1attogram= 10^{-18} gram	Peak 1	Peak 2	Peak 3	Peak 4
Resonant frequency	109.606KHz	108.680KHz	79.880KHz	59.073KHz
Bending modulus E	1.41TPa	1.39TPa	0.75TPa	0.41TPa
Spring constant $k = \frac{3E\pi(r_o^4 - r_i^4)}{L^3}$	9.878×10^{-6} N/m	9.738×10^{-6} N/m	5.254×10^{-6} N/m	2.872×10^{-6} N/m
$\frac{\Delta k}{k}$	NA	0.014	0.468	0.709
$\frac{f_1}{f_0}$	NA	0.992	0.729	0.539
Added mass $\Delta m = m \frac{\left(2 + \frac{\Delta k}{k} - 2 \frac{f_1}{f_0}\right)}{\frac{\Delta k}{2k} + 1}$	NA	0.6206 attogram	17.05 attogram	25.08 attogram
Mass sensitivity $\frac{\Delta f}{\Delta m}$	NA	1495 Hz/attogram	1744 Hz/attogram	2015 Hz/attogram

According to Fig 5.8, a linear relationship between the added mass and time both referred to the first resonance peak is revealed and hence it is reasonable to assume that this relationship holds for the added mass and time before the first resonance peak observed as well. Therefore, the mass for pristine CNT is extracted in Fig 5.9, which plots the effective mass of CNT system versus time.

The observed four resonance peaks correspond to the time 10, 11, 44 and 57 minutes respectively. The mass for pristine CNT before the experiment is thus extracted as the interception value on Y axis when time equals to 0 minute on the first order fitting line. The value is attained as 15.54 attogram.

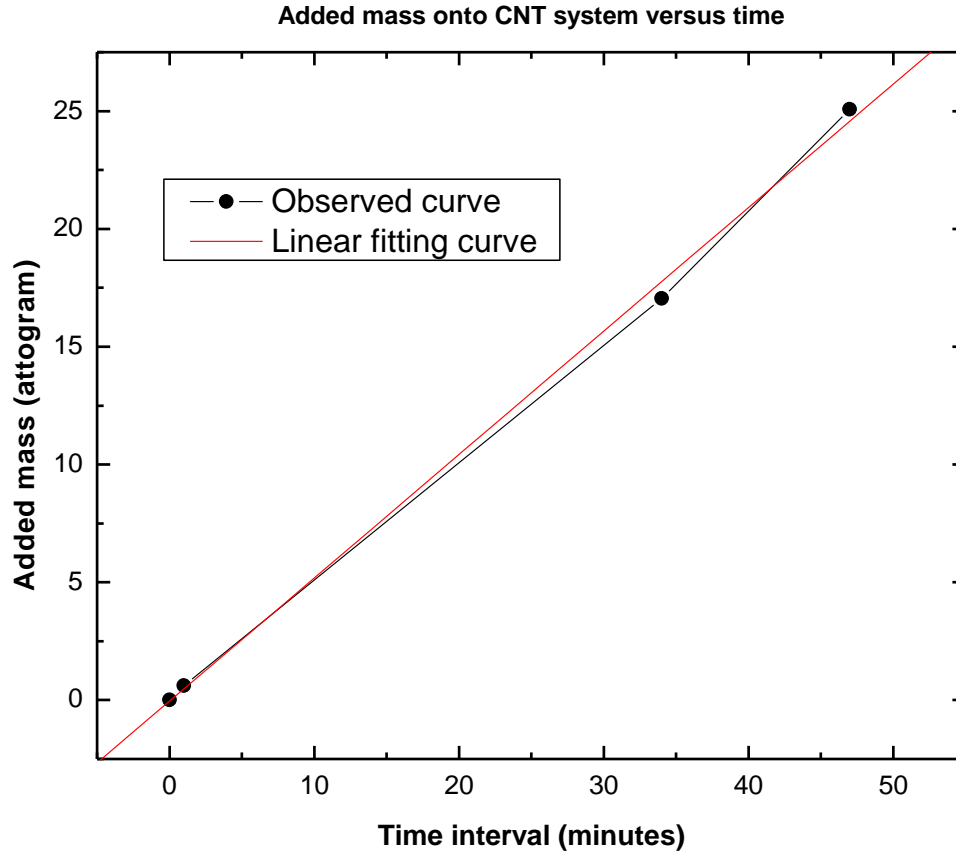


Fig 5. 8 $\Delta m-t$ curve reveals a linear relationship between the added mass referred to the first resonance peak and time, the time corresponding to each peak is recorded in the experiment.

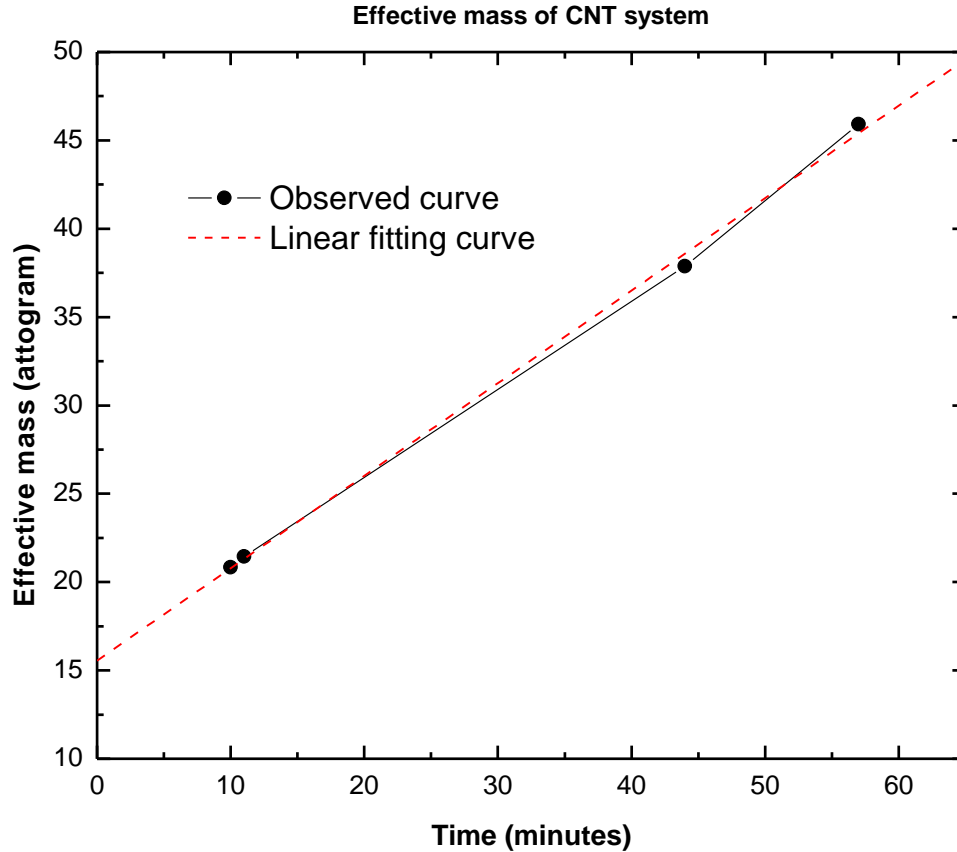


Fig 5. 9 Effective mass of CNT system versus time. The mass for pristine CNT is extracted by intercepting the first order fitting line onto the Y axis and the value is 15.54 attogram for this CNT. Time values for observed four resonance peaks are 10, 11, 44 and 57 minutes respectively.

Using the well recognized bending modulus value ($1.8TPa$) to calculate the spring constant for this pristine CNT and the resultant value is $12.610 \times 10^{-6} N/m$. Substituting extracted mass (15.54 attogram) and the above obtained spring constant for pristine CNT into Equation 5.12, the fundamental resonance frequency for this pristine CNT is obtained as $143.360 KHz$. Therefore Table 5.4 is further revised into Table 5.5 as shown below.

Table 5. 5Revised loaded mass and mass sensitivity of CNT resonator using pristine CNT mass.

1 attogram= 10^{-18} gram	P-CNT*	Peak 1	Peak 2	Peak 3	Peak 4
Resonant frequency	143.360 <i>KHz</i>	109.606 <i>KHz</i>	108.680 <i>KHz</i>	79.880 <i>KHz</i>	59.073 <i>KHz</i>
Bending modulus E	1.80TPa	1.41TPa	1.39TPa	0.75TPa	0.41TPa
Spring constant $k = \frac{3E\pi(r_o^4 - r_i^4)}{L^3}$	12.610×10^{-6} <i>N/m</i>	9.878×10^{-6} <i>N/m</i>	9.738×10^{-6} <i>N/m</i>	5.254×10^{-6} <i>N/m</i>	2.872×10^{-6} <i>N/m</i>
$\frac{\Delta k}{k}$	NA	0.217	0.228	0.583	0.772
$\frac{f_1}{f_0}$	NA	0.765	0.758	0.557	0.412
Added mass $\Delta m = m \frac{\left(2 + \frac{\Delta k}{k} - 2 \frac{f_1}{f_0}\right)}{\frac{\Delta k}{2k} + 1}$	NA	5.29 <i>attogram</i>	5.9106 <i>attogram</i>	22.34 <i>attogram</i>	30.37 <i>attogram</i>
Mass sensitivity $\frac{\Delta f}{\Delta m}$	NA	6380 <i>Hz/attogram</i>	5867 <i>Hz/attogram</i>	2842 <i>Hz/attogram</i>	2775 <i>Hz/attogram</i>

* P-CNT stands for pristine CNT. The bending modulus for pristine CNT is chosen as 1.80TPa.

5.5 Summary

The above type of measurement and characterization is based on several assumptions. First, one end of the nanotube is affixed, and it cannot move or be loose during the measurement. Moreover, there is no irreversible structural deformation during the oscillation.

In any case, the CNT resonator under investigation still exhibits great potential in ultra-sensitive applications such as virus sensor or mass sensor. The ultrasmall mass sensing

capability and ultrasensitive mass sensitivity enable the catalytic CVD grown MWNT promising candidate for novel sensing applications.

CHAPTER 6

CONCLUSIONS AND RECOMMENDATIONS

6.1 Conclusions

In the first part of this project, the catalytic CVD growth for synthesizing MWNTs is investigated and the effects of various parameters influencing the growth process are also discussed. FeCl_3 solution provides the essential iron catalyst for the growth of CNT in the experiments. With the concentration of catalyst increases, the density of grown CNTs increases. When duration of growth is elevated, longer CNTs are observed. One undesirable result of longer growth time is the resultant thicker diameters of CNTs. While another critical issue of longer growth duration is the deposition of amorphous carbon layer. Temperature also acts an important role in CNT growth. When growth temperature is low, the yield of CNTs is also low and the distribution density of growth is sparse as well. On the other hand, when the growth temperature is too high, the morphology and distribution density of the resultant CNTs are also undesirable.

The second part of this project investigates the fabrication, actuation and detection of CNT based resonator. Method for electrical actuation and *in situ* harmonic detection of electrically induced mechanical resonance of single MWNT cantilever is developed for the subsequent *in situ* investigation of performance of cantilevered CNT resonator prototype under DC and AC bias in SEM. SEM and TEM enable the great capability for characterizing CNT NEMS devices.

The last part of this project engages in the characterization of accomplished CNT resonator and analysis of the experimental results attained. Important parameters which describe and characterize CNT resonator are calculated and show that the CVD grown CNTs possess superior mechanical properties compared with conventional materials. An interesting and insightful phenomenon observed in the experiments is the continuous redshift in resonant frequency and broadening of resonance peak of the CNT resonator, which inspires the subsequent investigation on the capability and feasibility of CNT resonator acting as ultra-sensitive mass sensor. Discussion of the relationship between carbon contamination, spring constant of CNT system and resonant frequency shift has also been conducted and shows that CNT resonator under investigation exhibits sub-attogram sensing capability in the experiments, which holds great potential in various applications such as biomolecule and virus sensing.

6.2 Recommendations for future work

Within sixteen years of the discovery of CNTs, the merits of CNTs based sensors have shown strong potential to make huge impact in future sensor industry. However, the real mass production and utilization of these sensors will not emerge and unfold overnight. Various remaining challenges need to be addressed before the full potential of CNTs for sensor applications can be realized.

First, the production of pure and uncontaminated CNT is very costly. There are only few companies that produce CNTs for commercial applications. In addition to it, there is a lack of detailed understanding and accurate description of growth mechanism of

CNTs, which results in the incapability of synthesizing CNTs in a desired way. As described in previous chapters, the properties of CNTs are vulnerable to the defects exhibited in the structures, even the displacement of one carbon atom can result in a CNT with totally different properties. As a result, an efficient growth approach to synthesize structurally perfect nanotubes at large scales is highly demanded in order to realize CNTs based NEMS in the future.

In addition to the above challenge in the synthesis stage, more advanced detection and characterization techniques need to be developed. Despite the simplicity of the *in situ* detection scheme achieved by SEM and TEM in this project, it is hard to extract quantitative information about the vibrations of the resonator as the detector should be capable of taking images faster than the resonance frequency of the studied structure, which might lie in the megahertz or gigahertz range. Moreover, this is a very invasive measurement, as discussed in the thesis, which induces the damages to the system under investigation and renders the incapability of reusing the CNT devices. And finally, it is also impossible to rely on SEM or TEM for various sensing applications in reality, such as everyday purposes or industry utilizations. In order to implement the CNTs NEMS in real applications, fully-electrical actuation and detection scheme, which can perform the ultralow level signal detection, is highly desirable and needs to be developed before any real commercial product of CNTs NEMS can be realized.

Another issue concerning the utilization of CNTs is their toxicity [79] , [80] . On the basis of their experiments, researchers have suggested that CNTs possess health risks. They reasoned that humans can potentially be exposed to CNTs by inhalation because unprocessed CNTs are lightweight and, therefore, can become airborne. If CNTs reach

the lung, they can agglomerate and fill the air passages that may lead to suffocation. These reports warrant an in-depth study about the toxicology of CNTs to come up with a final conclusion with respect to their acceptance by the human immune system.

Lastly, the process from proof of concept in the laboratory of the CNTs based devices to the commercial market should be expedited greatly as the competition from other novel materials and technologies continue to emerge.

BIBLIOGRAPHY

- [1] Blencowe, M. P. (2004). Quantum electromechanical systems . *Physics Reports* , 159-222.
- [2] Roukes, M. L. (2001). Nanoelectromechanical systems face the future. *Physics World* , 25-31.
- [3] Roukes, M. L. (2001, September). Plenty of Room Indeed. *Scientific American* , pp. 48-57.
- [4] Dresselhaus, M. S. (1992). Down the straight and narrow. *Nature* , 195-196.
- [5] M.S.Dresselhaus, G. a. (1996). *Science of Fullerenes and Carbon Nanotubes*. New York: Academic Press.
- [6] Ekinici, K. a. (2005). Nanoelectromechanical systems. *Review of Scientific Instruments* , 061101–1, 061101–12.
- [7] Craighead, H. G. (2000). Nanoelectromechanical systems. *Science*, 1532.
- [8] Nguyen, C. T., Wong, A.-C., and Hao, D. (1999). Tunable, switchable, high-q vhf microelectromechanical bandpass filters. *IEEE International Solid-State Circuits Conference*, volume 448, page 78, San Francisco, CA.
- [9] LaHaye, M. D., Buu, O., Camarota, B., and Schwab, K. C. (2004). Approaching the quantum limit of a nanomechanical resonator. *Science*, 304:74–77.
- [10] Ilic, B., Krylov, S., Senaratne, W., Ober, C., Neuzil, P., and Craighead, H. G. (2004). Attogram detection using nanoelectromechanical oscillators. *Journal of Applied Physics*, 95:3694–3703.
- [11] Cleland, A. N., Pophristic, M., and Ferguson, I. (2001). Single-crystal aluminum nitride nanomechanical resonators. *Applied Physics Letters*, 79(13):2070–2072.
- [12] Zalalutdinov, M., Aubin, K. L., Reichenbach, R. B., Zehnder, A. T., Houston, B., Parpia, J. M., and Craighead, H. G. (2003). Shell-type micromechanical actuator and resonator. *Applied Physics Letters*, 83(18):3815–3817.
- [13] Sekaric, L., Carr, D. W., Evoy, S., Parpia, J. M., and Craighead, H. G. (2002). Nanomechanical resonant structures in silicon nitride: fabrication, operation and dissipation issues. *Sensors and Actuators A - Physical*, 101(1-2):215–219.
- [14] Nguyen, C. T. (1999). Micromechanical components for miniaturized low-power communications (invited). *In 1999 IEEE MTT-S international Microwave Symposium FR MEMS Workshop*, pages 48–77, Anaheim, California.

-
- [15] Ekinci, K., Huang, X. M. H., and Roukes, M. (2004). Ultrasensitive nanoelectromechanical mass detection. *Applied Physics Letters*, 84:4469–4471.
- [16] Rugar, D., Budakian, R., Mamin, H. J., and Chui, B. W. (2004). Single spin detection by magnetic resonance force microscopy. *Nature*, 430(6997):329–332.
- [17] Iijima. (1991). Helical microtubules of graphitic carbon. *Nature*, 56.
- [18] Huang, S., Cai, X., and Liu, J. (2003a). Growth of millimeter-long and horizontally aligned single-walled carbon. *Journal of American Chemical Society*, 125:5636–5637.
- [19] Minot, E. (2004). Tuning the band structure of carbon nanotubes. Doctoral thesis, Cornell University.
- [20] R. Saito et al. (1998). *Physical Properties of Carbon Nanotubes*, Imperial College press, 3th edition.
- [21] P. Giannozzi et al. (2003). Oxygen adsorption on graphite and nanotubes. *The Journal of Chemical Physics*. 118:1003.
- [22] H. Ulbricht et al. (2002). Physisorption of molecular oxygen on single-wall carbon nanotube bundles and graphite. *Phys. Rev. B*. 66: 075404.
- [23] S. Dag et al. (2003). Systematic study of adsorption of single atoms on a carbon nanotube. *Phys. Rev. B*. 67: 165424.
- [24] P. G. Collins et al. (2000). Extreme Oxygen Sensitivity of Electronic Properties of Carbon Nanotubes. *Science*. 287: 1801.
- [25] P. Qi et al. (2003). Toward Large Arrays of Multiplex Functionalized Carbon Nanotube Sensors for Highly Sensitive and Selective Molecular Detection. *Nano Lett.* 3: 347.
- [26] P. J. F. Harris. (1999). *Carbon Nanotubes and Related Structures*, Cambridge University press, 1th edition.
- [27] www.fundp.ac.be/~phlambin/Nanotube/knee.html.
- [28] www.slb.com/seed/en/watch/fullerenes/breakthrough.htm.
- [29] M. C.C. Lin et al. (2001). Synthesis of carbon nanotubes using polycyclic aromatic hydrocarbons as carbon sources in an arc discharge. *Materials Science and Engineering: C*. 4: 138-142.
- [30] C. Dekker. (1998). Carbon Nanotubes as Molecular Quantum Wires. *Physics Today*. 52: 22-28.

-
- [31] M. J. Bronikowski et al. (2001). Gas-phase production of carbon single-walled nanotubes from carbon monoxide via the HiPco process: A parametric study. *Journal of Vacuum Science and Technology A*. 19: 1800.
- [32] Tans, S. J., Verschueren, A. R. M., and Dekker, C. (1998). Room-temperature transistor based on a single carbon nanotube. *Nature*. 393:49-52.
- [33] Zhou, C. W., Kong, J., and Dai, H. J. (2000). Intrinsic electrical properties of individual single-walled carbon nanotubes with small band gaps. *Physical Review Letters*. 84(24):5604-5607.
- [34] Datta S. (1995). *Electron Transport in Mesoscopic Systems*. Cambridge University Press.
- [35] Kong, J., Yenilmez, E., Tomblor, T. W., Kim, W., Dai, H. J., Laughlin, R. B., Liu, L., Jayanthi, C. S., and Wu, S. Y. (2001). Quantum interference and ballistic transmission in nanotube electron waveguides. *Physical Review Letters*. 8710(10): 106801.
- [36] Liang, W. J., Bockrath, M., Bozovic, D., Hafner, J. H., Tinkham, M., and Park, H. (2001). Fabry-perot interference in a nanotube electron waveguide. *Nature*. 411(6838):665-669.
- [37] Javey, A., Guo, J., Wang, Q., Lundstrom, M., and Dai, H. J. (2003). Ballistic carbon nanotube field-effect transistors. *Nature*. 424(6949):654–657.
- [38] Yaish, Y., Park, J. Y., Rosenblatt, S., Sazonova, V., Brink, M., and McEuen, P. L. (2004). Electrical nanoprobng of semiconducting carbon nanotubes using an atomic force microscope. *Physical Review Letters*. 92(4):046401.
- [39] Kane, C. L., Mele, E. J., Lee, R. S., Fischer, J. E., Petit, P., Dai, H., Thess, A., Smalley, R. E., Verschueren, A. R. M., J., T. S., and Dekker, C. (1998). Temperature-dependent resistivity of single-wall carbon nanotubes. *Europhysics Letters*. 41:683-688.
- [40] Dresselhaus, M. S., Dresselhaus, G., and Avouris, P. (2001). *Carbon Nanotubes*. Springer.
- [41] Heyd, R., Charlier, A., and McRae, E. (1997). Uniaxial-stress effects on the electronic properties of carbon nanotubes. *Physical Review B*. 55(11):6820-6824.
- [42] Yang, L., Anantram, M. P., Han, J., and Lu, J. P. (1999). Band-gap change of carbon nanotubes: Effect of small uniaxial and torsional strain. *Physical Review B*. 60(19):13874-13878.
- [43] Overney, G., Zhong, W., and Tomanek, D. (1993). Structural rigidity and low-frequency vibrational-modes of long carbon tubules. *Zeitschrift Physik D*, 27:9396.

- [44] Lu, J. (1997). Elastic properties of carbon nanotubes and nanoropes. *Physical Review Letters*. 79:1297-1300.
- [45] Hernandez, E., Goze, C., Bernier, P., and Rubio, A. (1999). Elastic properties of C and $B_xC_yN_z$ composite nanotubes. *Physical Review Letters*. 80:4502-4505.
- [46] B. I. Yakobson, in *Fullerenes-Recent Advances in the Chemistry and Physics of Fullerenes and Related Materials*, R. S. Ruoff and K. M. Kadish, Eds. (Electrochemical Society, Pennington, NJ, 1997), vol. 5 (97-42), pp. 549-560.
- [47] Treacy, M. M. J., Ebbesen, T. W., and Gibson, J. M. (1996). Exceptionally high Young's modulus observed for individual carbon nanotubes. *Nature*. 381(6584):678-680.
- [48] Krishnan, A., Dujardin, E., Ebbesen, T. W., Yianilos, P. N., and Treacy, M. M. J. (1998). Young's modulus of single-walled nanotubes. *Physical Review B*. 58(20):14013-14019.
- [49] Poncharal, P., Wang, Z. L., Ugarte, D., and de Heer, W. A. (1999). Electrostatic deflections and electromechanical resonances of carbon nanotubes. *Science*. 283(5407):1513-1516.
- [50] Gao, R. P., Wang, Z. L., Bai, Z. G., de Heer, W. A., Dai, L. M., and Gao, M. (2000). Nanomechanics of individual carbon nanotubes from pyrolytically grown arrays. *Physical Review Letters*. 85(3):622-625.
- [51] Wong, E. W., Sheehan, P. E., and Lieber, C. M. (1997). Nanobeam mechanics: Elasticity, strength, and toughness of nanorods and nanotubes. *Science*. 277(5334):1971-1975.
- [52] Minot, E. D., Yaish, Y., Sazonova, V., Park, J. Y., Brink, M., and McEuen, P. L. (2003). Tuning carbon nanotube band gaps with strain. *Physical Review Letters*. 90(15):156401.
- [53] Purcell et al. (2002) Hot Nanotubes: Stable Heating of Individual Multiwall Carbon Nanotubes to 2000 K Induced by the Field-Emission Current. *Physical Review Letters*. 88: 105502.
- [54] <http://www.mos.org/sln/SEM/>.
- [55] <http://www.matter.org.uk/tem/>.
- [56] Interactive Nano-Visualization in Science and Engineering Education (INVSEE): <http://invsee.asu.edu/Invsee/invsee.htm>.
- [57] V. I. Merkulov, D. H. Lowndes, Y. Y. Wei, G. Eres, E. Voelkl. (2000). Patterned growth of individual and multiple vertically aligned carbon nanofibers. *Applied Physics Letters*. 76: 3555.

- [58] Y. C. Choi, Y. M. Shin, S. C. Lim, D. J. Bae, Y. H. Lee, B. S. Lee, D. Chung. (2000). Effect of surface morphology of Ni thin film on the growth of aligned carbon nanotubes by microwave plasma-enhanced chemical vapor deposition. *Journal of Applied Physics*. 88: 4898.
- [59] C. Bower, O. Zhou, W. Zhu, D. J. Werder, S. H. Jin. (2000). Nucleation and growth of carbon nanotubes by microwave plasma chemical vapor deposition. *Applied Physics Letters*. 77: 2767.
- [60] R. T. Baker. (1989). Catalytic growth of carbon filaments. *Carbon*. 27: 315.
- [61] C.P. Deck and K. Vecchio. (2006). Prediction of carbon nanotube growth success by the analysis of carbon-catalyst binary phase diagrams. *Carbon*. 44 (2): pp. 267–275.
- [62] C.J. Lee *et al.* (2000). Synthesis of bamboo-shaped multiwalled carbon nanotubes using thermal chemical vapor deposition. *Chemical Physics Letters*. 323: 560-565.
- [63] N. de Jonge, Y. Lamy, K. Schoots and T.H. Oosterkamp. (2002). High brightness electron beam from a multi-walled carbon nanotube. *Nature*. 420: 393–395.
- [64] <http://www.applied-nanotech.com/cntproperties.htm#Electronic%20Properties>.
- [65] H. Jiang, M.F. Yu, B. Liu, and Y. Huang. (2004). Intrinsic Energy Loss Mechanisms in a Cantilevered Carbon Nanotube Beam Oscillator. *Physical Review Letters*. 93: 185501.
- [66] Z.L. Wang and C. Hui. (2003). *Electron Microscopy of nanotubes*. Kluwer Academic Publisher.
- [67] Broughton, J. Q., Meli, C. A., Vashishta, P., and Kalia, R. K. (1997). Direct atomistic simulation of quartz crystal oscillators: Bulk properties and nanoscale devices. *Physical Review B*. 56: 611.
- [68] Phillips, R. (2001). *Crystals, Defects and Microstructures*. Cambridge University.
- [69] Greywall, D. S., Yurke, B., Busch, P. A., Pargellis, A. N., and Willett, R. L. (1994). Evading amplifier noise in nonlinear oscillators. *Physical Review Letters*. 72(19):2 992-2995.
- [70] Turner, K. L., Miller, S. A., Hartwell, P. G., MacDonald, N. C., Strogatz, S. H., and Adams, S. G. (1998). Five parametric resonances in a microelectromechanical system. *Nature*. 396 (6707):149-152.

-
- [71] S.P. Timoshenko and J.M. Gere. (1961). *Theory of Elastic Stability*. McGraw-Hill.
- [72] S.S. Rao. (1995). *Mechanical Vibrations*. Addison-Wesley. 523-527 (Chapter 8).
- [73] <http://www.pa.msu.edu/cmp/csc/ntproperties/quickfacts.html>.
- [74] C. H. Ke et al. (2005). Numerical Analysis of Nanotube Based NEMS Devices-Part II: Role of Finite Kinematics, Stretching and Charge Concentrations. *Journal of Applied Mechanics*. 72: 726.
- [75] Mitsumasa Nishio et al. (2005). Carbon nanotube oscillators toward zeptogram detection. *Applied Physics Letters*. 86: 133111.
- [76] Forró et al. (1999). Elastic and Shear Moduli of Single-Walled Carbon Nanotube Ropes. *Physical Review Letters*. 82: 944.
- [77] L. Yang et al. (1999). Electronic Structure of Deformed Carbon Nanotubes. *Physical Review Letters*. 85:154.
- [78] A. Gupta et al. (2004). Single virus particle mass detection using microresonators with nanoscale thickness. *Applied Physics Letters*. 84: 1976.
- [79] R.F .Service. (2003). Nanomaterials Show Signs of Toxicity. *Science*. 300: 243.
- [80] R.F .Service. (2004). Nanotechnology Grows Up. *Science*. 304: 1732.
- [81] Dai H.J. et al. (2001). Growth of Single-Walled Carbon Nanotubes from Discrete Catalytic Nanoparticles of Various Sizes. *Journal of Physical Chemistry B*. 105: 11424.
- [82] Dai L.M. et al. (2006). Water-Assisted Growth of Aligned Carbon Nanotube–ZnO Heterojunction Arrays. *Advanced Materials*. 18: 1740–1744.